

Université du Québec  
Institut National de la Recherche Scientifique  
Centre Énergie Matériaux Télécommunications

**CONCEPTION DE NOUVEAUX COMPOSANTS EN TECHNOLOGIE  
HYBRIDE POUR LES COMMUNICATIONS À HAUT DÉBIT EN BANDE  
MILLIMÉTRIQUE**

Par  
Chaouki Hannachi

Mémoire ou thèse présentée pour l'obtention du grade de  
Philosophiae doctor (Ph.D.)  
en Télécommunications

**Jury d'évaluation**

Président du jury et examinateur interne	Professeur Tayeb A. Denidni INRS-EMT
Examinateur externe	Professeur Chahé Nerguizian École Polytechnique de Montréal
Examinateur externe	Professeur Dominic Deslandes École de Technologie Supérieure (ÉTS)
Directeur de recherche	Professeur Serioja Ovidiu Tatu INRS-EMT

## **REMERCIEMENTS**

Le travail présenté dans ce manuscrit est le fruit de cinq ans d'étude et de recherche à l'institut national de la recherche scientifique (INRS), dans le centre Énergie Matériaux Télécommunications (EMT).

En premier lieu, je tiens à remercier dieu pour l'aide qu'il m'a apporté tout le long de ce travail de recherche et pour toutes ses bénédictions qu'il m'a offertes. Par ailleurs, je tiens à exprimer mes sincères remerciements à mon directeur de rechercher, monsieur Serioja Ovidiu Tatu pour son soutien continu, sa disponibilité, sa gentillesse ainsi que sa confiance. Tous ces éléments ont constitués un cadre d'une grande sérénité dans le déroulement de mon projet de recherche.

Je souhaite également remercier chaleureusement tous mes collègues au centre Énergie Matériaux Télécommunications (EMT) et plus particulièrement monsieur Djerafi Tarek, madame Emilia Moldovan, monsieur Djilali Hammou et tous les étudiants en maîtrise et au doctorat, sans oublier bien évidemment les membres de l'équipe administrative de l'INRS-EMT Centre Bonaventure. Chacun d'entre eux a contribué directement ou indirectement, et à sa manière au succès de ces travaux.

Un grand merci également à tous les membres de l'équipe technique de Poly GRAMES à l'École Polytechnique de Montréal, pour leurs précieux conseils et leur support durant la fabrication et la caractérisation des prototypes, et en particulier, Jules Gauthier, Traian Antonescu, Maxime Thibault, et Steve Dubé.

Par ailleurs, je souhaite exprimer toute ma reconnaissance et mon estime aux membres du jury pour le temps qu'ils ont passé à la révision de ce mémoire et d'avoir accepté d'assister à la présentation de ce travail. La pertinence de leur réflexion scientifique m'aura permis d'améliorer grandement la qualité de ce manuscrit.

Enfin, je tiens à exprimer ma plus profonde gratitude à mes parents et mon épouse Aicha pour le soutien constant qu'ils m'ont accordé tout au long de ces années d'études doctorales. Leurs encouragements, leur confiance et leur patience m'ont permis de mener à bien cette aventure jusqu'à son terme.

## RÉSUMÉ

L'objectif des travaux de recherche présentés dans cette thèse est de contribuer significativement au développement et à la conception, de nouveaux circuits opérant en ondes millimétrique autour de la bande de 60 GHz, en adoptant la technologie MHMIC sur substrat céramique ultra-mince. Ces circuits, incluant le réflectomètre six-port (RSP), le détecteur de puissance basé sur la diode de type Schottky (HSCH-9161), le réseau d'antenne micro ruban de 16 éléments, ainsi que la transition microstrip à guide onde (MS-WR12) sont utilisés dans l'architecture du prototype final de la frontale radiofréquence millimétrique, destinée aux communications sans fil à haute débit.

La conception des circuits millimétriques mentionnés précédemment a été effectuée à l'aide des simulateurs électromagnétiques (full-wave simulator), ADS (Advanced Design Systems software of Keysight Technologies) pour les structures planaires et HFSS (High Frequency Structure Simulator of Ansoft Corporation) pour les structures 3D.

Tout les composant fabriqués ont été complètement caractérisés et ont fait l'objet d'une publication dans des journaux scientifiques validés par un comité de lecture. Donc, il s'agit d'un rapport de these basé sur les articles produits durant les différentes étapes du parcours de recherche, où chaque publication présente une partie du travail réalisé sous la forme d'un chapitre, à l'exception du dernier chapitre qui sera consacré à l'exposition des résultats de la caractérisation de la frontale radiofréquence proposée dans le cadre de ce projet.

# TABLE DES MATIÈRES

<b>Introduction .....</b>	<b>14</b>
<b>Structure de la These et Contributions .....</b>	<b>15</b>
<b>Chapitre 1 : .....</b>	<b>17</b>
<b>Système de Télécommunication Sans-Fils .....</b>	<b>17</b>
1. Architectures des systèmes de réception .....	17
1.1. Les récepteurs RF (Front-Ends).....	18
1.1.1 <i>Les récepteurs homodynes (conversion direct ou ZERO-IF)</i> .....	18
1.1.2 <i>Les récepteurs hétérodynes</i> .....	19
1.2. Frontale radiofréquence à base d'un réflectomètre six-port.....	20
1.3. Les détecteurs de puissance .....	24
1.3.1 <i>Structure et principe de fonctionnement</i> .....	24
1.4. Les amplificateurs à faible bruit (LNAs) .....	28
1.4.1 <i>Principe de fonctionnement et utilité</i> .....	28
1.4.2 <i>Spécifications typique d'un LNA à 60 GHz</i> .....	29
1.4.3 <i>Problématique de la composante continue ou “DC offset”</i> .....	29
1.5. Le réseau d'antennes .....	31
1.5.1 <i>Généralités</i> .....	31
1.5.2 <i>Directivité, Efficacité et Gain.</i> .....	31
Références .....	33
<b>Chapitre 2 : .....</b>	<b>35</b>
<b>Complete Characterization of Novel MHMICs for V band Communication Systems .....</b>	<b>35</b>
2.1. Introduction .....	36
2.2. Calibration Techniques and Standards .....	37
2.3. Basic Circuit Characterization.....	39
2.3.1. <i>90° Hybrid Coupler</i> .....	40
2.3.2. <i>Rat-Race Coupler</i> .....	43
2.3.3. <i>C. Wilkinson Power Divider/Combiner</i> .....	45
2.4. Six-port Circuit Characterization.....	48
2.5. Conclusion.....	53
References .....	54
<b>Chapitre 3 : .....</b>	<b>57</b>

<b>Performance Comparison of 60 GHz Printed Patch Antennas with Different Geometrical Shapes Using Miniature Hybrid Microwave Integrated Circuits Technology .....</b>	<b>57</b>
3.1. Introduction .....	58
3.2. Conventional designs and specifications .....	60
3.3. Antennas design and fabrication.....	61
3.4. Rectangular and Square Microstrip Patch Antennas Shapes .....	63
3.5. Triangular and Trapezoidal Microstrip Patch Antennas Shapes .....	65
3.6. Circular and Elliptical Microstrip Patch Antennas Shapes .....	67
3.7. Annular-ring Microstrip Patch Antenna Shape .....	69
3.8. Performance Summary and Comparison .....	71
3.9. Conclusion.....	72
References .....	73
<b>Chapitre 4 : .....</b>	<b>77</b>
<b>A Compact V-band Planar Gap-coupled 4x1 Antenna Array: Improved Design and Analysis.....</b>	<b>77</b>
4.1. Introduction .....	78
4.2. Antenna designs, fabrication, and measurement.....	80
4.3. Theoretical analysis .....	85
4.4. Modified 4x1 gap-coupled microstrip antenna array .....	88
4.5. Conclusion.....	94
References .....	95
<b>Chapitre 5 : .....</b>	<b>98</b>
<b>A V-band High Dynamic Range Planar Integrated Power Detector: Design and Characterization Process....</b>	<b>98</b>
5.1. Introduction .....	99
5.2 Design Methodology and Fabrication .....	100
5.3 Characterization Methodology and Results .....	103
<i>5.3.1 Dynamic range measurement.</i> .....	103
<i>5.3.2 Responsivity measurement .....</i>	106
<i>5.3.3 Performance Comparison .....</i>	108
References .....	110
<b>Chapitre 6 : .....</b>	<b>112</b>
<b>Broadband E-Band WR12 to Microstrip Line Transition Using a Ridge Structure on High-Permittivity Thin-Film Material .....</b>	<b>112</b>
6.1. Introduction .....	113
6.2. Design and Configuration.....	114

6.3. Results and Discussion .....	117
References .....	120
<b>Chapitre 7 : .....</b>	<b>121</b>
<b>Fabrication, Résultats et Discussions .....</b>	<b>121</b>
7.1. Prototypes des frontales radiofréquences fabriquées .....	121
7.2. Caractérisation d'une frontale radiofréquence à base du RSP en technologie guide d'onde .....	123
7.3. Caractérisation de la frontale radiofréquence à base du RSP en technologie MHMIC .....	126
7.3.1. <i>Simulation système</i> .....	126
7.3.2. <i>Mesure et caractérisation</i> .....	1288
7.3.3. <i>Validation expérimentale d'une liaison sans fil à 60 GHz</i> .....	12929
7.3.4. <i>Évaluation de la liaison à 60 GHz</i> .....	132
7.3.5. <i>Sensibilité du récepteur</i> .....	133
References .....	135
Conclusion générale et perspectives .....	136
Liste des publications .....	138

## **LISTE DES TABLEAUX**

Tableau 1.1- Caractéristiques typiques d'un LNA à 60 GHz .....	30
Tableau 3.1 - Theoretical design parameters for conventional geometries of microstrip patch antennas. .	62
Tableau 3.2: Comparison Table of the performances between 7 shapes of fabricated microstrip patch antennas.....	73
Tableau 4.1- Even and Odd mode Capacitances Equations.....	87
Tableau 5.1- Performance comparison of the proposed power detector with some previously published designs in different technologies.....	110
Tableau 6.1- State of the art of E-band transitions.....	120
Tableau 7.1- Equipements employés au banc de test.....	124

## **LISTE DES FIGURES**

Figure 1.1 - Structure globale d'un récepteur .....	18
Figure 1.2 - Architecture d'un récepteur homodyne .....	20
Figure 1.3 - Architecture d'un récepteur hétérodyne .....	21
Figure 1.4 - Architecture d'une frontale radiofréquence à base du réflectomètre six-port.....	22
Figure 1.5 - Schéma typique d'un détecteur de puissance à base de diode de type Schottky.....	26
Figure 1.6 - Schéma équivalent de la sortie du détecteur à base de diode Schottky.....	27
Figure 1.7 - Caractéristique typique d'un détecteur à diode .....	28
Figure 1.8 - Exemple d'implantation d'un LNA à 60 GHz (TGA4600).....	30
Figure 1.9 - Problème de la fuite d'oscillateur local (OL) dans une chaîne de réception homodyne.....	31
Figure 1.10 - Problème de fuite des signaux parasites vers l'oscillateur local (OL) dans une chaîne de réception homodyne .....	31
Figure 1.11-Efficacité de rayonnement et efficacité de l'antenne .....	33
Figure 2.1 - Microphotograph of the fabricated circuits on thin ceramic substrate of 2.54 cm x 2.54 cm.	40
Figure 2.2 - Microphotograph of the branch-line coupler.....	41
Figure 2.3 - Measured input return loss for the 90° hybrid coupler.....	42
Figure 2.4 - Measured transmission S parameter magnitudes for the 90° hybrid coupler.....	43
Figure 2.5 - Measured transmission S parameter phase difference for the 90° hybrid coupler.....	43
Figure 2.6 - Micro-photograph of the rat-race coupler. ....	44
Figure 2.7 - Measured input return loss for the rat-race coupler. ....	45
Figure 2.8 - Measured transmission S parameter magnitudes for the rat-race coupler.....	45
Figure 2.9 - Measured transmission S parameter phase difference for the rat-race coupler.....	46
Figure 2.10 - Microphotograph of the Wilkinson power divider/combiner.....	47
Figure 2.11 - Measured return loss for the Wilkinson power divider /combiner.....	48
Figure 2.12 - Measured transmission S parameter magnitudes for the Wilkinson power divider/combiner. .....	48
Figure 2.13 - Measured transmission S parameter phase difference for the Wilkinson power divider/combiner .....	49
Figure 2.14 - Six-port circuit block diagram.....	49
Figure 2.15 - Micro-photograph of the novel millimeter wave six-port in a typical S parameter measurement configuration.....	50
Figure 2.16 - Measured RF inputs return loss and isolation for the proposed six-port.....	51
Figure 2.17 - Typical measured transmission magnitudes (S25, S45) for the proposed six-port. ....	52

Figure 2.18 - Typical measured transmission magnitudes (S16, S36) for the proposed six-port.....	52
Figure 2.19 - Typical measured outputs matches for the proposed six-port.....	53
Figure 2.20 - Typical measured transmission phase difference of (S52, S54) for the proposed six-port ..	53
Figure 2.21 - Typical measured transmission phase difference of (S61, S63) for the proposed six-port ..	54
Figure 3.1 - Micro-photographs of (a) The fabricated microstrip patch antennas on very thin ceramic substrate, (b) Cross-section view of thin ceramic substrate and metal layers, and (c) On-wafer measurement with GSG-150 $\mu\text{m}$ probe.....	64
Figure 3.2 - Microphotograph with geometric dimensions of (a) Rectangular patch antenna, and (b) Square patch antenna.....	65
Figure 3.3 - Measured and simulated return loss and input VSWR : (a) Measured and simulated return loss of rectangular and square patch antennas, and (b) Measured VSWR of rectangular and square patch antennas.....	66
Figure 3.4 : Simulated radiation characteristics at 61.8 GHz of (a) Square patch antenna and (b) Rectangular patch antenna .....	66
Figure 3.5 - Micro-photograph with geometric dimensions of (a) Triangular patch antenna and (b) Trapezoidal patch antenna.....	67
Figure 3.6 - Measured and simulated return loss, and input VSWR : (a) Measured and simulated return loss of triangular and trapezoidal patch antennas, (b) Measured VSWR of triangular and trapezoidal patch antennas .....	68
Figure 3.7 - Simulated radiation characteristics at 61.7 GHz of (a) ,Triangular patch antenna and (b), Trapezoidal patch antenna.....	68
Figure 3.8 - Microphotograph with geometric dimensions of, (a) Circular patch antenna and, (b) Elliptical patch antenna.....	69
Figure 3.9 - Measured and simulated return loss and input VSWR : (a) Measured and simulated return loss of circular and elliptical patch antennas, and (b) Measured VSWR of circular and elliptical patch antennas .....	70
Figure 3.10 - Simulated radiation characteristics at 61 GHz of (a) Circular patch antenna and, (b) Elliptical patch antenna.....	70
Figure 3.11 - Design of the proposed annular ring patch antenna : (a) Microphotograph with geometric dimensions, (b) Measured and simulated return loss, and (c) Measured input VSWR.....	71
Figure 3.12 - Simulated radiation characteristics of annular ring patch antenna at 62 GHz : (a) in the elevation plane (b) in the 3D polar plots.....	72

Figure 4.1 - Single modified patch antenna and its equivalent rectangular patch in (a) Photograph of the fabricated prototypes with the geometrical parameters of the single rectangular patch antenna, and single modified patch antenna in (b), and (c) respectively.....	81
Figure 4.2 - Photograph of the fabricated prototype with the geometrical parameters of (a) the rectangular gap-coupled microstrip patch antenna and (b) the modified gap-coupled microstrip patch antenna. ....	82
Figure 4.3 - Measured and simulated return loss of single modified patch (SMP) and single rectangular patch antenna (SRP).....	83
Figure 4.4 - Measured and simulated return loss of the modified gap-coupled patch (MGCP) and the rectangular gap-coupled patch antenna (RGCP). .....	84
Figure 4.5 - Calculated gain at -10 dB bandwidth of single modified patch (SMP), single rectangular patch antenna (SRP), modified gap-coupled patch (MGCP) and the rectangular gap-coupled patch antenna (RGCP). .....	85
Figure 4.6 - Calculated efficiency at -10 dB bandwidth of single modified patch (SMP), single rectangular patch antenna (SRP), modified gap-coupled patch (MGCP) and the rectangular gap-coupled patch antenna (RGCP). .....	86
Figure 4.7 - Even and odd mode capacitances of the proposed gap-coupled microstrip patch antenna structure.....	87
Figure 4.8 - Coupling capacitances versus normalized gap width for the alumina substrate ( $\epsilon_r = 9.9$ and $h = 127 \mu\text{m}$ ). ....	88
Figure 4.9 - Variation of the input impedance magnitude with frequency for different normalized gap distances. ....	89
Figure 4.10 - Photographs of the fabricated 4x1 gap-coupled antenna array (a) prototype with coplanar line (CPWG) to microstrip transition (b) prototype with V-connector (1.85) mm and (c) simulated surface current distributions on the conductor. ....	90
Figure 4.11 - Simulated RF inputs return loss and isolation of the feed network.....	91
Figure 4.12 - Simulated transmission S-parameter magnitudes of the feed network.....	91
Figure 4.13 : Antenna under test (AUT) with (a) The Anritsu 37397C vector network analyzer (VNA), and (b) The automated anechoic chamber.....	92
Figure 4.14: Measured and simulated return loss of the fabricated 4x1 gap-coupled antenna arrays. ....	93
Figure 4.15: Radiation patterns of the fabricated 4x1 gap-coupled antenna array in E and H-planes.....	93
Figure 4.16: Simulated and measured gains of the fabricated 4x1 gap-coupled antenna array.....	94
Figure 5.1: A V-band power detector circuit design: (a) Photograph of the fabricated prototype, (b) Small signal linear model used in ADS for the employed HSCH-9161 Schottky diode, and (c) HSCH-9161 Schottky diode with its geometric dimensions.....	102

Figure 5.2: Simulated and measured return loss of the fabricated MHMIC V-band power detector.....	104
Figure 5.3: Experimental setup for the fabricated MHMIC V-band power detector characterization.....	105
Figure 5.4: Simulated and measured detected power versus input power at 61 GHz.....	106
Figure 5.5: Measured output detected power versus frequency for different millimeter-wave input power levels (Pin= -17, -21, and -25 dBm).....	106
Figure 5.6: Typical experimental setup for responsivity measurement.....	107
Figure 5.7: Measured power detector responsivity (mV/mW), from 60 to 70 GHz .....	108
Figure 5.8: Measured modulated reference signal (VRef), and the output voltage waveform (Vout).....	109
Figure 6.1-Microstrip-to-ridge waveguide in-line. transition.....	116
Figure 6.2-Parametric study and equivalent circuit, .....	117
Figure 6.3-Proposed rectangular waveguide to microstrip line transition.....	118
Figure 6.4-Measured and simulated insertion loss, and return loss of the fabricated transition prototype.	119
	.....
Figure 7.1- Premier prototype de la frontale radiofréquence, avec l'amplificateur faible bruit (LNA) et le réseau d'antenne microruban intégré .....	122
Figure 7.2- Deuxième prototype de la frontale radiofréquence, sans amplificateur faible bruit (LNA) et le réseau d'antenne microruban. ....	122
Figure 7.3-Banc de test de la frontale radiofréquence à base du RSP (Réflectomètre Six-Port) en technologie guide d'onde.....	123
Figure 7.4 - Schéma bloc du banc de caractérisation.....	123
Figure 7.5 - Résultats de démodulations MPSK.....	125
Figure 7.6 - Schéma bloc du circuit de simulation du récepteur à base du réflectomètre six-port. ....	126
Figure 7.7 - Diagrammes simulés de constellation PSK/QAM des signaux I et Q.....	127
Figure 7.8 - Schéma bloc du banc de caractérisation d'un récepteur basé sur un six-port intégré en technologie microstrip.....	128
Figure 7.9 - Diagrammes expérimentaux de constellation PSK/QAM des signaux I et Q. ....	129
Figure 7.10 - Photographe du banc de caractérisation du récepteur à base du réflectomètre six-port pour une liaison sans fil de 1.75m. ....	130
Figure 7.11 - Formes d'ondes des signaux I et Q pour une modulation BPSK. ....	130
Figure 7.12 - Formes d'ondes des signaux I et Q pour une modulation QPSK. ....	131
Figure 7.13 - Formes d'ondes des signaux I et Q pour une modulation 8PSK. ....	131
Figure 7.14 - Formes d'ondes des signaux I et Q pour une modulation 8PSK. ....	132

## **LISTE DES ABRÉVIATIONS**

ADS Advanced Design System  
AWGN Additive White Gaussian Noise  
BER Bit Error Rate  
CREER Centre for Research in Radiofrequency Electronics  
DSP Digital Signal Processor  
FPGA Field Programmable Gate Array  
FCC Federal Communication Commission  
HFSS High Frequency Structure Simulator  
IEEE the Institute of Electrical and Electronics Engineers  
INRS Institut National de la Recherche Scientifique  
IF Intermediate Frequency  
LMR Ligne Microruban  
LOS Line of Sight  
MHMIC Miniature Hybrid Microwave Integrated Circuits  
MMIC Microwave Monolithic Integrated Circuit  
MIMO Multiple-Input Multiple-Output  
MISO Multiple-Input Single-Output  
NLOS Non Line of Sight  
NF Noise Factor  
QPSK Quadrature Phase-Shift Keying  
RF Radio Frequency  
RWG Rectangular Waveguide  
SIMO Single-Input Multiple-Output  
SISO Single-Input Single-Output  
SINR Signal to Interference-plus-Noise Ratio  
SNR Signal to Noise Ratio  
SIR Signal to Interference Ratio  
SINR Signal to Interference plus Noise Ratio  
SIW Substrate Integrated Waveguide

SLL Side Lobes Level  
SOLT Short-Open-Load-Thru  
TRL Thru, Reflect, Line  
VNA Vector Network Analyser  
XPL Cross Polarization Level

## INTRODUCTION

Durant la dernière décennie, les télécommunications sans fil ont connus un progrès sans précédent, grâce à des terminaux mobile miniatures assurant la transmission de gros volumes d'information en peu de temps, avec une grande souplesse et une grande mobilité. Aujourd'hui, plusieurs techniques sont envisagées afin de répondre à ce besoin de haut débit parmi lesquelles on peut citer ; le recours à des systèmes à entrées et sorties multiples (MIMO –Multiple Input Multiple Output), les transmissions ultra large bande (ULB) et enfin, la montée en fréquence vers le spectre des ondes millimétriques qui constitue une des solutions les plus prometteuses pour accroître le débit (jusqu'aux quelques Gbit/s) des futurs réseaux locaux sans fil (WPAN). Dans ce dernier contexte, la bande de fréquences sans licence autour de 60 GHz a été retenue un peu partout dans le monde comme une bande possible pour les transmissions très haut débit, particulièrement pour des applications dans un environnement intérieur de type réseaux locaux sans fil (WLAN) à très haut débit ( $>100$  Mbit/s) [1-2]. De nombreux travaux ont été développés considérant certains aspects comme la conception des nouveaux circuits et des antennes opérant à 60 GHz, la caractérisation du canal de propagation, ainsi que les techniques de modulations/démodulations. Cependant, peu d'études portent sur une réalisation complète d'un système de communications sans fil à 60 GHz et la caractérisation de ses performances dans des environnements réalistes. Cette dernière approche est à la base de mon projet de recherche [3].

Les travaux proposés dans cette thèse portent principalement sur le développement, la fabrication et la caractérisation expérimentale, de nouveaux circuits millimétriques destinés aux futurs systèmes sans fil haut débit, de l'ordre du Gbits/s, conformément à la norme sans fil IEEE 802.15.3c. Ces circuits comprenant le réflectomètre six-port (RSP), le détecteur de puissance basé sur la diode de type Schottky (HSCH-9161), le réseau d'antenne micro ruban de 16 éléments, ainsi que la transition microstrip à guide onde (MS-WR12). Ils seront tout intégrés dans la structure du prototype final de la frontale radiofréquence millimétrique, utilisant la technologie MHMIC sur un substrat céramique ultra-mince. Ce prototype à son tour, sera caractérisé et les résultats seront exposés et discutés.

## **STRUCTURE DE LA THESE ET CONTRIBUTIONS**

Ce manuscrit sera décomposé en sept chapitres. Le premier chapitre décrit les différentes architectures employées à la réception dans un système de radiocommunications. En suite, il présente le principe de base du réflectomètre six-port dans son utilisation conventionnelle et dans les récepteurs, en tant que démodulateur I/Q des signaux RF. Nous avons également exposé quelques éléments de théorie concernant le reste des composants constituant une chaîne de réception tel que les détecteurs de puissance, les amplificateurs faibles bruits (LNA), ainsi que les antennes micro rubans. Ces détails théoriques permettront aux lecteurs de comprendre les différentes notions abordées dans les chapitres qui suivent.

Dans la deuxième chapitre, nous allons entrer dans le vif du sujet, nous exposerons les différents circuits millimétriques conçus en technologie MHMIC (Miniaturized Hybrid Microwave Integrated Circuit), en commençant par les éléments les plus simples tels que le coupleur hybride H90°, le coupleurs rate-race et le diviseur de puissance de type Wilkinson pour arriver à une nouvelle structure d'un circuits passifs qui est l'interféromètre six-port. Tous les circuits fabriqués ont fait l'objet d'une optimisation rigoureuse et ont été caractérisés expérimentalement par l'exploitation des mesures de paramètres de dispersion S au Laboratoire RF du Centre Énergie, Matériaux et Télécommunications.

Dans le troisième chapitre, nous allons effectuer une étude comparative de différentes formes d'antennes imprimées dont le but est de déterminer la forme géométrique de l'élément patch, la plus convenable pour notre frontale radiofréquence, en termes de bande passante, gain, taille, et efficacité. Les formes géométriques considérées sont la forme rectangulaire, carré, triangulaire, trapézoïdale, circulaire, elliptique et annulaire. En effet, le meilleur élément résultant de cette étude sera intégré dans un réseau d'antenne comprenant au minimum 16 éléments pour le prototype final de la frontale radiofréquence.

Le chapitre quatre élargit encore plus la recherche dans le domaine des antennes micro ruban, en adoptant cette fois la technique de couplage par proximité en ondes millimétriques, particulièrement dans la bande de 57 à 65 GHz, afin de concevoir une nouvelle structure améliorée de réseau d'antenne imprimé ayant 4 éléments. La structure proposée a été analysée en terme de performance, elle montre une largeur de bande d'environ 7%, et un gain mesuré autour

de 10,7 dB tout en maintenant une taille réduite (5,2 mm x 9,5 mm). Avec ces performances, la structure du réseau d'antenne proposée constitue une excellente alternative aux futures frontales radiofréquences intégrées opérant en ondes millimétriques, elle peut être relié directement à divers circuits MHMIC passifs, ou à des dispositifs actifs tel que les amplificateurs faible bruit (LNA) par l'intermédiaire de la technologie de liaison par fil, sur un substrat d'alumine ultra mince standard.

Dans le cinquième chapitre, nous avons développé et conçu le détecteur de puissance à base de diode Schottky qui sera connecté aux quatre sorties du réflectomètre six-port pour la conversion de fréquence. Nous avons utilisé à cet effet l'outil de conception électromagnétique Momentum de Keysight Technologies, pour le design des circuits d'adaptation à l'entrée et à la sortie du détecteur. Le détecteur à base de diode Schottky HSCH-9161 a démontré d'excellentes performances notamment, une très large zone de détection quadratique, haute sensibilité, et une très bonne adaptation.

Le sixième chapitre, concerne l'étude, la réalisation, et la caractérisation d'une nouvelle transition entre la ligne micro ruban et le guide d'onde rectangulaire WR12 dans la bande de fréquence millimétrique, de 60 à 90 GHz. Cette transition est requise afin d'alimenter notre prototype de frontale radiofréquence en signal de pompe OL (Oscillateur Local), tout en assurant évidemment la synchronisation entre les signaux OL et RF dans l'architecture du prototype de frontale proposé.

Le dernier chapitre, le septième, c'est le chapitre qui englobe tous les éléments développés dans le présent projet. En effet, dans cette partie nous allons exposer les résultats de caractérisation de la frontale radiofréquence développée et fabriquée dans le cadre de cette thèse. Ces résultats incluent une évaluation expérimentale de la qualité de la transmission en termes de différents types de modulation incluant BPSK, QPSK, 8PSK, 16PSK, 16QAM, et 32QAM, ainsi que la validation pratique d'une liaison sans fil à 60 GHz en utilisant le prototype de la frontale radiofréquence fabriquée.

Enfin, nous finissons par une conclusion générale qui résume l'ensemble du travail, ainsi que les travaux futurs, et qui sera exposée à la fin du rapport.

## CHAPITRE 1 :

# SYSTÈME DE TÉLÉCOMMUNICATION SANS FILS

## 1. Architectures des systèmes de réception

Habituellement, le signal que l'antenne détecte ne contient pas seulement l'information importante, il est souvent associé à d'autres parasites tel que le bruit et d'autres signaux inutiles. Alors, une amplification du signal intéressant est envisageable afin de protéger le système au maximum, du bruit, des signaux parasites ainsi des non-linéarités du récepteur. Pour cette raison, un ensemble d'amplificateur à faible bruit (LNA-Low Noise Amplifier) et un filtre passe bande à l'entrée du récepteur sont nécessaires.

Après avoir isolé le signal, on le ramène autour d'une fréquence permettant son traitement grâce à un bloc démodulateur-synthétiseur comme le montre la figure 1.1.

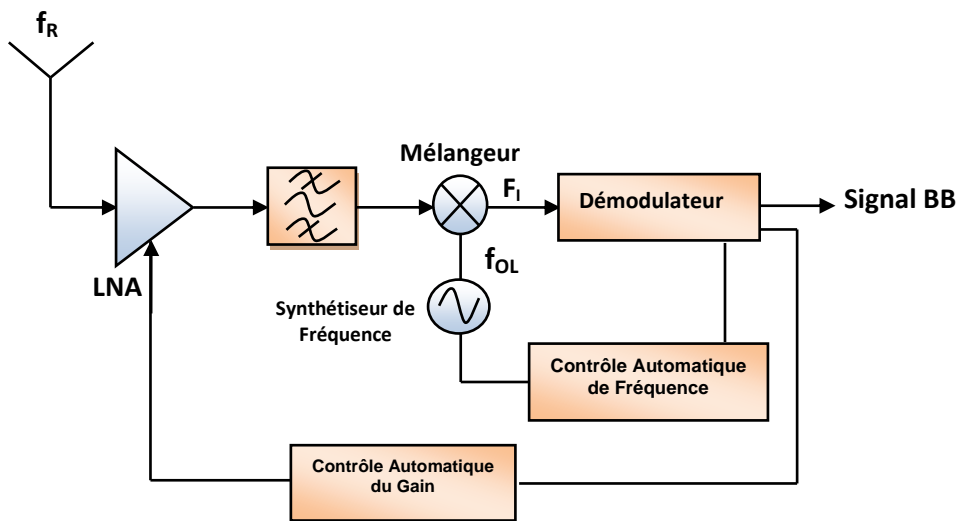


Figure 1.1 - Structure globale d'un récepteur.

Quelque soit le degré de complexité, tout récepteur est construit autour des mêmes éléments de base. Dans notre étude, on va s'intéresser particulièrement de la fonction primordiale dans une chaîne de réception qui est la démodulation. Dans ce qui suit, nous fournirons une description détaillée sur les principaux types de récepteurs radiofréquences [1].

## 1.1. Les récepteurs RF (Front-Ends)

La partie RF d'un récepteur a pour rôle de transposer vers une fréquence centrale, habituellement inférieure à celle reçue. Le signal reçu est démodulé et traité par la suite, afin qu'il sera transmis au destinataire final. Nous pouvons distinguer deux grandes catégories de récepteurs, des récepteurs homodynes dont le passage des fréquences RF vers les basses fréquences se fait directement ou en plusieurs étapes, quand il s'agit des récepteurs hétérodynes.

### 1.1.1 Les récepteurs homodynes (conversion direct ou ZERO-IF)

Ce type de récepteur est né de la problématique et de ces conséquences du filtrage de la fréquence image. Cette architecture consiste à transposer la bande de réception RF directement en bande de base BB. La fréquence de l'oscillateur local chargée de réaliser la transposition doit être identique à celle de la porteuse centrale de la bande RF, ce qui va annuler la fréquence intermédiaire FI. Alors, le signal image est superposé au signal RF.

L'inconvénient majeur de cette architecture est la présence d'une tension continue de décalage (DC-offset) en sortie des mélangeurs causé principalement par des défauts d'isolement au niveau du mélangeur entre les voies RF et OL [1-2].

D'autres inconvénients peuvent se rajouter à cette structure, tel que l'appariement entre les deux voies I et Q qui est pratiquement impossible, ce qui va se traduire en réalité par une erreur de gain ou de phase qui va déformer la constellation du signal et augmenter le taux d'erreur binaire (TEB). Par ailleurs, la dégradation de la sensibilité du récepteur aux signaux très basses fréquences, à cause du niveau élevé du bruit qui s'exprime en  $1/f$  et non thermique qui va se superposer au signal utile.

Malgré ces points négatifs, ce type de récepteur est de plus en plus populaire de part la simplicité du traitement RF qui est associé à un niveau d'intégration largement amélioré par rapport aux récepteurs hétérodynes.

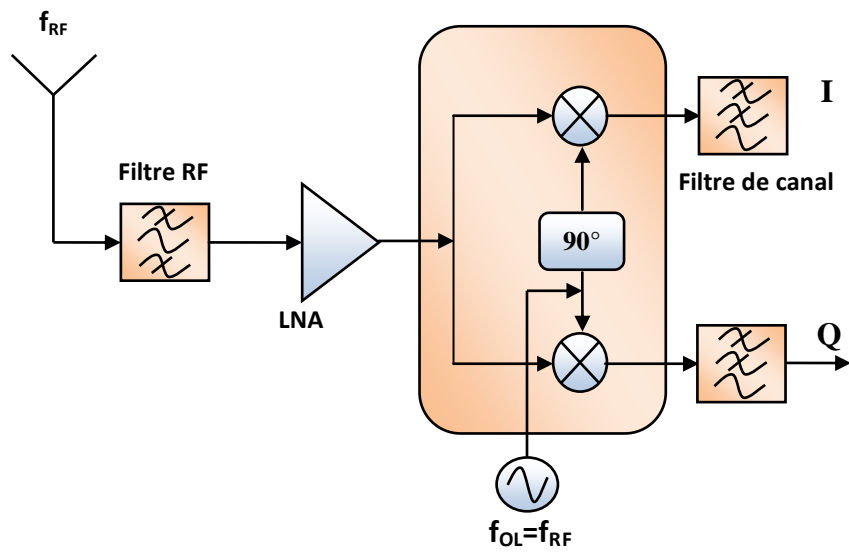


**Figure 1.2 - Architecture d'un récepteur homodyne.**

### 1.1.2 Les récepteurs hétérodynes

Le principe de cette architecture qui est illustré dans figure 1.3 consiste à la transposition de la bande du signal RF reçue autour d'une fréquence FI fixe. Si cette transposition se fait en une seule étape, le récepteur est hétérodyne, si elle nécessite plusieurs étapes alors le récepteur est appelé superhétérodyne.

Dans le cas d'une structure superhétérodyne, une première transposition du spectre peut se réaliser par la multiplication du signal RF avec le signal issu d'un oscillateur local  $f_{OL1}$ . La deuxième transposition est réalisée par un démodulateur IQ constitué d'une paire de mélangeurs montés en quadrature avec un oscillateur local  $f_{OL2}$ . Grâce à ses performances remarquables en termes de sélectivité et de sensibilité, cette architecture est la plus utilisée dans les mobiles de deuxième et troisième génération.

L'inconvénient majeur de ce type de récepteur est lié au problème de réjection de la fréquence image. Plusieurs essais ont été envisagés afin d'intégrer cette structure. Mais les filtres RF et FI sont difficilement intégrables, ce qui rend cette architecture très lourde en termes de complexité. Effectivement, la réalisation de ces filtres exige l'intégration des inductances permettant d'atteindre des facteurs de qualité importants, ce qui est pratiquement difficile, car les facteurs de qualité que nous pouvons obtenir sont insuffisants pour assurer une bonne sélectivité du récepteur [2-3].

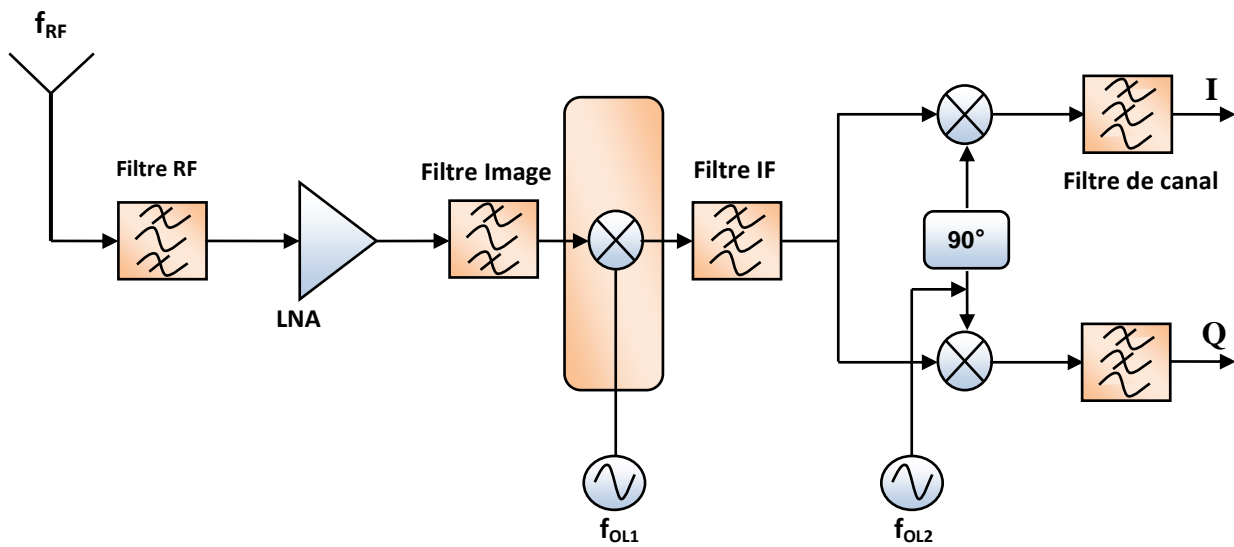


**Figure 1.3 - Architecture d'un récepteur hétérodyne.**

## 1.2. Frontale radiofréquence à base d'un réflectomètre six-port

La structure que nous allons proposer dans l'étude suivante va nous permettre d'éclaircir le principe de fonctionnement d'une frontale radiofréquence à base de réflectomètre six-port dans la démodulation de signaux RF. La structure présentée dans la figure 1.4 est composée de trois coupleurs Hybrides H-90 qui produisent des voies directes et couplées en quadrature de phases, et un coupleur de type Wilkinson, qui peut agir comme un diviseur de puissance. L'architecture proposée permet d'obtenir à partir de mesures de puissance en sortie, la différence de phase et le rapport d'amplitude entre un signal inconnu qui provient de l'antenne,  $a_6$ , et le signal de référence qui provient de l'oscillateur local,  $a_5$  [3-4].

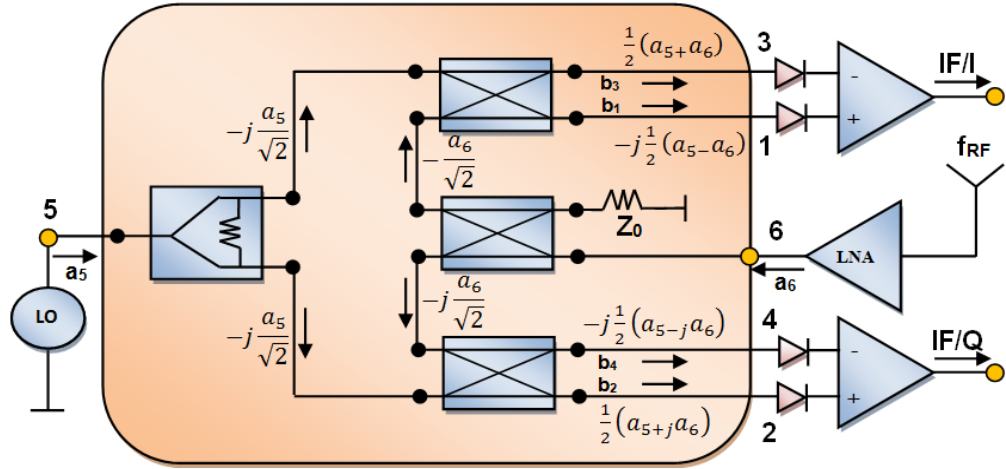


**Figure 1.4** - Architecture d'une frontale radiofréquence à base du réflectomètre six-port.

Les signaux de sortie,  $b_i$ , peuvent s'exprimer en fonctions des signaux  $a_i$  et les paramètres de dispersion  $S_{ij}$  du réflectomètre six-port par la relation linéaire suivante :

$$b_i = \sum_{j=1}^6 S_{ij} a_j , \quad i = 1, \dots, 6 \quad (1.1)$$

Les paramètres  $S_{ij}$  du réflectomètre six-port peuvent être obtenus directement à partir de la figure 1.4. À cet effet, on exploite les matrices de dispersion  $[S]$ , du coupleur hybride H-90°, et celle du diviseur de puissance Wilkinson. Les matrices correspondantes sont données dans l'ordre par les équations (1.2) et (1.3).

$$[S] = \frac{1}{\sqrt{2}} \begin{bmatrix} 0 & j & 1 & 0 \\ j & 0 & 0 & 1 \\ 1 & 0 & 0 & j \\ 0 & 1 & j & 0 \end{bmatrix} \quad (1.2)$$

$$[S] = -j \frac{1}{\sqrt{2}} \begin{bmatrix} 0 & 1 & 1 \\ 1 & 0 & 0 \\ 1 & 0 & 0 \end{bmatrix} \quad (1.3)$$

Donc, on obtient la matrice  $[S]$  globale du réflectomètre six-port de la figure 1.4.

$$[S] = \frac{1}{2} \begin{bmatrix} 0 & 0 & 0 & 0 & -j & j \\ 0 & 0 & 0 & 0 & 1 & j \\ 0 & 0 & 0 & 0 & 1 & 1 \\ 0 & 0 & 0 & 0 & -j & -1 \\ -j & 1 & 1 & -j & 0 & 0 \\ j & j & 1 & -1 & 0 & 0 \end{bmatrix} \quad (1.4)$$

À l'aide de l'équation (1.4), nous pouvons conclure les formules des quatre formes d'ondes émergentes,  $b_1, b_2, b_3, b_4$ , en fonction des deux ondes incidentes  $a_5$  et  $a_6$  :

$$\left\{ \begin{array}{l} b_1 = -j \frac{a_5}{2} + j \frac{a_6}{2} \\ b_2 = \frac{a_5}{2} + j \frac{a_6}{2} \\ b_3 = \frac{a_5}{2} + \frac{a_6}{2} \\ b_4 = -j \frac{a_5}{2} - \frac{a_6}{2} \end{array} \right. \quad (1.5)$$

Dans le but de simplifier les calculs, nous allons admettre que les signaux RF, résultant de l'antenne,  $a_6$ , et de l'oscillateur local,  $a_5$ , ont un rapport d'amplitude  $\alpha$ , une différence de phase,  $\Delta\varphi(t) = \varphi_6(t) - \varphi_5$  et une différence de fréquence,  $\Delta\omega = \omega - \omega_0$ . Ces signaux, nous pouvons les exprimer par les équations suivantes [3] :

$$a_5 = a \cdot e^{j(\omega_0 \cdot t + \varphi_5)} \quad (1.6)$$

$$a_6 = \alpha \cdot a \cdot e^{j(\omega_0 \cdot t + \varphi_6(t))} = \alpha \cdot a_5 \cdot e^{j(\Delta\omega \cdot t + \Delta\varphi(t))} \quad (1.7)$$

En remplaçant les signaux  $a_5$  et  $a_6$  par leurs expressions dans le système d'équations précédent, on obtient :

$$b_1(t) = -j \frac{a}{2} \cdot e^{j(\omega_0 t + \varphi_5)} \cdot [1 + \alpha \cdot e^{j(\Delta\omega \cdot t + \Delta\varphi(t) + \pi)}] \quad (1.8)$$

$$b_2(t) = \frac{a}{2} \cdot e^{j(\omega_0 t + \varphi_5)} \cdot [1 + \alpha \cdot e^{j(\Delta\omega \cdot t + \Delta\varphi(t) + \frac{\pi}{2})}] \quad (1.9)$$

$$b_3(t) = \frac{a}{2} \cdot e^{j(\omega_0 t + \varphi_5)} \cdot [1 + \alpha \cdot e^{j(\Delta\omega \cdot t + \Delta\varphi(t))}] \quad (1.10)$$

$$b_4(t) = -j \frac{a}{2} \cdot e^{j(\omega_0 t + \varphi_5)} \cdot [1 + \alpha \cdot e^{j(\Delta\omega \cdot t + \Delta\varphi(t) - \frac{\pi}{2})}] \quad (1.11)$$

Les signaux en bande FI (fréquence intermédiaire) sont les résultats de la connexion des quatre sorties du réflectomètre six-port à des détecteurs (voir figure 1.4). Nous considérons que la puissance délivrée en sortie de chaque détecteur idéal, est proportionnelle au carré de la magnitude du signal RF [4-6].

$$v_i = K_i \cdot |b_i|^2 = K_i \cdot b_i \cdot b_i^*, \quad i = 1, \dots, 4 \quad (1.12)$$

Sachant que les détecteurs sont identiques ( $K_i = K$ ), alors :

$$v_1(t) = K \frac{a^2}{4} \cdot \{1 + \alpha^2 - 2 \cdot \alpha \cdot \cos[\Delta\omega \cdot t + \Delta\varphi(t)]\} \quad (1.13)$$

$$v_2(t) = K \frac{a^2}{4} \cdot \{1 + \alpha^2 - 2 \cdot \alpha \cdot \sin[\Delta\omega \cdot t + \Delta\varphi(t)]\} \quad (1.14)$$

$$v_3(t) = K \frac{a^2}{4} \cdot \{1 + \alpha^2 + 2 \cdot \alpha \cdot \cos[\Delta\omega \cdot t + \Delta\varphi(t)]\} \quad (1.15)$$

$$v_4(t) = K \frac{a^2}{4} \cdot \{1 + \alpha^2 + 2 \cdot \alpha \cdot \sin[\Delta\omega \cdot t + \Delta\varphi(t)]\} \quad (1.16)$$

Afin de générer des signaux IF/ IQ en quadrature, nous allons utiliser des amplificateurs différentiels dans la bande intermédiaire, aux sorties, 1 et 3, et 2 et 4, (Figure 1.4) :

$$v_{IF}^I(t) = A_{IF} \cdot [v_3(t) - v_1(t)] = \alpha \cdot K \cdot a^2 \cdot A_{IF} \cdot \cos[\Delta\omega \cdot t + \Delta\varphi(t)] \quad (1.17)$$

$$v_{IF}^Q(t) = A_{IF} \cdot [v_4(t) - v_2(t)] = \alpha \cdot K \cdot a^2 \cdot A_{IF} \cdot \sin[\Delta\omega \cdot t + \Delta\varphi(t)] \quad (1.18)$$

On procède à une seconde conversion de fréquence suivie par un filtrage basse fréquence, on obtient les formules des signaux I/Q en bande de base.

$$I(t) = \frac{1}{2} \cdot \alpha \cdot K \cdot a^2 \cdot A_{IF} \cdot A_{BB} \cdot \cos[\Delta\varphi(t)] \quad (1.19)$$

$$Q(t) = \frac{1}{2} \cdot \alpha \cdot K \cdot a^2 \cdot A_{IF} \cdot A_{BB} \cdot \sin[\Delta\varphi(t)] \quad (1.20)$$

Le signal I/Q en bande de base peut être exprimé dans le plan complexe par l'équation suivante :

$$\Gamma(t) = I(t) + Q(t) = \frac{1}{2} \cdot \alpha \cdot K \cdot a^2 \cdot A_{IF} \cdot A_{BB} \cdot e^{j\Delta\varphi(t)} \quad (1.21)$$

Cette expression montre que les termes  $A_{IF}$  et  $A_{BB}$ , sont en relation avec l'amplification en bande intermédiaire IF et en bande de base BB. Dans les deux types d'architectures, hétérodyne dans les équations (1.17) et (1.18), et l'architecture homodyne dans les équations (1.19) et (1.20). On peut obtenir en bande de base, le rapport d'amplitude  $\alpha$  ainsi que la différence de phase,  $\Delta\varphi(t) = \varphi_6(t) - \varphi_5$ . Ce rapport, entre les domaines RF et la bande intermédiaire ainsi que la bande de base, mis en évidence le rôle du réflectomètre six-port comme un discriminateur de phase, de fréquence et d'amplitude [7].

### 1.3. Les détecteurs de puissance

#### 1.3.1 Structure et principe de fonctionnement

Comme nous l'avons vu dans la partie précédente, l'utilisation de signaux modulés, nécessite l'implémentation des détecteurs de puissance rapides, généralement à base de diodes Schottky non polarisées (zéro-bias) afin de permettre la détection de puissance au niveau des quatres sorties de l'interferomètre six-porte. La configuration typique de ces détecteurs inclut typiquement la diode mentionnée précédemment suivie d'un filtre de type passe-bas, tel qu'ilustré à la figure 1.5 suivant [8] :

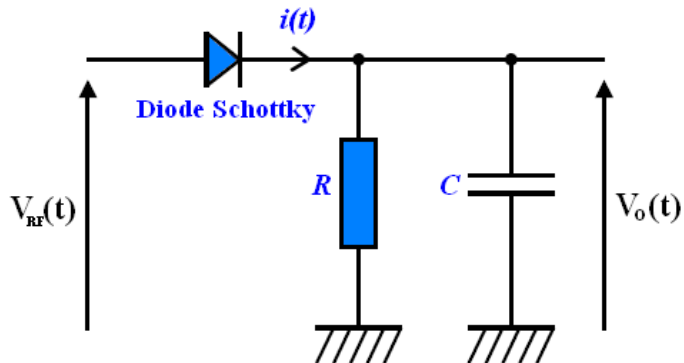


**Figure 1.5** - Schéma typique d'un détecteur de puissance à base de diode de type Schottky.

La caractéristique non linéaire reliant le courant  $i(t)$  qui parcourt la diode et la tension RF d'entrée  $V_{RF}(t)$  est généralement décrite par la loi de Schottky. En négligeant la résistance série parasite de la diode, cette caractéristique sera exprimée par :

$$i(t) = I_s \left[ \exp \left( \frac{q_o v_{RF}(t)}{nKT} \right) - 1 \right] \quad (1.22)$$

Avec :

$I_s$  : le courant de saturation,  $q_o$  : la charge de l'électron,  $n$  : le coefficient d'idéalité,  $K$  : la constante de Boltzmann,  $T$  : la température.

Sachant que la tension  $V_{RF}(t)$  peut exprimer par :

$$v_{RF}(t) = A \cdot \cos(\omega_{RF} t), \quad \omega_{RF} = 2\pi f_{RF} \quad (1.23)$$

D'autre parts, en considérant que le signal d'entrée  $V_{RF}(t)$  est de faible puissance, et qu'il vérifie la condition :  $A < V_T$ , alors nous pouvons réexprimer l'équation (1.22) en employant le développement limité de la fonction exponentielle afin d'obtenir :

$$i(t) = I_s \left[ \left( \frac{v_{RF}(t)}{nV_T} \right) + \frac{1}{2} \left( \frac{v_{RF}(t)}{nV_T} \right)^2 + \dots \right] \quad (1.24)$$

Par ailleurs, le circuit basse fréquence équivalent à la sortie du détecteur peut se présenter comme suit [8-9]:

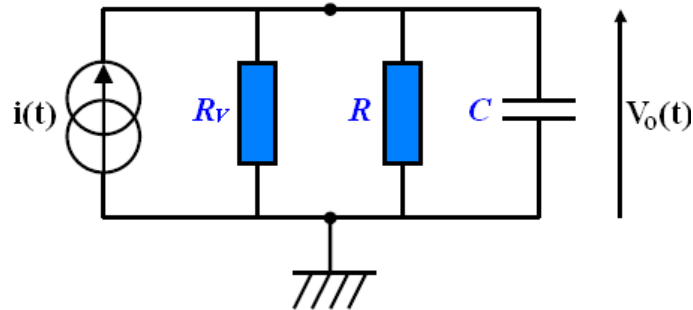


**Figure 1.6** - Schéma équivalent de la sortie du détecteur à base de diode Schottky.

La résistance dynamique de la diode, correspond à la résistance vidéo  $R_v$  [8]. Cette dernière avec la résistance  $R$  et le condensateur  $C$  forment un filtre passe-bas du premier ordre ayant une fréquence de coupure  $f_c$ :

$$f_c = \frac{R_v + R}{2\pi R_v R C} \quad (1.25)$$

Avec le choix d'une fréquence de coupure  $f_c$  faible par rapport à la fréquence RF d'entrée du détecteur, la tension de sortie  $V_o(t)$  sera donc proportionnelle aux composantes basses fréquences ou bande de base (BB) du courant  $i(t)$ , notamment au terme quadratique de l'équation (1.24).

Alors, par le remplacement de l'expression de la tension d'entrée RF donnée par (1.23) dans l'équation (1.24), et en ne tenant compte que du terme quadratique de l'équation, nous obtenons donc :

$$i(t) = \frac{I_s}{2} \left( \frac{A \cdot \cos(2\pi f_{RF} t)}{V_T} \right)^2 \quad (1.26)$$

Après une opération de filtrage passe-bas, la tension de sortie sera alors :

$$v_o(t) = \frac{R \cdot R_V}{R + R_V} \left( \frac{I_S}{4V_T^2} \right)^2 \cdot A^2 = \alpha \cdot P_{RF} \quad (1.27)$$

Le coefficient  $\alpha$  représente la sensibilité du détecteur qui est habituellement exprimée en Volt/Watt. D'après la formule, on peut constater que pour les faibles niveaux de puissance, le détecteur à diode réalise une détection de puissance, car la tension de sortie du détecteur est proportionnelle au carré de l'amplitude du signal d'entrée, autrement dit à la puissance du signal RF. Cependant sur une large plage dynamique de puissance, la caractéristique du détecteur à diode peut se présenter au figure 1.7, de la manière suivante :

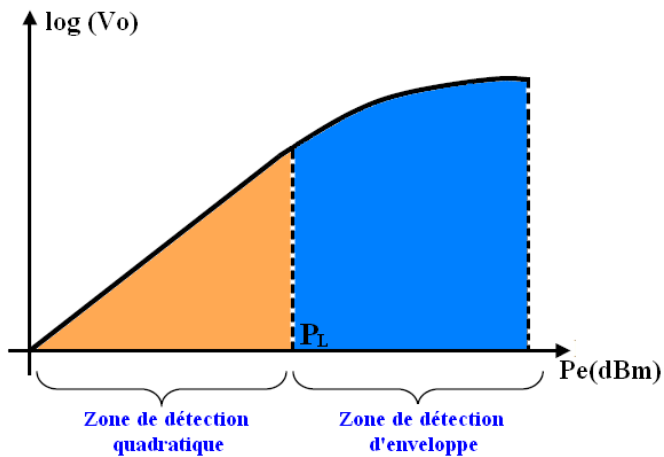


**Figure 1.7** - Caractéristique typique d'un détecteur à diode.

La figure 1.7 illustre la variation de la tension de sortie d'un détecteur à base de diode Schottky en fonction de la puissance RF injectée à l'entrée. D'après la figure ci-dessus, on peut distinguer deux types d'opération :

1- Pour  $P_e < P_L$  : le détecteur de puissance effectue une détection quadratique et permet ainsi de mesurer la puissance du signal RF injectée à l'entrée.

2- P<sub>e</sub> > P<sub>L</sub> : étant donné que la puissance d'entrée est plus élevée, les estimations faites antérieurement ne sont plus valables, alors la diode fonctionne en mode redresseur, et le détecteur de puissance réalise une détection d'enveloppe classique. Dans de tel cas, une correction de la tension de sortie est nécessaire afin d'augmenter la dynamique de mesure de puissance [8].

## 1.4. Les amplificateurs à faible bruit (LNAs)

### 1.4.1 Principe de fonctionnement et utilité

Un amplificateur à faible bruit ou LNA (Low Noise Amplifier) représente l'amplificateur de tête de la chaîne de réception. Il est souvent placé à proximité de l'antenne, afin d'amplifier les signaux utiles ayant un très faible niveau puissance à la sortie de cette dernière. Cependant, l'amplification du signal reçu par l'amplificateur doit répondre à deux critères importants : maintenir un gain stable et approprié tout en contrôlant la dégradation de la figure de bruit du récepteur. Autrement dit, un compromis entre le facteur de bruit et le gain est donc nécessaire dans la conception du LNA [1].

Généralement, le facteur de bruit  $F$  représentant la dégradation du rapport signal à bruit causé par les composants de la chaîne RF. Il est défini comme étant le rapport entre les  $SNR$  (Signal-to-Noise Ratio) à l'entrée et à la sortie du bloc :

$$SNR = \frac{SNR_{IN}}{SNR_{OUT}} \quad (1.28)$$

Habituellement dans le domaine des télécommunications, il est commun d'utiliser comme unité le décibel (dB), alors, dans ce cas, le facteur de bruit est plus communément nommé figure de bruit  $NF$  (Noise Figure), et il peut être s'exprime comme suit :

$$NF = 10 \log (F) \quad (1.29)$$

Par ailleurs, la figure de bruit globale d'une telle chaîne peut être déterminée par la formule de Friis (1.30). Cette dernière montre que plus le gain d'un amplificateur en amont est élevé, plus

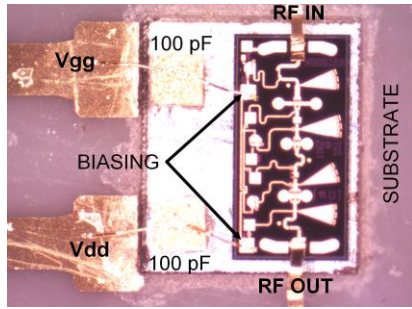
son influence sur le bruit global est significative. La conception d'un LNA doit donc être un compromis entre le facteur de bruit et le gain.

$$F = 1 + \sum_{k=1}^n \frac{F_k - 1}{\prod_{i=1}^{k-1} G_{Ai}} \quad (1.30)$$

#### 1.4.2 Spécifications typique d'un LNA à 60 GHz

Dans le cadre de notre projet de thèse, nous avons opté pour le LNA (TGA4600) de la compagnie TriQuint. Ce dernier possède un facteur de bruit acceptable  $NF = 4$  dB, ce qui permet de limiter significativement la contribution en bruit de la chaîne de réception. Un exemple de l'implantation de cet amplificateur faible bruit LNA sur un substrat en céramique utilisant la technologie MHMIC est illustré dans la figure 1.8. Les caractéristiques typiques à 60 GHz afin qu'il remplisse adéquatement son rôle sont également présentées au tableau 1 :

**Tableau 1.1-** Caractéristiques typiques d'un LNA à 60 GHz



<b>Technologie</b>	0.15 um 3MI pHEMT
<b>NF</b>	4 dB
<b>Gain</b>	13 dB
<b>Bande de fréquence</b>	57 - 65 GHz
<b>Impédance d'entrée et de sortie</b>	50 Ω
<b>Taux de retour en entrée et en sortie</b>	26 dB et 6 dB
<b>Isolation inverse</b>	20 dB
<b>Facteur de stabilité</b>	>1

**Figure 1.8** - Exemple d'implantation d'un LNA à 60 GHz (TGA4600)

#### 1.4.3 Problématique de la composante continue ou “DC offset”

La génération de composantes continues ou DC offset est une problématique très courante dans les récepteurs homodynes. Ces composantes apparaissent d'une manière directe dans la bande utile comme des signaux parasites.

Ce phénomène est généralement le résultat de deux principaux facteurs, le premier, est le niveau d'isolations entre l'OL (Oscillateur Local), les entrées du mélangeur et le LNA. En effet,

cette isolation n'est pas idéale, et par conséquent, une fuite provenant de l'OL peut avoir lieu. Cette dernière est généralement due au couplage direct ou indirect par le substrat et elle peut apparaître également à l'entrée du LNA et même parfois à l'entrée du mélangeur.

Ce problème est représenté dans la figure 1.9 où uniquement la voie Q est considérée. Cette fuite liée à l'OL est présentée à l'entrée du LNA et du mélangeur, est par la suite mélangée avec le signal provenant de l'OL lui-même, pour générer une composante parasite autour de la fréquence zéro (DC composante) [1] [11].

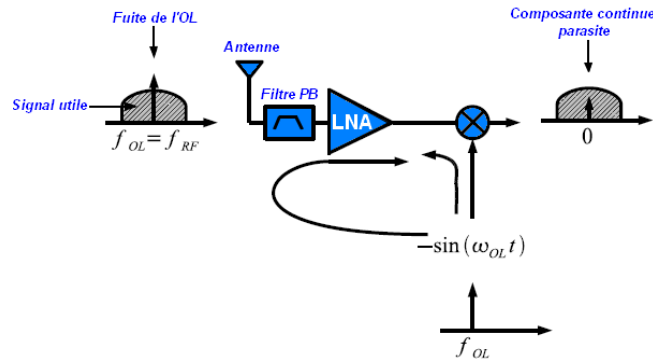


**Figure 1.9** - Problème de la fuite d'oscillateur local (OL) dans une chaîne de réception homodyne.

Par ailleurs, le même phénomène peut se reproduire quand les fortes interférences présentent sur l'antenne peuvent traverser le LNA pour se rendre aux entrées du mélangeur et ensuite se multiplier avec lui-même [1][10]. La figure 1.10 illustre bien ce phénomène, où qu'une seule voie Q est considérée.

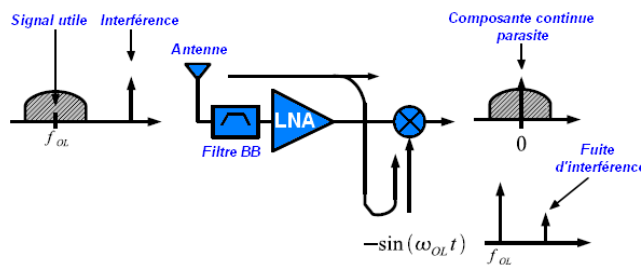


**Figure 1.10** - Problème de fuite des signaux parasites vers l'oscillateur local (OL) dans une chaîne de réception homodyne.

## 1.5. Le réseau d'antennes

### 1.5.1 Généralités

L'antenne est un dispositif permettant de rayonner (émission) ou de capter (réception) des ondes électromagnétiques. Elle sert d'interface entre les ondes électromagnétiques qui se propagent dans les structures de guidages (guides d'ondes, lignes de transmission) et les ondes qui se propagent dans l'espace libre [12].

Le choix d'un type d'antenne dépend surtout du type d'application envisagée. Les facteurs les plus fondamentaux à considérer dans une antenne sont entre autres, la puissance d'émission qui fixe la portée du système, la directivité, la taille et la facilité d'intégration de l'antenne dans un système complet.

Il existe plusieurs types d'antennes, les antennes filaires, les antennes patchs et les antennes à ouverture. Ces derniers ont été considérées pendant longtemps comme les seules susceptibles de montrer de bonnes performances pour les applications en ondes millimétriques. Cependant, de récents développements ont montré que les antennes patchs disposent également de très bonnes performances aux fréquences millimétriques [13-14].

Pour les applications millimétriques sans fil, courtes distances et haut débit, ces antennes répondent parfaitement à nos exigences en termes de coût de production, de taille, et de facilité d'intégration dans le prototype de frontale radiofréquence réalisé en technologie MHMIC.

### 1.5.2 Directivité, Efficacité et Gain

La directivité d'une antenne désigne généralement la façon dans laquelle une antenne concentre son rayonnement dans certaines directions de l'espace. Elle est définie comme le rapport entre l'intensité de rayonnement ( $U(\theta, \phi)$ ) dans une direction donné et l'intensité de rayonnement moyenne d'une antenne isotrope ( $U_0$ ). La densité de rayonnement de cette dernière est égale à la puissance rayonnée par l'antenne ( $P_R$ ) divisée par  $4\pi$  [12].

$$D(\theta, \phi) = \frac{U(\theta, \phi)}{U_0} = \frac{4\pi \cdot U(\theta, \phi)}{P_R} \quad (1.31)$$

Alors, la directivité est une grandeur qui permet de décrire le rayonnement de l'antenne par rapport à un rayonnement isotrope. Donc, plus l'antenne est directive, plus le rayonnement est dirigé vers une seule direction.

L'efficacité totale d'une antenne est employée pour prendre en compte les pertes à l'entrée du dispositif et les pertes liées aux conducteurs. Elle est égale au rapport entre la puissance rayonnée ( $P_{Ray}$ ) et la puissance incidente à l'entrée de l'antenne ( $P_I$ ). Ce rapport est souvent utilisé pour prendre en considération les pertes de l'antenne incluant, la puissance perdue dans la métallisation (effet Joule) ou dans le substrat, et la puissance réfléchie à l'entrée en raison de la désadaptation d'impédance de l'antenne. En générale, à part de l'efficacité totale, nous parlons également de l'efficacité de rayonnement qui traduit le rapport entre la puissance rayonnée et la puissance transmise à l'antenne ( $P_T$ ). Toutes ces puissances sont illustrées, ci-dessous, à la figure 1.11.

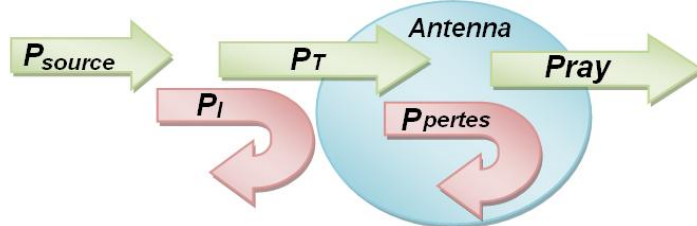


**Figure 1.11 - Efficacité de rayonnement et efficacité de l'antenne**

$$\eta_{tot} = \frac{P_{Ray}}{P_I} = \eta_{ref} \eta_{ray} \quad \text{où} \quad \eta_{ray} = \frac{P_{Ray}}{P_T} \quad \text{et} \quad \eta_{ref} = (1 - |\Gamma|^2) \quad (1.32)$$

$\eta_{ref}$  représente la désadaptation de l'impédance d'entrée de l'antenne ( $Z_{in}$ ) et la source ( $Z_0$ ).  $\Gamma$  est le coefficient de réflexion à l'entrée de l'antenne et est donné par [15] :

$$\Gamma = \frac{Z_{in} - Z_0}{Z_{in} + Z_0} \quad (1.33)$$

Le gain d'une antenne, dans une direction donné, est défini comme le rapport de l'intensité de rayonnement de l'antenne, par l'intensité de rayonnement d'une antenne isotrope idéale, dans cette direction. Les deux antennes sont supposées être alimentées par la même puissance. Cette expressions se résume à [15]:

$$G(\theta, \phi) = \frac{4\pi \cdot U(\theta, \phi)}{P_I} \quad (1.34)$$

Ainsi, le gain est lié à la directivité par l'intermédiaire de l'efficacité :

$$G(\theta, \phi) = \eta_{tot} \cdot D(\theta, \phi) \quad (1.35)$$

## Références

- [1] Ioan BURCIU, 2010. “Architecture de récepteurs radiofréquences dédiés au traitement bibande simultané”. Thèse de doctorat, l’Institut National des Sciences Appliquées de Lyon, 210p.
- [2] Moussa Hassan BARAKAT, 2008. “Dispositif radiofréquence millimétrique pour objets communicants de type smart dust”. Thèse de doctorat, Institut de Microélectronique, Electromagnétisme et Photonique, INPG, MINATEC, 212p.
- [3] Tatou, S.O. 2005. “Nouveau récepteur six-port en ondes millimétriques”. Thèse de doctorat, Montréal, École polytechnique, 209p.
- [4] Li, J., R.G. Bosisio et K. Wu. 1995. “Computer and Measurement Simulation of a New Digital Receiver Operating Directly at Millimeter-Wave Frequencies”. IEEE Transactions Microwave Theory Techniques, 43, 2766-2772.
- [5] Engen, G.F. et C.A. Hoer. 1972. “Application of an Arbitrary 6-Port Junction to Power-Measurement Problems”. IEEE Trans. Instrumentation and Measurement, IM-21, 470-474.

- [6] Engen, G.F. 1977. "The Six-Port Reflectometer: An Alternative Network Analyzer". IEEE Trans. Microwave Theory Technique, MTT-25, 1075-1077.
- [7] Tatu, S. O., E. Moldovan, K. Wu, R. G. Bosisio. et T. Denidni, (2005). "Ka-Band Analog Front-End for Software-Defined Direct" Conversion Receiver. IEEE Transactions on Microwave Theory and Techniques, vol. 53, no 9, 2678 - 2776.
- [8] Sara ABOU CHAKRA, 2004. "La Boucle Locale Radio et la Démodulation directe de signaux larges bandes à 26 GHz". Thèse de doctorat, Télécom ParisTech ENST, 144p.
- [9] Woods, D. 1979. "Analysis and calibration theory of the general six-port reflectometer employing four amplitude detector", Pro IEEE, Vol. 126, pp. 221-228.
- [10] Fredrick, JD; T. Itoh. 2001. "Recent developments in RF front ends based upon active antenna concepts". TELSIKS 2001, pp. 3-9.
- [11] Fredrick, J.D., Y. Qian et T. Itoh. 2000. "Novel Design Technique for A Low Noise Receiver Front End With Integrated Circularly Polarized Patch Antenna". 30th European Microwave, Conference Proceedings, vol. 2 pp. 333-336.
- [12] Stutzman W. L., et G.A. Thiele. 1981. Antenna Theory and Design, John Wiley, New York.
- [13] Park, J., Y. Wang et T. Itoh. 2003. "A 60GHz Integrated Antenna Array for High-Speed Digital Beamforming Applications". Microwave Symposium Digest, 2003 IEEE MTT-S International, vol. 3, pp. 1677-1680.
- [14] J.R. JAMES & P.S. HALL, (1989).Handbook of Microstrip Antennas Volume 1. Peter Peregrinus ltd., London UK
- [15] Lee, K.F. and Chen, W., (1997). Advances in Microstrip and Printed Antennas John WILEY & Sons, Inc.

## **CHAPITRE 2 :**

### **COMPLETE CHARACTERIZATION OF NOVEL MHMICS FOR V BAND COMMUNICATION SYSTEMS**

**C. Hannachi, D. Hammou, T. Djerafi, Z. Ouardirhi, and S.O. Tatou**

Journal of Electrical and Computer Engineering, vol. 2013, pp.1-7, October 2013

**Résumé :** Dans ce chapitre nous avons présenté les différents circuits passifs conçus pour opérer à la bande de fréquence de 60 GHz en adoptant la technologie MHMIC (Miniaturized Hybrid Microwave Integrated Circuit). Ces circuits incluent, le coupleur hybride H90°, le coupleur en anneau (rat-race), le diviseur de puissance de type Wilkinson et enfin l'interféromètre six-port qui sera la combinaison d'un diviseur de puissance et trois coupleurs hybrides H90°. Tous ces circuits ont été caractérisés expérimentalement en termes de paramètres de dispersion S dans la bande millimétrique considérée, de 60 à 65 GHz. Comme technique de calibration, nous avons opté pour la calibration TRL (Thru, Reflect, Line) où nous avons préféré fabriquer notre propre kit de calibration et de l'intégré avec les circuits à caractériser. Cette démarche nous permet d'éviter l'utilisation des standards commerciaux (ISS), connus pour leurs coûts trop élevés et qui sont conçus généralement sur un différent standard de substrat. Cette première fabrication est considérée comme une étape préliminaire essentielle à la conception de notre futur prototype de la frontale radiofréquence, car elle nous permet de connaître avec exactitude les performances de l'interféromètre six-port, utilisé comme un démodulateur direct en bande millimétrique.

## Abstract

This paper presents the characterization results of several new passive millimeter wave circuits integrated on very thin ceramic substrate. The work is focused on the design and characterization of a novel rounded Wilkinson power divider, a 90° hybrid coupler, a rat-race coupler, and of a novel six-port (multi-port) circuit. Measurements show the wideband characteristics, allowing therefore their use for multi Gb/s V-band wireless communication systems.

### 2.1. Introduction

THE use of the 60-GHz band has attracted a great deal of interest over the last few decades, especially for its use in future compact transceivers dedicated to high-speed wireless applications in indoor environments (57 – 64 GHz) [1], [2], [3]. In this context, intensive research have been done to further develop new millimeter-wave components for high data rate wireless communications according to the IEEE 802.15.3c standard. As previously demonstrated, the six-port technology offers an excellent alternative to conventional receiver architectures, especially at millimeter-wave frequencies [4], [5], [6].

Nowadays, there are few promising high-quality fabrication technologies, yielding potentially low-cost millimeter-wave components, such as the Monolithic Microwave Integrated Circuit (MMIC) on GaAs or SiGe for large-scale production, and the Miniature Hybrid Microwave Integrated Circuit (MHMIC) technology on very thin ceramic substrates, for small-scale production and prototyping [7], [8].

Moreover, several technologies have been intensively used for the millimeter wave circuit design and in house prototype fabrication. We particularly note the coplanar, the Substrate Integrated Waveguide (SIW), and the microstrip technology. The coplanar technology assures high-quality component design, but is not well suited for low-cost production due to the difficulties in automating wire-bonding implementation, necessary for obtaining repeatable performances. On the other hand, the SIW technology assures high-quality component design on thin ceramics [9] or the design of optimal transitions from planar to standard rectangular waveguides [10]. For further circuit miniaturization, the microstrip technology on very thin, high relative permittivity substrate is recommended.

As known, the microstrip line width is related to the characteristic impedance, substrate relative permittivity and its thickness. It is to be noted that, due to reduced guided wavelength in high permittivity ceramic substrates, in order to keep the required circuit aspect ratio (guided wavelength versus the line width), the substrate must be as thin as possible. The optimal choice for frequencies greater than 60 GHz is the 127  $\mu\text{m}$  thick alumina substrate, which is also easily compatible with the usual 100  $\mu\text{m}$  thick MMIC active components, to be integrated with planar passive MHMICs. The MMIC chips are placed in rectangular cuts on ceramics, on the top of the same metallic fixture, allowing thermal dissipation and easy wire-bonding with MHMIC components, which are practically at the same height.

Initial designs and circuit characterization results of several MHMIC passive circuits on very thin ceramic substrate, designed for advanced millimeter wave systems operating in 60 – 90 GHz band, have been published few years ago [11].

This paper presents novel circuit designs, together with major improvements obtained in fabrication and characterization process in recent years.

## 2.2. Calibration Techniques and Standards

Measurement performance mainly depends on the accuracy of the calibration technique and its standards used for correcting the imperfections of the measurement system. These imperfections depend on several factors such as non-ideal nature of cables and probes, and the internal characteristics of the vector network analyzer (VNA) itself. In order to simplify calibration procedures and to obtain more accurate and reliable measurement by introducing much smaller systematic errors, the on-wafer calibration and measurement with pico-probes were adopted.

Typically, on-wafer calibration standards are fabricated either on the wafer including the device under test (DUT) or on a separate impedance standard substrate (ISS). The reference plane is usually taken at the probe tips. Nevertheless, for the DUT measurement in microstrip technology, on-wafer standards fabricated on the same wafer as the DUT are required since the probe-to-standard transition can be designed to be very similar to the transition to the DUT. It sometimes happens that the transition between the probe tips and the coplanar line end is not well matched and parasitic and some wave modes occur at the contact of the probe tips. By

taking the probe tips as measurement reference plane, the errors due to this transition are not corrected, and may affect the measurement results.

Different calibration procedures or standards have been used for measuring microstrip based circuits; among the most commonly used are line-reflect-match (LRM), line-line-reflect-match (LLRM), and thru-reflect-line (TRL) [12].

One of the most robust and popular technique is the TRL calibration, that is well suited to the on-wafer measurements at millimeter wave frequencies. According to previous comments, the reference plane is considered at the middle of the thru line. The TRL calibration was done using on-wafer microstrip structures and the TRL algorithm supported by our vector network analyzer E8362B of Agilent Technologies.

A non-zero length thru is used to extend the reference plane a physical distance of 2286  $\mu\text{m}$  into the microstrip line in order to ensure direct measurement at the desired reference plane of the device, eliminating further de-embedding and its associated uncertainties.

One microstrip delay line of 477  $\mu\text{m}$  length is used to cover the whole considered frequency band. Generally, in order to avoid phase uncertainties, for TRL calibration, the electrical length of the line standard is maximum 180° at the highest operating frequency.

For the reflect standard, the designer can chose between the open and the short. In our opinion, the open standard is a better option at millimeter wave frequencies, due to the complex nature of the short circuit design having repeatable performances in microstrip technology, especially when via-holes are used.

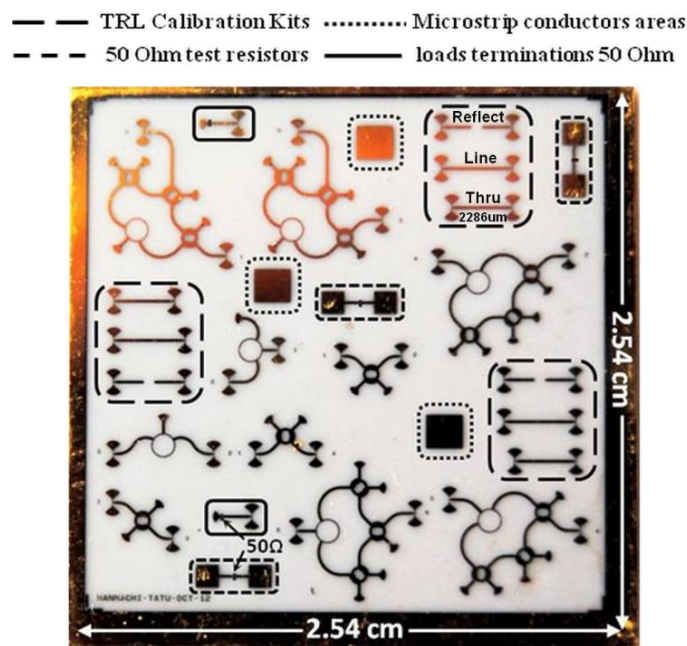
In our designs, millimeter wave RF short circuits are implemented with quarter wavelength sectors, avoiding via-holes.

Figure 2.1 shows a microphotograph of typical fabricated circuits, including several identical TRL standard calibration kits. In order to optimize the fabrication cost and the measurement time, a maximum number of circuits to be characterized are fabricated on each ceramic die of 2.54 cm x 2.54 cm.

Due to the vulnerability of the very thin gold layer metallization (1  $\mu\text{m}$ ), multiple identical kits have been fabricated in order to ensure successful calibration before each measurement. Small microstrip conductor areas were also added on die in order the properly align the pico-

probes before measurement. In addition,  $50\ \Omega$  microstrip terminations and resistors test kits, were used to verify the required value of  $100\ \Omega$  per square for the integrated loads.

Typical measurement results over 60 – 90 GHz band of a microstrip line, after calibration, show matching results better than -50 dB at both ports, and a quasi-perfect transmission of 0 dB (with no more than 0.5 dB ripple, the intrinsic error of the VNA) when the pico-probes are properly aligned and positioned.



**Figure 2.1** - Microphotograph of the fabricated circuits on thin ceramic substrate of 2.54 cm x 2.54 cm.

### 2.3. Basic Circuit Characterization

In order to integrate complete millimeter wave front-ends on ceramic substrates, the first step is to design basic circuits, such as couplers and power dividers/combiners. These components will be further utilized in antenna array and six-port down-converter or direct modulator designs.

As mentioned, the MHMICs have been designed and fabricated on a very thin ceramic substrate having a relative permittivity of 9.9 and a thickness of 127  $\mu\text{m}$ . Advanced Design System (ADS) version 2011.05 of Agilent Technologies was used for circuits design and

simulation. In order to perform on-wafer measurement of the S parameters, several circuits have been integrated in the same alumina substrate of 2.54 cm x 2.54 cm size, as see in Figure 2.1.

The symmetry of circuits is used to reduce the number of fabricated circuits required for complete characterization. For example, the full characterization of four port couplers requires minimum three different circuits due to the two-dimensional symmetry. Only two circuits are needed for the Wilkinson power divider, because of its one-dimension symmetry. Finally, five circuits are requested for the full characterization of our six-port design. All these circuits can be easily identified in Figure 2.1. The unused ports are connected to integrated  $50\Omega$  loads.

Even if the allowed frequency band starts from 57 GHz, all circuits are measured from 60 GHz because of measurement set-up capabilities (WR-12 rectangular waveguides modules for the 60 – 90 GHz millimeter wave extension of the VNA). However, the results can be extrapolated in the 57 – 60 GHz band by symmetry and comparison with electromagnetic simulations.

### 2.3.1. $90^\circ$ Hybrid Coupler

Figure 2.2 shows the microphotograph of the  $90^\circ$  hybrid coupler, prepared for port 1 to port 3 measurements

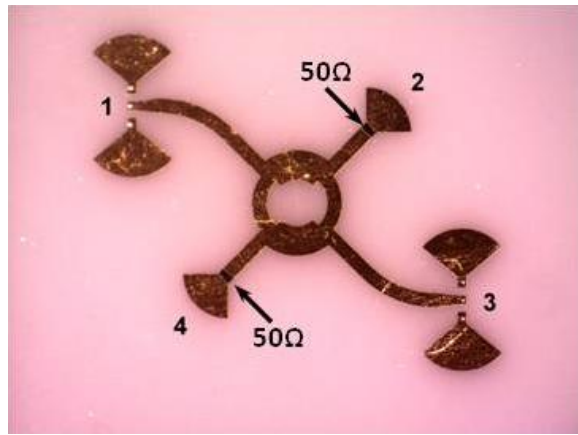


**Figure 2.2** - Microphotograph of the branch-line coupler

As usual in our millimeter wave designs, the shape of the circuit is rounded, ensuring better S parameter performances. The microstrip line widths are 126  $\mu\text{m}$  for the  $50\Omega$  microstrip line, 100  $\mu\text{m}$  for central line of the coplanar input, and 250  $\mu\text{m}$  for  $50/\sqrt{2}\Omega$  quarter wave line inside the

coupler. The diameter of the coupler, measured between the centers of diametrically opposite microstrip lines is around 625  $\mu\text{m}$ .

As explained earlier, all via-holes are replaced by wide-band RF short circuits. Details, such as 50  $\Omega$  integrated resistor or the trace of the pico-probes on gold layer metallization after measurement, can be seen in the picture.

Figures 2.3 to 2.5 show measurement results for S parameter magnitudes and phases of the circuit. Measurements are performed for  $S_{21}$ ,  $S_{31}$ , and  $S_{41}$  on three different circuits (see Figure 2.1, the secondary diagonal).

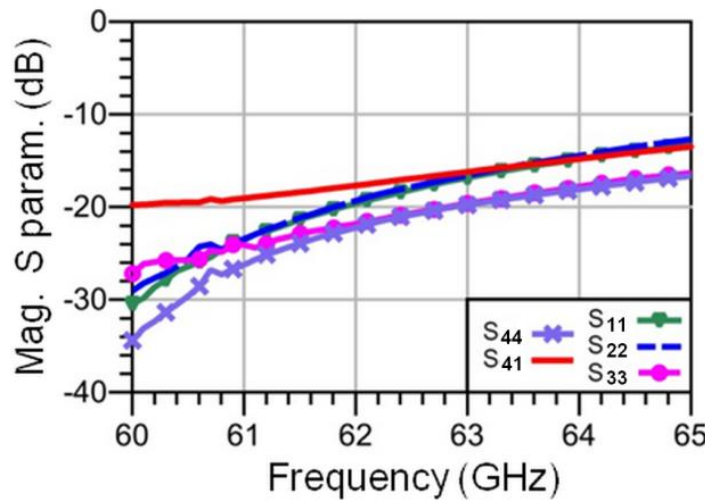


**Figure 2.3** - Measured input return loss for the 90° hybrid coupler.

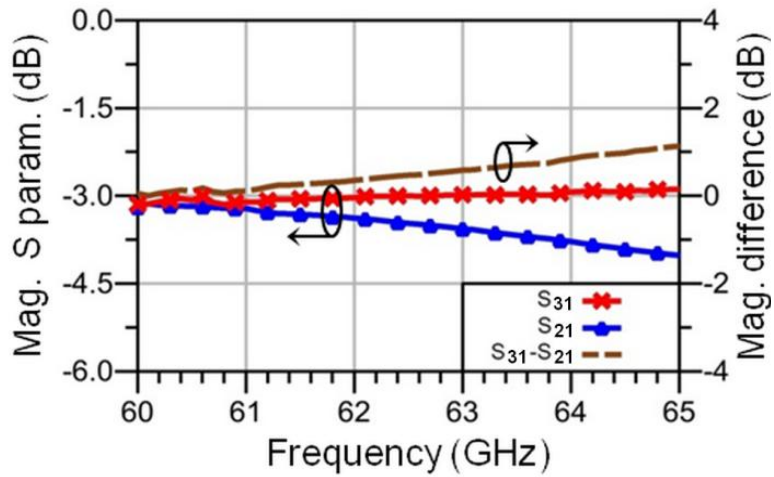


**Figure 2.4** - Measured transmission S parameter magnitudes for the 90° hybrid coupler.

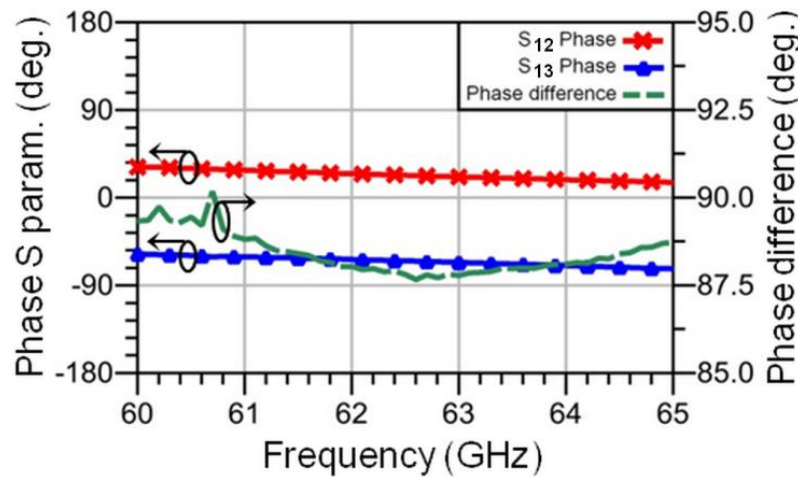


**Figure 2.5** - Measured transmission S parameter phase difference for the 90° hybrid coupler.

As seen in Figure 2.3, the measured return losses are better than 26 dB at 60 GHz, and better than 14 dB at the highest frequency allowed for V-band communications, 64 GHz.

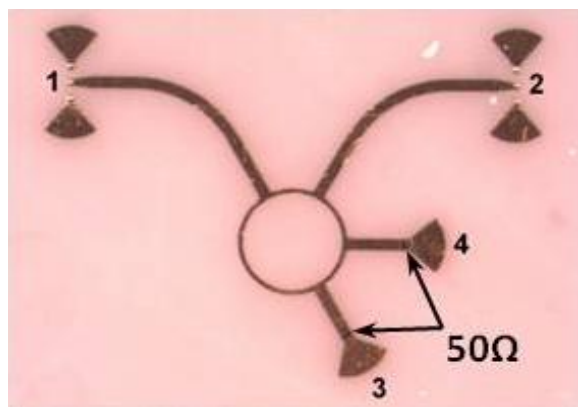
The isolation,  $S_{41}$ , is around 20 dB at 60 GHz and has comparable values with return losses from 63 GHz. The measured transmitted power is well splitted between the two outputs, especially around the central frequency allowed for V-band communications (60.5 GHz). The magnitude unbalancing is practically zero at 60 GHz and less than 1 dB at 64 GHz, as it can be seen in Figure 2.4.

Figure 2.5 shows that the phase difference between the two outputs is around  $89^\circ \pm 1^\circ$  from 60 to 65 GHz. Because in a six-port circuit the signal path crosses over two such couplers, these low values of magnitudes and phases unbalances are considered appropriate for modulation/demodulation schemes having up to 16 symbols.

### 2.3.2. Rat-Race Coupler

A rat-race coupler has been also designed and fabricated on a separate die, similar of that illustrated in Figure 2.1, along with other circuits. Multiple circuits have been fabricated to measure complete S parameters of the coupler. As for the previous case, the unused ports are connected to integrated  $50\Omega$  loads.

Figure 2.6 shows the micro-photograph of this rat-race coupler, prepared for port 1 to port 2 measurements. In order to have a better idea of circuit size, let's see same dimensions: the line widths are 126  $\mu\text{m}$  for  $50\Omega$  microstrip lines and 55  $\mu\text{m}$  for  $50\sqrt{2}\Omega$  characteristical impedance of the circular shape. The coupler circumference is equal to six quarter wavelengths and its diameter is 740  $\mu\text{m}$ . Two integrated  $50\Omega$  millimeter wave loads are connected to ports 3 and 4. Similar details, as in the previous circuit case are visible on the picture: the  $50\Omega$  integrated resistors connected at unused ports and the traces of the pico-probes on gold layer metallization after measurement.



**Figure 2.6** - Micro-photograph of the rat-race coupler.

Figures 2.7 to 2.9 show measurement results for S parameter magnitudes and phases of this rat-race coupler. Figure 2.7 shows the measured input return loss and isolation values are better than 15 dB over the whole considered frequency band, from 60 to 65 GHz. The isolation  $S_{14}$  reaches an exceptional value, of at least 35 dB, due to the constant characteristic impedance over the ring. There are no steps in line width, which improves millimeter wave isolation. As regards with the transmitted power plotted in Figure 2.8, a quasi-equal split between the two outputs over the whole frequency range of interest is observed. The measured unbalancing is less than 0.5 dB, comparable with the intrinsic error of the VNA.

Figure 2.9 shows the measurement of the transmission phase difference between the output ports. The phase difference value is equal to  $180^\circ$ , with a corresponding of phase error of  $\pm 5^\circ$  over the considered frequency band. This error is close to  $0^\circ$  at the central frequency allowed for V-band communications (60.5 GHz).

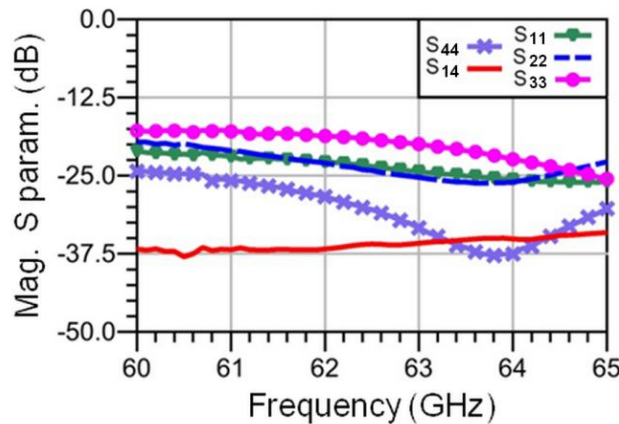


**Figure 2.7** - Measured input return loss for the rat-race coupler.

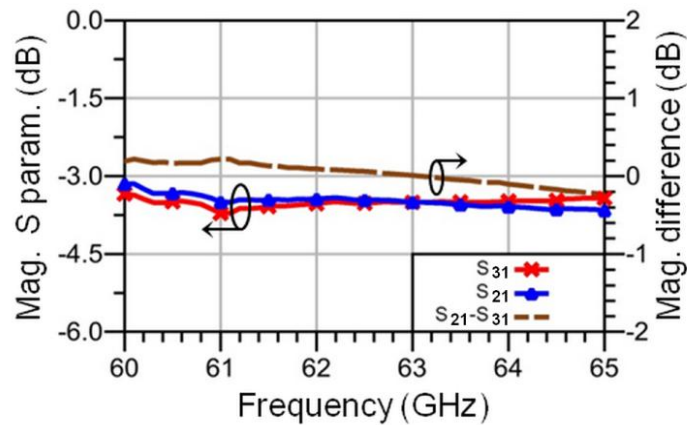


**Figure 2.8** - Measured transmission S parameter magnitudes for the rat-race coupler.

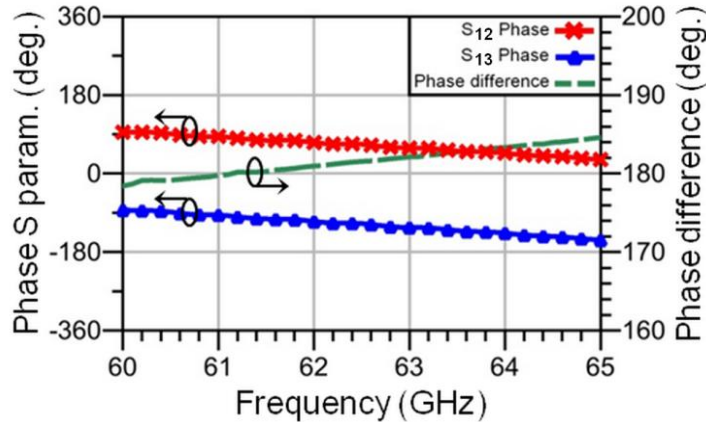


**Figure 2.9** - Measured transmission S parameter phase difference for the rat-race coupler.

The rat-race coupler performances are ideal to design a V-band six-port based down-converter using the quasi-conventional architecture (with two pairs of anti-parallel diodes connected to rat race quadrature outputs), similar to those presented in [13] for automotive radars, at 77 GHz.

It is known that a conventional mixer uses such a rat-race coupler and a pair of anti-parallel diodes. The six-port down-converter design is completed by adding a  $90^\circ$  hybrid coupler to LO port and a Wilkinson at RF port and two diode mixers [14].

### 2.3.3. C. Wilkinson Power Divider/Combiner

Figure 2.10 shows the micro-photograph of a novel rounded shape Wilkinson power divider [15] along with the transition from the coplanar wave to the microstrip line, requested for on wafer measurements. This circuit of Figure 2.10 is prepared for the port 2 to port 1 measurement.

A second circuit, fabricated on the same ceramic die (see Figure 2.1), is used to measure isolation between ports 2 and 3. In order to avoid via holes, as in previous measurements, the  $50\ \Omega$  loads uses a quarter wavelength open stub as millimeter wave RF short-circuit (see port 3).

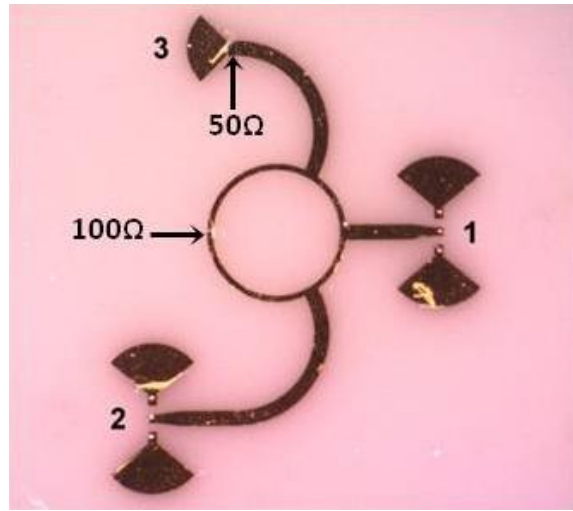


**Figure 2.10** - Microphotograph of the Wilkinson power divider/combiner.

Figures 2.11 to 2.13 show measurement results of the novel Wilkinson power divider/combiner S parameters (magnitude and phase).

As seen in Figure 2.11, the measured return losses have very good values. The port 2 return loss result is probably due to deviations from  $50\ \Omega$  values of the integrated load in the corresponding measurement circuit. However, due to the symmetry of the Wilkinson, the results must be closer to those obtained at port 3 using the second circuit. The isolation between two output/input ports of the divider/combiner,  $S_{23}$ , reaches also a very good value of around 25 dB over the whole band.

The power is almost equally split over the band, as illustrated in Figure 2.12; the magnitude unbalance is around 0.1 dB.

The phase difference between the two outputs is less than  $2^\circ$  over the considered band, as shown in Figure 2.13.

The glitches at 60.5 GHz are due to an internal error of our VNA' millimeter wave heads, which cannot be totally cancelled by calibration. It remains in the tolerance measurements of VNA, for both magnitude and phase measurements.

When the power divider circuit is part of a six-port, same conclusion as for previous circuits: the low values of magnitudes and phases unbalances are considered appropriate for the use of the six-port in modulation/demodulation schemes having up to 16 symbols.

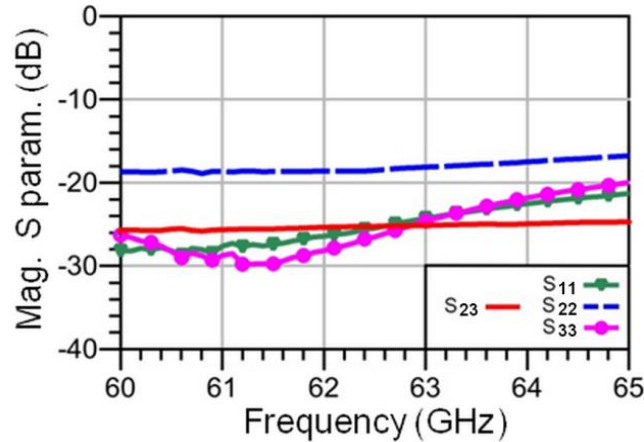


**Figure 2.11** - Measured return loss for the Wilkinson power divider/combiner.

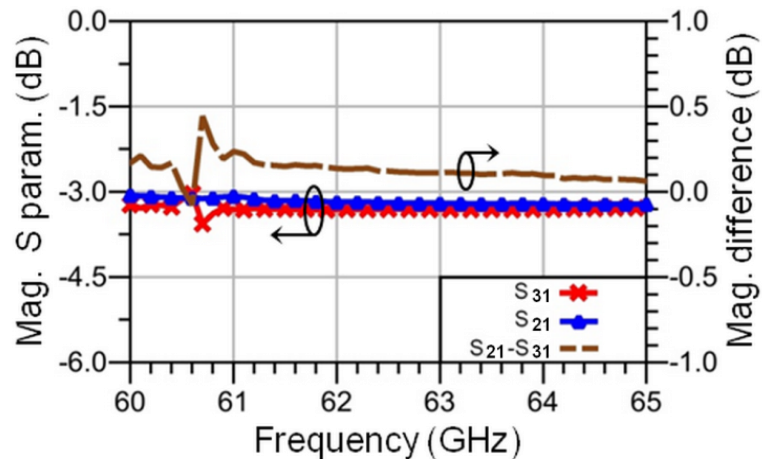


**Figure 2.12** - Measured transmission S parameter magnitudes for the Wilkinson power divider/combiner.

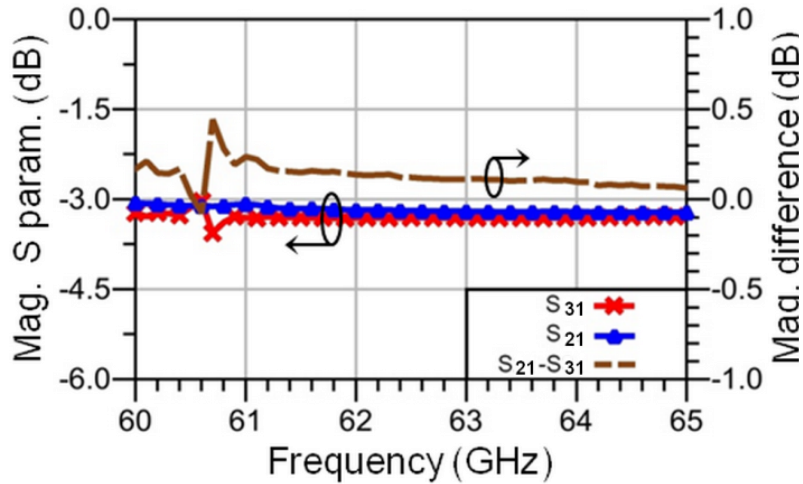


**Figure 2.13** - Measured transmission S parameter phase difference for the Wilkinson power divider/combiner

## 2.4. Six-port Circuit Characterization

Six-port (multi-port) quadrature down-conversion and direct modulation is an innovative approach in millimeter wave technology. A complete theory, validated by various simulations and measurements of V-band direct conversion receivers, has been published in recent years [14], [16].

Figure 2.14 shows the block diagram of the proposed six-port, composed by a Wilkinson power divider and three 90° hybrid couplers. As usually noted in all our previous publications, in a six-port down converter, the port 6 is connected to the RF signal and the port 5 is connected to the LO signal; the other four output ports (1, 2, 3, and 4) are connected to power detectors [14].

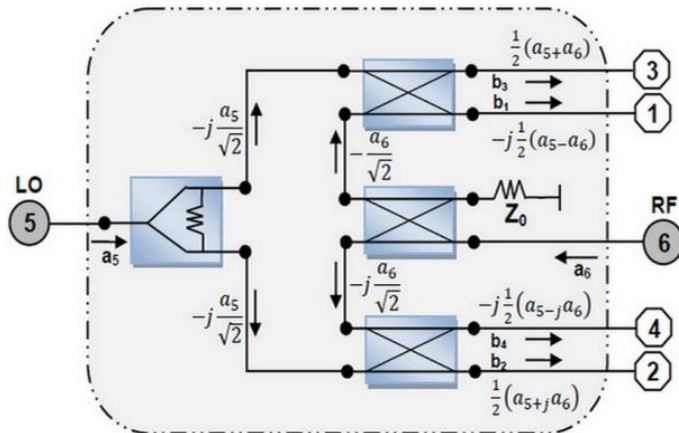


**Figure 2.14** - Six-port circuit block diagram.

In down-conversion techniques, it has been demonstrated that the six-port technology allows improved results in terms of conversion loss and requires reduced LO power, as compared to the conventional methods (as low as -20 to -25 dBm to perform an efficient frequency conversion) [14]. On the other hand, a conventional diode mixer using anti-parallel diodes acting at LO-driven switches requires around +10 dBm LO power for the same conversion loss. The excellent isolation between the six-port RF inputs is another important advantage versus the conventional approach [14].

A novel six-port circuit, having an improved symmetry and rounded shapes, has been designed using the novel Wilkinson power divider/combiner and the  $90^\circ$  hybrid couplers presented in previous sections III.C and III.A, respectively. The central design frequency is 60.5 GHz, in the middle of allowed band of 57 – 64 GHz.

Measurements are performed, as explained for other circuits from 60 GHz, due to our measurement equipment capabilities. Once again, extrapolation of measurements and comparison with simulations help us to estimate the circuit behavior from 57 to 60 GHz.

The microphotograph in Figure 2.15 shows the six-port circuit prepared for port 2 to port 5 measurements. As requested, all other ports are terminated by adapted loads, integrated on the same substrate. The outer six-port dimensions are approximately 6.5 mm x 6.5 mm.

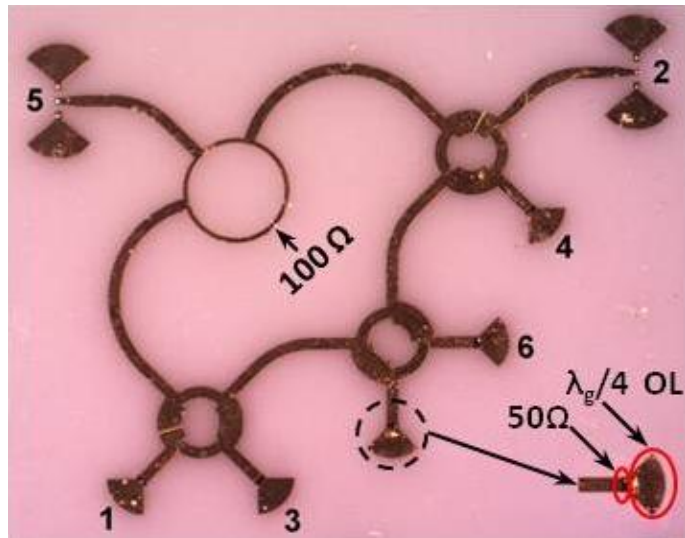
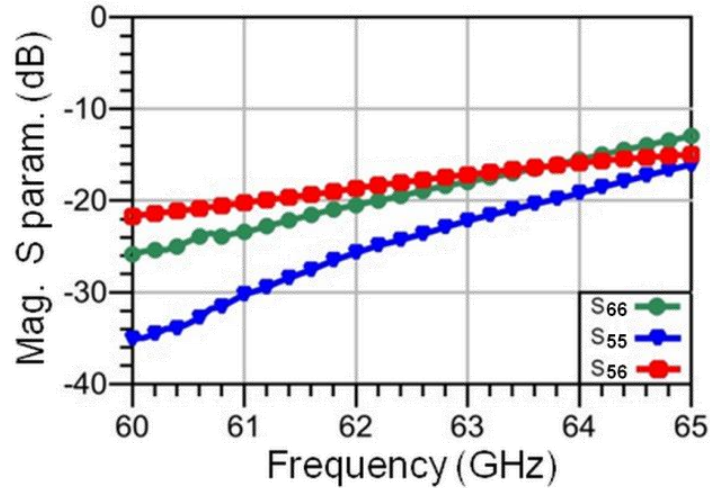


**Figure 2.15** - Micro-photograph of the novel millimeter wave six-port in a typical S parameter measurement configuration.

In order to measure the most important six-port S parameters (such as RF – LO ports isolation  $S_{65}$ , input match at ports, power transmission between the RF and LO ports to the outputs, and the phase difference between transmitted signals), five six-port circuits have been integrated in the same alumina die, along with other basic circuits and required calibration standards (see Figure 2.1).

Figures 2.16 to 2.21 show some typical measurement results, according to the port numbers specified in Figures 2.14 and 2.15.

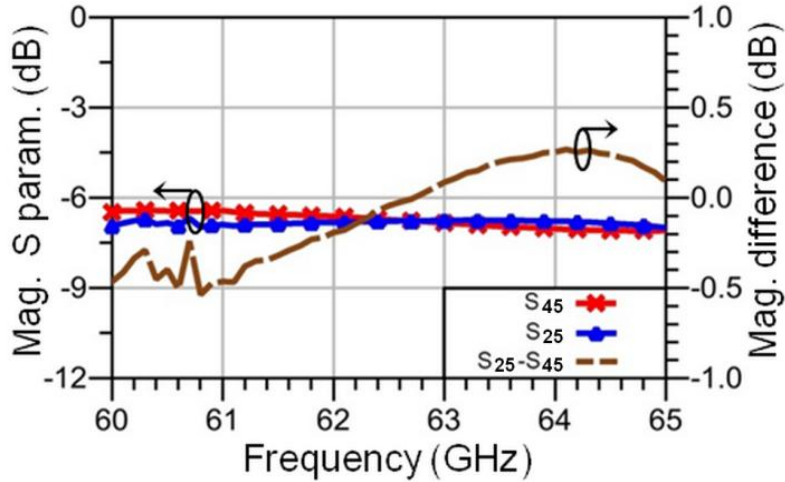
Figure 2.16 shows the measured return loss at port 6 (RF input) and port 5 (LO input), and isolation between them. At the central operating frequency of V-band systems all values are better than 20 dB. In addition, the measured values are better than 15 dB at the highest frequency allowed for V-band communications, 64 GHz.



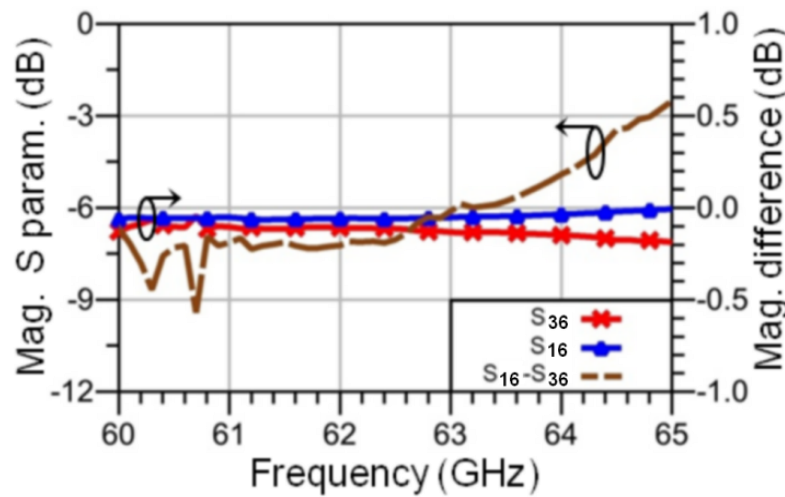
**Figure 2.16** - Measured RF inputs return loss and isolation for the proposed six-port

Figure 2.17 shows the power splitting between the LO port and two adjacent output ports,  $S_{25}$  and  $S_{45}$ . As compared to the theoretical value of -6 dB, very good results are obtained over the band. The supplementary insertion loss is around 1 dB at the central frequency and reaches 1.5 dB at the edge. The magnitude unbalance is close to 0 dB at 62.5 GHz and less than 0.5 dB over the entire band.

The power splitting between the RF port (port 6) and two adjacent output ports,  $S_{16}$  and  $S_{36}$  is also shown in Figure 2.18. Good results have been obtained over the considered frequency band. These results show less than 1.5 dB of supplementary insertion loss, while the magnitude unbalance between requested ports (port 1 and port 3) don't exceed 0.6 dB in the whole frequency band of interest.



**Figure 2.17** - Typical measured transmission magnitudes ( $S_{25}$ ,  $S_{45}$ ) for the proposed six-port.

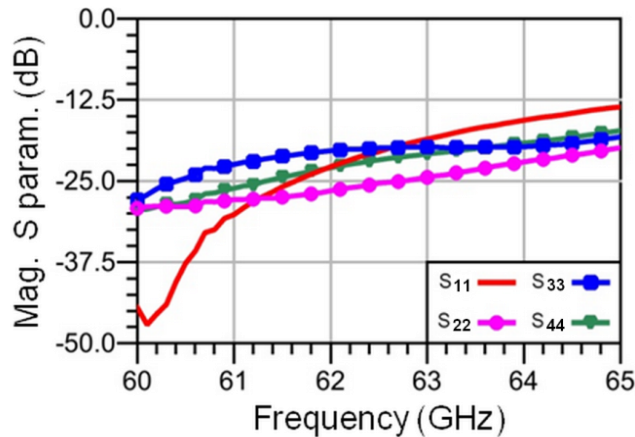


**Figure 2.18** - Typical measured transmission magnitudes ( $S_{16}$ ,  $S_{36}$ ) for the proposed six-port.

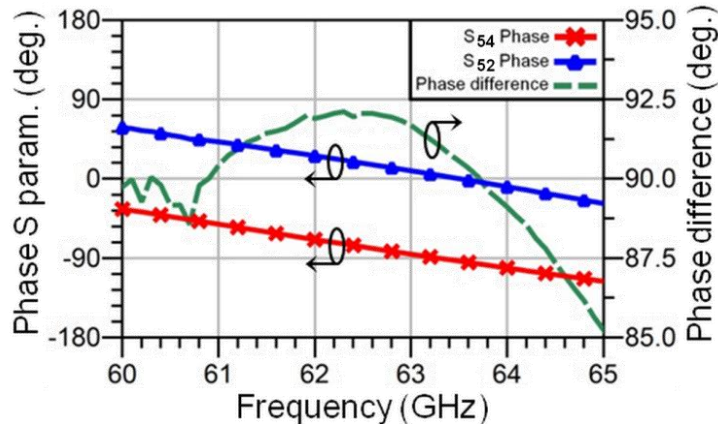
The measured return losses at output ports are illustrated in Figure 2.19. At the central operating frequency of V-band systems all values are better than 25 dB, keeping good values over the band.

Figure 2.20 shows the phase difference between the two typical transmission S parameters,  $S_{52}$  and  $S_{54}$ . It can be seen that the measured phase difference between these two outputs is close to the quadratic reference of  $90^\circ$ , as expected. The observed phase difference error is less than  $\pm 2^\circ$  up to 64 GHz.

As regards the phase difference between the two typical transmission S parameters,  $S_{61}$  and  $S_{63}$ , depicted in Figure 2.21, shows two quasi-parallel characteristics. The phase difference between two requested ports (port 1, port 3) is closed to  $90^\circ$ . The phase difference error is approximately  $3^\circ$  in the entire frequency band of interest.



**Figure 2.19** - Typical measured outputs matches for the proposed six-port.



**Figure 2.20** - Typical measured transmission phase difference of ( $S_{52}$ ,  $S_{54}$ ) for the proposed six-port.

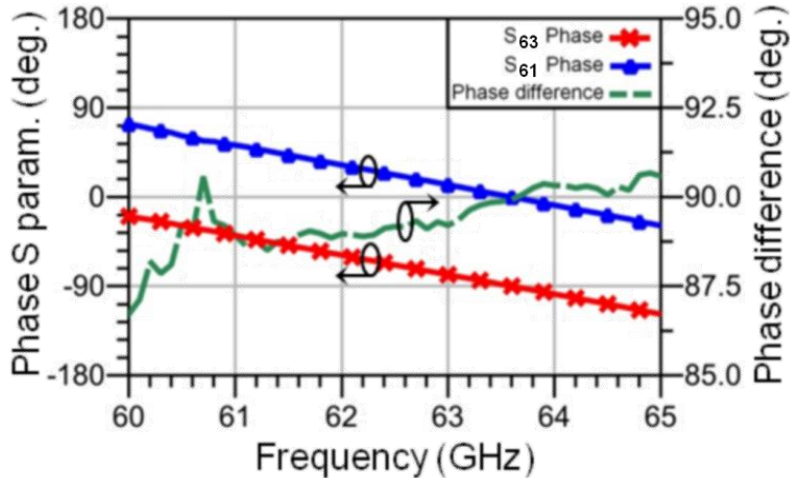


**Figure 2.21** - Typical measured transmission phase difference of ( $S_{61}$ ,  $S_{63}$ ) for the proposed six-port.

## 2.5. Conclusion

Novel V-band MHMICs, including a rounded shape six-port circuit, have been presented in this paper. In order to improve circuits' performances, these MHMICs are fabricated in microstrip technology on very thin ceramic substrate.

Measurement results show that the proposed circuits are wideband components. The measured supplementary insertion losses, amplitude, and phase unbalancements are considered more than acceptable to build modulators/ demodulators for modulation schemes having up to 16 symbols (BPSK to 16 QAM, PSK or dual star). Keeping in the account the 7 GHz bandwidth allowed for V-band communication systems, the data-rates can reach quasi-optical values.

Six-port computer models have been implemented from the previous full port measurements of Wilkinson and couplers. The two-port measurements of each circuit on die have been imported into ADS using data access components (DAC). Each model use multiple DAC, interconnected according to the corresponding schematic of the six-port. The S parameter simulation results, using the six-port model developed from these basic building boxes, agree with the measurements of the five six-port circuits presented in this paper. Therefore, the computer models will be considered for advanced system simulations of high-speed V-band wireless communication systems.

In conclusion, this new fabrication run has allowed us to improve the performances of the six-port circuit in order to be integrated in our future design of an entire millimeter wave front-end on a 2.54 cm x 2.54 cm thin ceramic substrate. The die will integrate a 2 x 8 elements patch antenna array, a MMIC Low Noise Amplifier, and a six-port quadrature down-converter.

## Acknowledgment

The authors would like to acknowledge the support of the “Centre de Recherche en Électronique Radiofréquence” (CREER) of Montréal, funded by the “Fonds du recherché du Québec –Natures and Technologies” (FRQNT), for the MHMICs fabrication.

## References

- [1] Federal Communications Commission, “Amendment of Parts 2, 15 and 97 of the Commission's Rules to Permit Use of Radio Frequencies Above 40 GHz for New Radio Applications”, FCC 95-499, ET Docket No. 94-124, RM-8308, December 1995.
- [2] B. Laemmle, K. Schmalz, J. Borngraeber, J. C. Scheytt, R. Weigel, A. Koelpin, and D. Kissinger, “A fully integrated 120-GHz six-port receiver front-end in a 130-nm SiGe BiCMOS technology”, in IEEE Topical Meeting Silicon Monolithic Integrated Circuits in RF Systems Digest, pp. 129-131, Austin, TX, January 2013.
- [3] P. Smulders, “Exploiting the 60 GHz Band for Local Wireless Multimedia Access: prospects and Future Directions”, IEEE Communications Magazine, no.1, pp. 140-147, January 2002.
- [4] A. Koelpin, G. Vinci, B. Laemmle, D. Kissinger, and R. Weigel, “The six-port in modern society,” IEEE Microwave Magazine, vol. 11, no. 7, pp. 35–43, 2010.
- [5] T. Eireiner, T. Schnurr, and T. Muller, “Integration of a six-port receiver for mm-wave communication,” in Proc. IEEE Mediterranean Electrotechnical Conf., pp. 371–376, 2006.
- [6] B. Laemmle, K. Schmalz, C. Scheytt, D. Kissinger, and R. Weigel, “A 62 GHz reflectometer for biomedical sensor readout in SiGe BiCMOS technology”, in IEEE Topical Meeting Silicon Monolithic Integrated Circuits in RF Systems. Digest., pp. 45-48, Santa Clara, CA, January 2012.
- [7] W. Winkler, “60 GHz Transceiver Circuits in SiGe HBT Technology”, IEEE Compound Semiconductor Integrated Circuit Symposium Digest, pp. 109-112, November 2005.

- [8] K. Leong, and T. Itoh, “Advanced and Intelligent RF Front-End Technology”, Wireless Communication Technology, Conference Proceedings, pp. 190-193, October 2003.
- [9] E. Moldovan, S.O. Tatu, S. Affes, Ke Wu, and R. G. Bosisio, “W-band Substrate Integrated Waveguide Radar Sensor Based on Multi-port Technology”, 4th European Radar Conference, 2007 European Microwave Week, Conference Proceedings, pp. 174-177, Munich, October 8 - 12, 2007.
- [10] D. Hammou, M. Nedil, N. Kandil, E. Moldovan, S.O. Tatu, “V-band Millimeter-wave Microstrip to Rectangular Waveguide Transition”, Microwave and Optical Technology Letters, vol. 55, no.7, pp. 1696–1699, July 2013.
- [11] B. Boukari, D. Hammou, E. Moldovan, R. G. Bosisio, Ke Wu, S.O. Tatu, “MHMICs on Ceramic Substrate for Advanced Millimeter wave Systems”, 2009 IEEE MTT-S International Microwave Symposium, Boston, Conference Proceedings, pp. 1025-1028, MA, June 7-12, 2009.
- [12] M.Nishimoto, M. Hamai, J. Laskar, Lai, R. ; “Onwafer Calibration Techniques and Applications at V-band,” IEEE Microwave and Guided Wave Lett., Vol. 4, Issue 11, pp. 370-372, November 1994.
- [13] S.O. Tatu, B. Boukari, E. Moldovan, R. G. Bosisio, Ke Wu, “Millimeter-wave Multi-port Radar Sensor with Integrated Receiver Front-end for Automotive Applications”, 2012 IEEE MTT-S International Microwave Symposium, Conference CD, pp.1-4, Montreal, Canada, June 17-22, 2012.
- [14] S.O. Tatu, E. Moldovan, S. Affes, “Multi-Port Front-End and Transceivers for V-Band Multi-Gigabit/s Communication Systems”, Digital Front-End in Wireless Communications and Broadcasting Circuits and Signal Processing, ISBN:9781107002135, Chapter DOI: <http://dx.doi.org/10.1017/CBO9780511744839.025>, pp. 707-732, Cambridge University Press, Cambridge, UK, September 2011.
- [15] D. Hammou, E. Moldovan, S.O. Tatu, “Novel MHMIC Millimeter Wave Power Divider/Combiner”, 2011 IEEE Canadian Conference on Electrical and Computer Engineering (CCECE 2011), Conference proceedings, pp. 280-283, Niagara Falls, Ontario, May 8-11, 2011.

- [16] T. Brabetz and V. Fusco, “Six-port receiver front-end MMIC for V-band MBS applications,” in Proc. 11th Gallium Arsenide Applications (GAAS’03), pp. 97–99, October 2003.

## **CHAPITRE 3 :**

### **PERFORMANCE COMPARISON OF 60 GHZ PRINTED PATCH ANTENNAS WITH DIFFERENT GEOMETRICAL SHAPES USING MINIATURE HYBRID MICROWAVE INTEGRATED CIRCUITS TECHNOLOGY**

**C. Hannachi, and S.O. Tatu**

IET Microwaves Antennas & Propagation, vol. 2016, pp.106-112, October 2016

**Résumé :** Dans ce chapitre, une étude comparative de différentes formes d'antennes imprimées a été effectuée. Les formes géométriques considérées sont la forme rectangulaire, carré, triangulaire, trapézoïdale, circulaire, elliptique et annulaire. L'objectif principal de cette comparaison est de déterminer la forme géométrique de l'élément patch, la plus convenable en termes de bande passante, gain, taille, et efficacité. Cependant, le meilleur élément sera intégré dans un réseau d'antenne comprenant au minimum 16 éléments, qui sera à son tour implémenté dans le prototype de la frontale radiofréquence proposée. Il convient également de noter que toutes ces antennes microrubans ont été conçues en technologie MHMIC sur un substrat en céramique ultra mince pour permettre un niveau plus élevé d'intégration avec d'autres circuits intégrés notamment, l'amplificateur faible bruit (LNA), et le circuit six-port tel est le cas dans notre frontale radiofréquence. Cette étude comparative sera aussi de grande utilité particulièrement, pour les concepteurs d'antennes puisque elle leur permet de sélectionner la géométrie d'antenne la plus appropriée lors de la conception des antennes microrubans opérant à la bande de fréquence de 60 GHz.

## **Abstract**

This paper presents a comparative study of several printed antennas having different shapes of the patch (rectangular, square, triangular, trapezoidal, circular, elliptical, and annular ring), suitable for 60-GHz wireless applications. All these microstrip patch antennas have been designed and fabricated on a very thin ceramic substrate to enable a high level of integration with other integrated circuits including passive circuits (such as power dividers, hybrid couplers, and passive filters), and active circuits (such as LNA, RF mixers, and frequency multipliers). In that event, all of those circuits will be incorporated on a single and very small planar substrate to reduce overall size, and to avoid lossy millimeter-wave connectors. In order to analyze and compare the performances, Advanced Design System of Keysight Technologies was used for circuits design and simulation. This comparison is based on the obtained results particularly in radiation characteristics and inputs return loss, by determining the main associated parameters such as the bandwidth, VSWR, gain, directivity, efficiency, and cross polarization level. This comparative study would be very helpful for RF design engineers to select suitable antenna geometry while designing microstrip patch antenna arrays at 60 GHz millimeter-wave band.

### **3.1. Introduction**

Millimeter-wave microstrip patch antennas are a promising alternative to the future wireless technologies in various sectors including, military, civil and commercial [1, 2]. This is mainly due to their low-cost, small size and lightweight, as well as easy fabrication and integration with any planar fabrication technology, including Miniature Hybrid Microwave Integrated Circuit (MHMIC) and Monolithic Microwave Integrated Circuit (MMIC) [3-6].

Recently, researchers' attention has been focused on 60 GHz band with over a 7 GHz of continuous unlicensed spectrum; this makes the band very desirable for high data rate wireless applications. Moreover, the short wavelength at 60 GHz enables the design of very compact elements with very small form factors that could never be achieved in the past on a chip at low frequencies. Despite these advantages, many factors restrict the use of 60 GHz band for long distance communication (>2 km) such as, in particular, the oxygen absorption (10-17 dB/km) and the severe path loss, which is close to 88 dB for 10 m range. However, these adverse effects can be circumvented by designing high gain, and high directive microstrip patch antennas. For this purpose, several techniques have been suggested in recent years, for instance, reducing the

substrate permittivity ( $\epsilon_r$ ) or increasing its thickness (h), introducing parasitic elements, and using modified shape of the patch [6-8]. Generally, a suitable compromise is desirable between all these techniques, for example if the substrate thickness (h) is increased beyond  $0.1\lambda_0$  (0.5 mm); surface-wave propagation takes effect, and the probe inductance increases. On the other hand, the use of parasitic element increases the overall size of antenna and hence limits their use as array elements. Other possible approaches are also proposed, among the most relevant, is to integrate the appropriate single microstrip patch antenna shape into the array structures (2x2, 4x4, and 8x8) to attain a high directional radiation pattern, and high gain (up to 22 dB). On the one hand, this allows overcoming the gain limitation of the single microstrip patch antenna at 60 GHz millimeter-wave band, which cannot enable high-data rate wireless applications, and on the other hand, they generate highly directional radiation patterns and narrow beam widths, which are very desirable for multiple 60 GHz wireless applications. These applications usually cover a distance between 2 m and 2 Km, and require high gain (10 to 20 dB) as well as moderate bandwidth (10 to 700 MHz), including particularly, line of sight point-to-point links (LOS), Giga-bit/s Wireless LAN, broadband fixed wireless access (BFWA), mobile systems communications, short-range personal communications, and short-range home communications [9].

In this paper, performance comparison for seven geometric shapes of microstrip patch antennas designed to operate at 60 GHz band have been carried out in order to investigate the effect of geometric shape on microstrip patch antennas performances. This comparison deals with almost all of regular geometric shapes of the microstrip patch at 60 GHz band, including rectangular, square, triangular, trapezoidal, circular, elliptical, and annular ring. It provides a more complete view compared to other works in the literature that most of them are focused only on the more common microstrip antenna shapes such as the rectangular and circular shapes [10-12]. One of the important considerations in designing the proposed microstrip patch antennas is the compact size. The latter is the key element to enable a fully integrated 60 GHz transceiver front-end on a miniature single-chip. For this purpose, a low-loss substrate with a small thickness and high dielectric constant, compatible with integrated circuit fabrication techniques is highly required. However, the selected thin film ceramic substrate ( $h=127 \mu\text{m}$ ,  $\epsilon_r=9.9$ ) meets perfectly these requirements, it provides exceptional performances at millimeter wave

frequencies up to 90 GHz [13]. In addition, the microstrip lines widths are comparable to the substrate thickness, which facilitates the design and optimization of the circuits.

### **3.2. Conventional designs and specifications**

Generally, microstrip patch antennas are made of conducting material such as copper, silver or gold, as was in our case. It is typically composed of a radiating patch on one side of a dielectric substrate and a ground plane on the other side. The most popular geometries have been explored in the literature including, the rectangular, triangular, circular and annular ring shapes.

Table 3.1 below shows all these shapes with their characteristic geometric parameters.

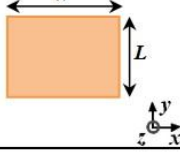
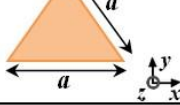
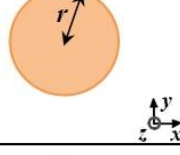
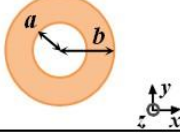
As illustrated, for rectangular microstrip patch,  $W$  and  $L$  are computed for the specific substrate at the resonance frequency  $f_r$  [6]. The calculation of length and width is based on the transmission line method as explained below in (1) and (2), using the effective dielectric constant  $\epsilon_{eff}$  and the extension length  $\Delta L$  in (3) and (4) [11].

The second geometry represents the triangular shaped patch antenna, which has also received a lot of attention recently [14, 15]. This is due to their small size compared with other shapes such as the rectangular and circular patch antennas. Regarding the equilateral triangular patch antenna, at the lowest order resonant frequency  $f_r$ , the side length  $a$ , can given by (5) [16, 17].

For a circular microstrip patch antenna design, a method analysis based on the cavity model was adopted, by modelling the circular patch, the ground plane and the material between them as a circular cavity. However, a correction is introduced by using an effective radius  $r_{eff}$  instead of the actual radius  $r$ , as expressed in (7) and (9) [18-19]. The resonant frequency  $(f_r)_{110}$  for the dominant mode  $TM_{110}^z$  is given by (8), where  $z$  is taken perpendicular to the patch and the substrate height is assumed to be very small ( $h \ll \lambda$ ).

The last geometry is the annular ring shaped microstrip antenna. It consists of an inner and outer radii, designated by  $a$  and  $b$ , respectively. However, by means of these two parameters, the separation of resonant modes can be easily controlled. In fact, several analyses confirmed that the  $TM_{21}$  mode is undoubtedly the best mode because of its good radiation efficiency and its high performances in circular polarization. Nevertheless, when the annular ring patch works at this mode, its mean circumferential length is approximately twice the wavelength in effective permittivity as expressed in (11). Therefore, the operating frequency can be given by (12) [20].

**Tableau 3.1** - Theoretical design parameters for conventional geometries of microstrip patch antennas.

geometric shapes	characteristic equations	
Rectangular 	$W = \frac{c}{2f_r} \sqrt{\frac{2}{\epsilon_r + 1}} \quad (1)$	$L = \frac{c}{2f_r \sqrt{\epsilon_{eff}}} - 2\Delta L \quad (2)$
	$\epsilon_{eff} = \frac{\epsilon_r + 1}{2} + \frac{\epsilon_r - 1}{2} \left[ 1 + 12 \frac{h}{W} \right]^{-1/2} \quad (3)$	$\Delta L = 0.412h \frac{\left( \epsilon_{eff} + 0.3 \right) \left( \frac{W}{h} + 0.264 \right)}{\left( \epsilon_{eff} - 0.258 \right) \left( \frac{W}{h} + 0.8 \right)} \quad (4)$
Triangular 	$a = \frac{2c}{3f_r \sqrt{\epsilon_r}} \quad (5)$	$c = 3 \times 10^8 \quad (6)$
Circular 	$r_{eff} = r \left\{ 1 + \frac{2h}{\pi r \epsilon_r} \left[ \ln \left( \frac{\pi r}{2h} \right) + 1.7726 \right] \right\}^{1/2} \quad (7)$	$(f_r)_{110} = \frac{1.8412 c}{2\pi r_{eff} \sqrt{\epsilon_r}} \quad (8)$
	$r = \frac{F}{\left\{ 1 + \frac{2h}{\pi \epsilon_r F} \left[ \ln \left( \frac{\pi F}{2h} \right) + 1.7726 \right] \right\}^{1/2}} \quad (9)$	$F = \frac{8.791 \times 10^9}{f_r \sqrt{\epsilon_r}} \quad (10)$
Annular ring 	$\pi(a+b) = \frac{2\lambda_0}{\sqrt{\epsilon_{eff}}} = \frac{2c}{f_{21} \sqrt{\epsilon_{eff}}} \quad (11)$	$f_{21} = \frac{2c}{\pi(a+b) \sqrt{\epsilon_{eff}}} \quad (12)$

### 3.3. Antennas design and fabrication

The proposed microstrip patches antennas can take a variety of geometrical forms, such as rectangular, square, triangular, trapezoidal, circular, elliptical, and annular ring as shown in Fig.1a. All these microstrip patch antennas are etched on a very thin alumina substrate ( $\epsilon_r = 9.9$  and  $h = 127 \mu m$ ), using the MHMIC technology. It should be noted that this technology is considered as an intermediate between Microwave Integrated Circuits (MIC) and Monolithic Microwave Integrated Circuits (MMIC). It adopts a thin-film process in which a wide range of passive components are fabricated on an alumina substrate having typically a high dielectric constant. These components are not limited only to basic lumped passive components such as thin film resistors, overlay capacitors, and spiral inductors, but also a large variety of RF passive components including directional couplers, power dividers, microstrip patch antennas, and filters. The active devices such as diodes, amplifiers, and LNAs are added at the end of the process by assembly, using gold wire bonding technology.

The most commonly used materials for the substrate metallization are the gold, copper, or copper-gold as shown in Fig.1b. The thin film resistors are usually done by depositing nichrome or tantalum nitride films on alumina substrates. For this purpose, various processing techniques are often used, including e-beam, photolithography techniques, and more recently, the excimer laser micro-machining [21-22].

Today, the MHMIC technology represents an excellent alternative for low-cost and rapid prototyping of highly miniaturized circuits with improved performances at millimeter-wave frequencies up to 90 GHz [13].

In order to ensure return loss measurement accuracy, the TRL calibration technique was adopted using on-wafer microstrip structures and the TRL algorithm supported by our vector network analyzer E8362B from Agilent Technologies. A dual port calibration is used with the same already tested standards as for two-port circuit measurements [23]. Its standards consist of a thru line (T), two open circuits as reflect (R) and a short line (L). Due to the fragility of the very thin gold layer metallization ( $1 \mu\text{m}$ ), multiple identical standards are designed on the same substrate to ensure repeatability and success of calibrations and measurements.

To perform on-wafer measurements with ground-signal-ground GSG  $150 \mu\text{m}$  coplanar probes, a coplanar line to microstrip transition has been designed. Quarter-wavelength open stubs are used to implement RF short-circuits, as shown in Fig. 1c. In this approach, the metalized via-holes for RF are avoided because those are difficult to be fabricated with high accuracy and repeatability at millimeter-wave frequencies [23].

As regards the feeding technique for the proposed microstrip patches antennas, we chose the simplest way (direct feed) that consists of a microstrip line directly connected to the end of the patch. The impedance matching can be obtained without the need for any additional matching element, by simply selecting the proper inset cut length (see Figure 3.1c). The major advantage of this technique is its simplicity in terms of fabrication and analysis, as well as impedance matching.

It should also be noted that the radiation patterns were only simulated, while introducing the estimated conductor and dielectric losses using momentum platform in Advanced Design System (ADS) to achieve very accurate electromagnetic simulations. This is because a high complexity of 1.85 mm V-connector installation, which is the only one available in the millimeter-wave

connector market that can be, used up to 67 GHz. However, its connection with MHMIC circuit is very challenging due to the fragility of the ceramic alumina substrate ( $h=127 \mu\text{m}$ , very thin gold layer metallization ( $1 \mu\text{m}$ )), and also the need for the manufacture of a metallic base to fix the ceramic substrate and 1.85 mm V-connector together, which further complicates the fabrication process. In addition, the large size of the 1.85 mm V-connector compared to the fabricated antenna sizes is yet another serious problem (1.85 mm V-connector width is approximately 10 times greater than the microstrip patch antenna width), this can affect significantly the return loss, radiation pattern, and introduce additional resonances. Finally, the 1.85 mm V-connector could reach the insertion loss of 1 dB below 67 GHz, which is a considerable loss, greatly influencing the gain of the fabricated patch antennas [24-25].

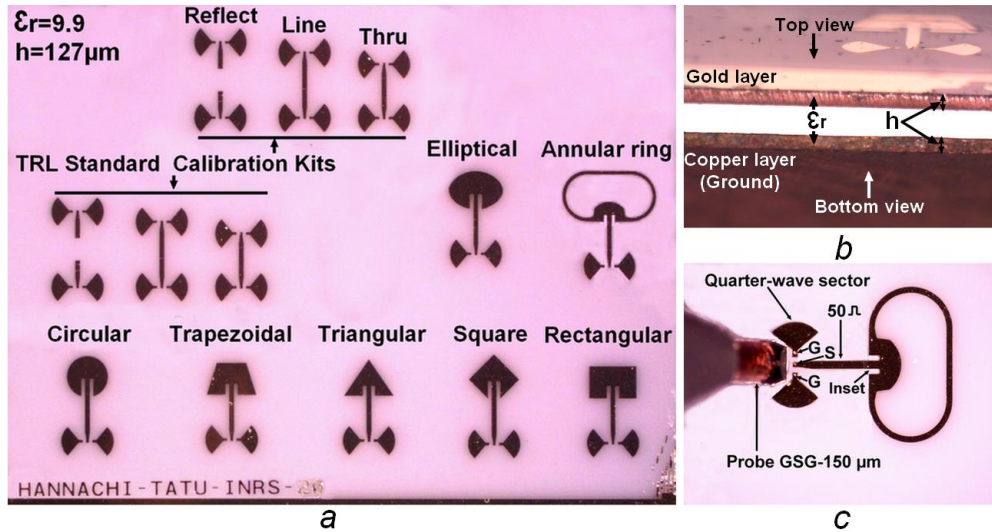


**Figure 3.1** - Micro-photographs of (a) The fabricated microstrip patch antennas on very thin ceramic substrate, (b) Cross-section view of thin ceramic substrate and metal layers, and (c) On-wafer measurement with GSG-150  $\mu\text{m}$  probe.

### 3.4. Rectangular and Square Microstrip Patch Antennas Shapes

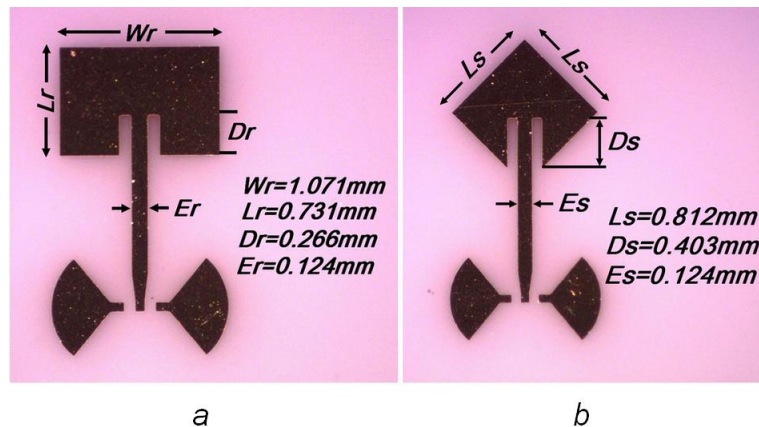
The design and geometrical parameters of rectangular and square microstrip patches are shown in Figures 3.2a and 3.2b. As we know, the square shape is a special case of the rectangular shape when the four sides are equal, for this reason, we will discuss the two cases together.

Figure 3.3a shows the simulated and measured return loss of rectangular and square microstrip patches. It is noteworthy that the return loss has been measured from 60 GHz, while

the allowed frequency band for unlicensed applications starts from 57 GHz. This is due to measurement set-up capabilities (WR-12 rectangular waveguides modules for the 60–90 GHz millimeter-wave extension of the VNA). However, the results can be extrapolated in the 57–60 GHz band by symmetry and comparison with simulations.

Considering the -10 dB bandwidth, corresponding to a Voltage Standing Wave Ratio (VSWR) bandwidth under 1.92, the rectangular patch has largest impedance bandwidth approximately 1.7% from 61–62.2 GHz, compared to the square patch that has 1.53% from 61.4–62.4 GHz. This is also confirmed by the measured VSWR in Figure 3.3b, which varies between almost 1 and 1.92 in the same frequency ranges for both microstrip patch antennas.

The simulated radiation patterns at 61.8 GHz are illustrated in Figures 3.4a and 3.4b for rectangular and square microstrip patches. The maximum gain and directivity at 61.8 GHz are respectively 5.22 dBi and 6.50 dBi for the rectangular patch, while for the square patch are 4.45 dBi and 6.14 dBi.



**Figure 3.2** - Microphotograph with geometric dimensions of (a) Rectangular patch antenna, and (b) Square patch antenna.

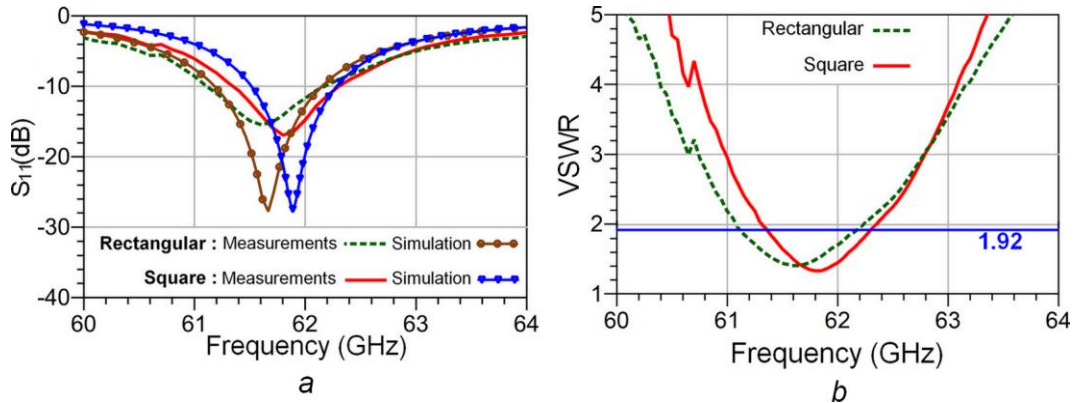


**Figure 3.3** - Measured and simulated return loss and input VSWR : (a) Measured and simulated return loss of rectangular and square patch antennas, and (b) Measured VSWR of rectangular and square patch antennas.

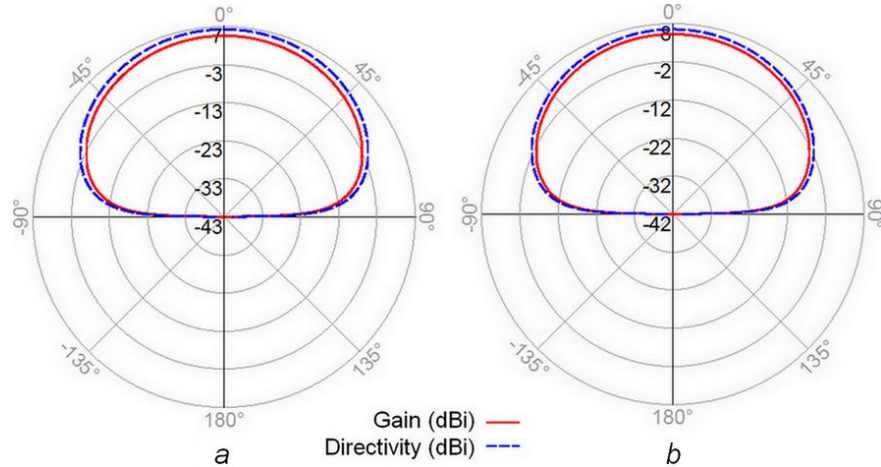


**Figure 3.4** - Simulated radiation characteristics at 61.8 GHz of (a) Square patch antenna and (b) Rectangular patch antenna.

### 3.5. Triangular and Trapezoidal Microstrip Patch Antennas Shapes

Figure 3.5a and 3.5b show, respectively, the geometry of the triangular and trapezoidal patches. It may be noted that the triangular shape can be obtained from trapezoidal one, when the smaller base at the top tends towards zero. This brings us to study these two shapes together.

The results of return losses and VSWR are compared over the considered frequency band with good agreement in Figure 3.6a and 3.6b respectively. These results show that the triangular

patch at -10 dB (VSWR  $\approx$  1.92) has bandwidth of 0.65 GHz from 61.4 to 62.05 GHz, which represents the measured 1.92:1 VSWR bandwidth of 0.97% at the resonant frequency (61.7 GHz). For the trapezoidal patch, the measured bandwidth is 1.62% from 61 to 62 GHz (1.92:1 VSWR bandwidth), which is significantly larger than the bandwidth previously obtained by the triangular patch.

The simulated radiation characteristics for triangular and trapezoidal patches are presented in Figures 3.7a and 3.7b respectively. The maximum gain and directivity achieved at 61.7 GHz are successively 4.10 dBi and 5.96 dBi for the triangular patch, whereas for the trapezoidal patch are 4.30 dBi and 6.14 dBi.

Measured bandwidth is 1.62% from 61 to 62 GHz (1.92:1 VSWR bandwidth), which is significantly larger than the bandwidth previously obtained by the triangular patch.

The simulated radiation characteristics for triangular and trapezoidal patches are presented in Figure 3.7a and 3.7b respectively. The maximum gain and directivity achieved at 61.7 GHz are successively 4.10 dBi and 5.96 dBi for the triangular patch, whereas for the trapezoidal patch are 4.30 dBi and 6.14 dBi.

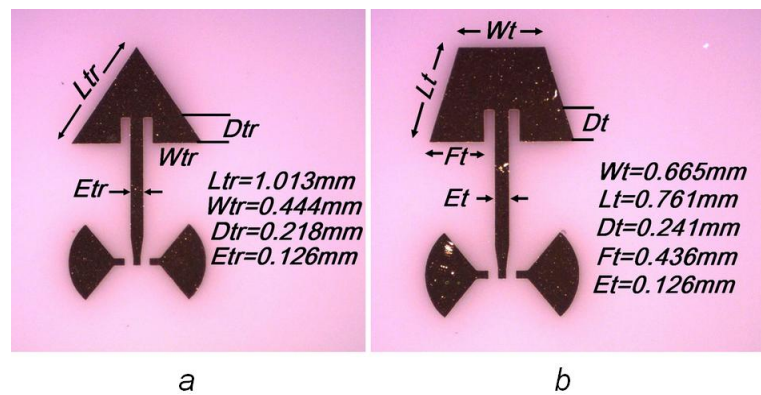


**Figure 3.5** - Micro-photograph with geometric dimensions of (a) Triangular patch antenna and (b) Trapezoidal patch antenna.

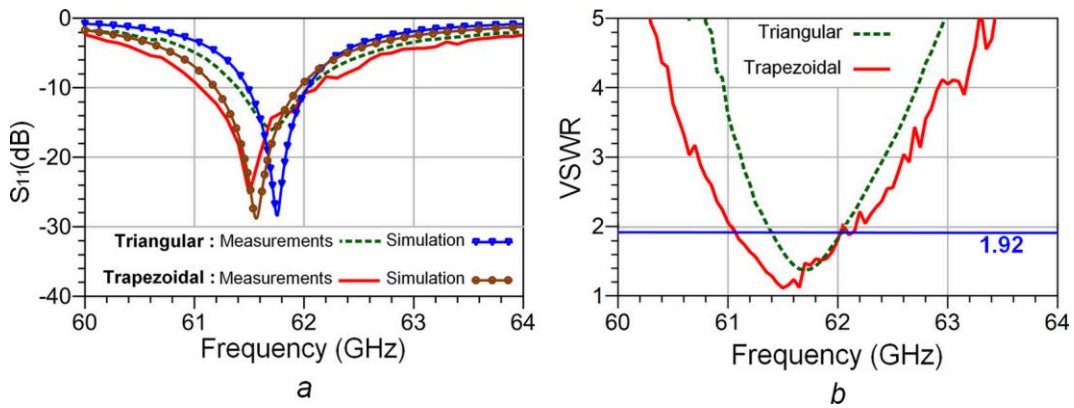


**Figure 3.6** - Measured and simulated return loss, and input VSWR : (a) Measured and simulated return loss of triangular and trapezoidal patch antennas, (b) Measured VSWR of triangular and trapezoidal patch antennas.

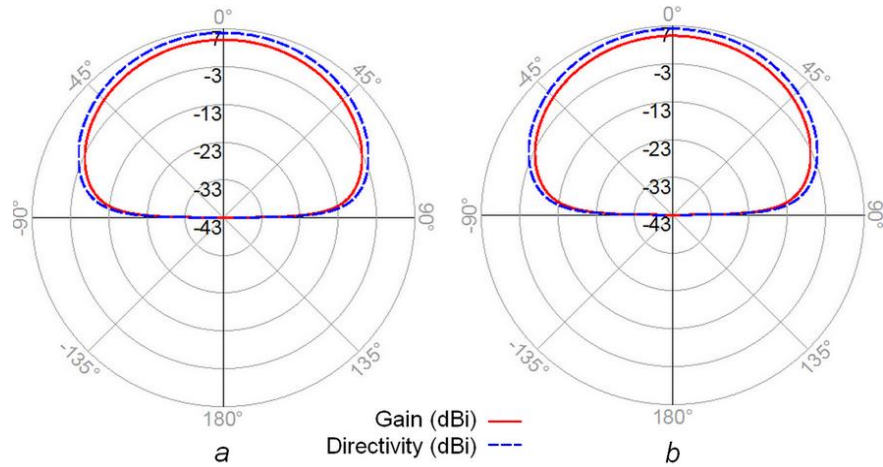


**Figure 3.7** - Simulated radiation characteristics at 61.7 GHz of (a) Triangular patch antenna and, (b) Trapezoidal patch antenna

### 3.6. Circular and Elliptical Microstrip Patch Antennas Shapes

Figures 3.8a and 3.8b show the geometry of the proposed circular and elliptical microstrip patch antennas with detailed dimensions. As can be seen, the circular shape can be obtained from the elliptical shape when the smaller radius  $R_2$  and the largest radius  $R_1$  are equal. For that reason, we have analyzed the two microstrip patches together.

The simulated and measured results of return loss, as well as the measured VSWR are shown in Figures 3.9a and 3.9b over the same frequency range, 60 to 64 GHz, taking into account the

unlicensed V-band and our measurement capabilities. In terms of return losses, good agreement between simulated and measured results is obtained for both circular and elliptical microstrip patches. However, we can observe a resonant frequency shift of 1.5% between simulated and measured return loss for each microstrip patch antenna. This frequency shift is also clearly observed in the measured VSWR in Figure 3.9b. Generally, such shift in the frequency can be caused by the fabrication tolerances, higher dielectric constant substrate and the reflections due to the time effect to remove GSG 150  $\mu\text{m}$  coplanar probes. The measured impedance bandwidths (1.92:1 VSWR bandwidths) are 1.65% (60.1–61.1 GHz) and 1.79 % (60.9–62 GHz), respectively, for the circular and elliptical microstrip patches. It is very clear from these two figures that the elliptical microstrip patch offers higher bandwidth compared to the circular microstrip patch.

The simulated radiation characteristics of both circular and elliptical microstrip patches at 61 GHz are shown in Figures 3.10a and 3.10b. As these figures show, the maximum gain and directivity for both are respectively 4.60 dBi and 6.22 dBi for the circular patch, while for the elliptical patch are 4.44 dBi and 6.18 dBi.

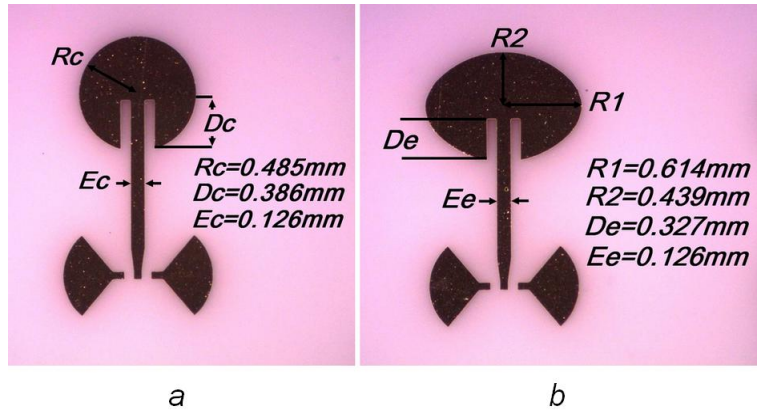


**Figure 3.8** - Microphotograph with geometric dimensions of, (a) Circular patch antenna and, (b) Elliptical patch antenna.

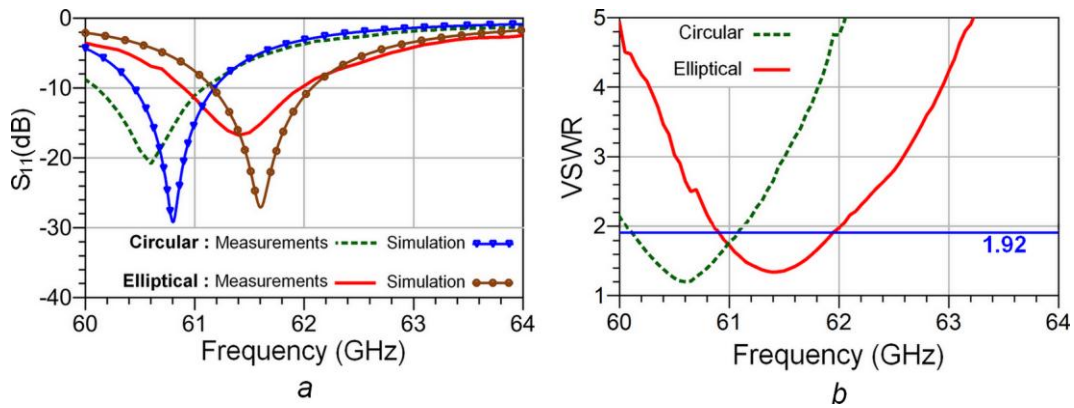


**Figure 3.9** - Measured and simulated return loss and input VSWR : (a) Measured and simulated return loss of circular and elliptical patch antennas, and (b) Measured VSWR of circular and elliptical patch antennas

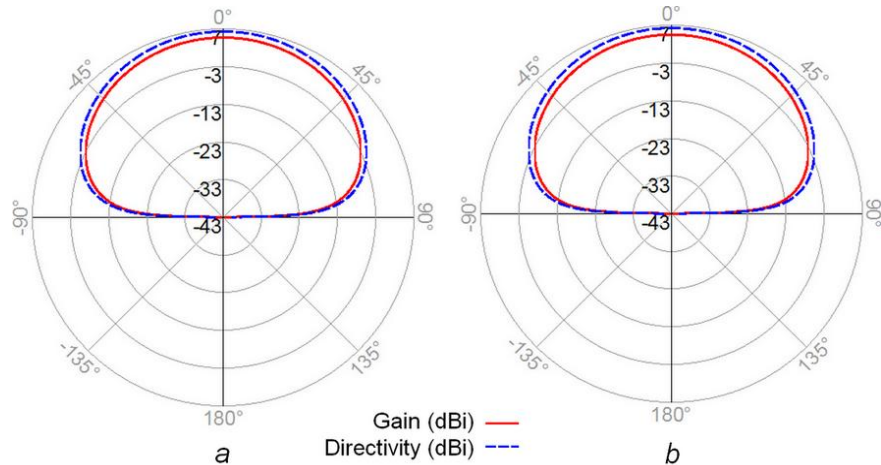


**Figure 3.10** - Simulated radiation characteristics at 61 GHz of (a) Circular patch antenna and, (b) Elliptical patch antenna.

### 3.7. Annular-ring Microstrip Patch Antenna Shape

A modified geometry of annular ring microstrip antenna with inset feed technique is presented in Figure 3.11a. This structure has been optimized to achieve best radiation efficiency and good impedance matching.

Figures 3.11b and 3.11c show the measured and simulated return loss and the measured VSWR respectively over the considered frequency band, from 60 to 64 GHz. Both results are in

a good agreement and demonstrate that the antenna resonates efficiently at 62 GHz. However, the measured and simulated return loss show a slight downward shift in the resonant frequency, which is mainly due to the substrate losses, imperfections in measurement, and other effects have been mentioned in the previous section. The measured bandwidth of the proposed annular ring microstrip antenna at -10 dB ( $VSWR \approx 1.92$ ) is approximately 0.3 GHz (1.92:1 VSWR bandwidth), ranging from 61.8 GHz to 62.1 GHz. Although these results indicate that antenna bandwidth is narrow, but it is enough for certain millimeter-wave wireless applications such as short-range line of sight communication over link lengths from 10 m to 2 km.

The simulated radiation characteristics in the elevation plane, is shown in Figure 3.12a. It can be observed from this figure that the maximum gain and directivity are respectively 6.03 dBi and 7.09 dBi. A 3-D polar plot is also shown in Figure 3.12b, where the main color is red that shows the maximum field intensity in the broadside direction.

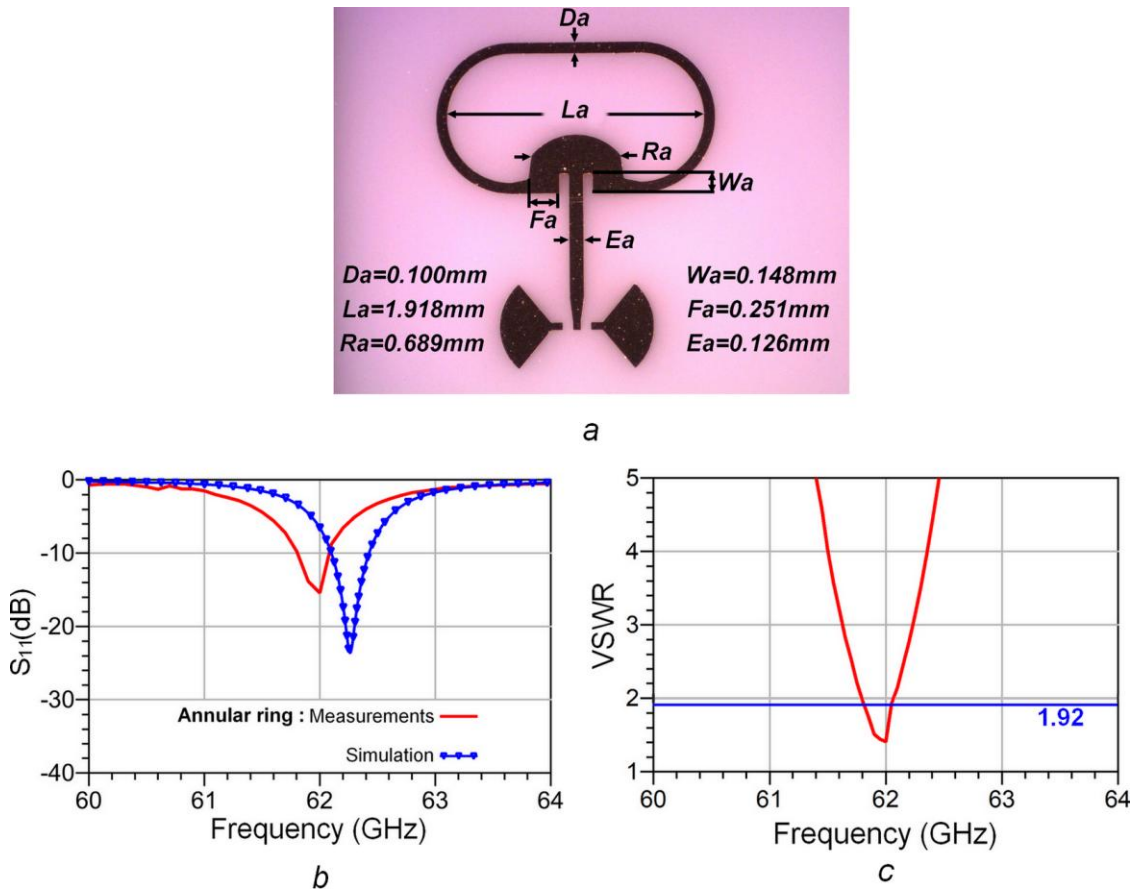


**Figure 3.11** - Design of the proposed annular ring patch antenna : (a) Microphotograph with geometric dimensions, (b) Measured and simulated return loss, and (c) Measured input VSWR.

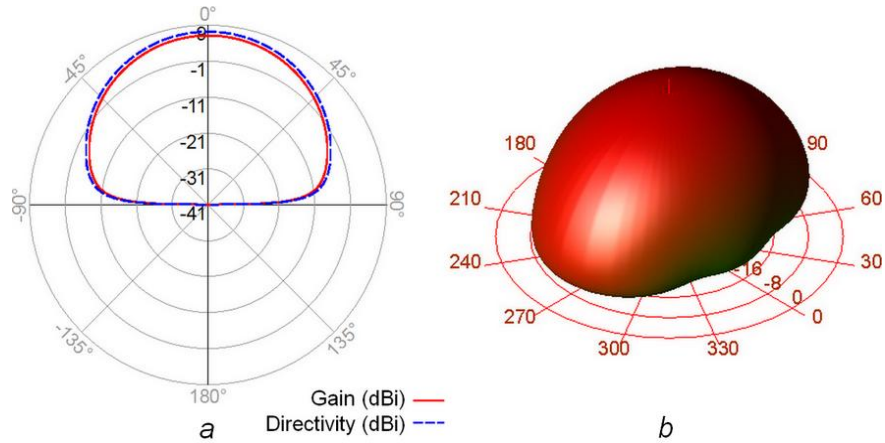


**Figure 3.12** - Simulated radiation characteristics of annular ring patch antenna at 62 GHz : (a) in the elevation plane (b) in the 3D polar plots.

### 3.8. Performance Summary and Comparison

A comparison of various performance parameters, including return loss, VSWR, gain, directivity efficiency, and cross polarization level for different patch antenna geometries is shown in Table 3.2.

It is clear from the table that the rectangular and the elliptical patch antenna achieve better performances in term of bandwidth (BW), with very close values of 1.70% and 1.79% respectively, followed closely by the circular (1.65%), trapezoidal (1.62%) and square patch antenna (1.53%). However, the annular ring patch antenna has lowest impedance bandwidth of 0.65%, followed by the triangular patch antenna (0.97%). It should be noted that the considered bandwidth corresponds to the frequency range over which VSWR is less than 1.92. This means a return loss of 10 dB or about 11% reflected power.

As regards the radiation characteristics, the annular ring patch antenna offers a higher gain and directivity with best efficiency factor, as seen in the same table. This is mainly due to the very high quality factor and its reduced metalized surface compared to other types of geometries. In second position comes the rectangular patch antenna that achieves 74.61% of radiation efficiency, immediately followed by circular patch antenna with 68.86%. All the other shapes have almost same radiation pattern performances with a slight preference for the square patch antenna.

In terms of cross polarization level (XPL), the proposed microstrip patch antennas exhibit very low cross polarization levels, better than -40 dB at broadside for all microstrip patch antenna shapes, except for the annular ring shaped microstrip antenna, which is better than -38 dB. In overall terms, these results are excellent for all proposed microstrip patch antennas and meet perfectly the cross polarization requirements at 60 GHz millimeter-waves band. They are also very important, especially for microstrip antenna arrays, because a poor cross polarization level (XPL) degrades significantly the performance of communication systems, predominantly by a gain reduction and a very bad establishment of the polarization state.

This comparison clearly proves that the rectangular patch presents the best possible compromise in terms of performance, which has at the same time larger bandwidth, high gain, high directivity, better radiation efficiency, and low cross polarization level. However, its large dimensions compared to other geometries at the same operating frequency constitute its major weak point.

**Tableau 3.2 :** Comparison Table of the performances between 7 shapes of fabricated microstrip patch antennas.

PATCH ANTENNA PARAMETERS								
PATCH SHAPES	Resonant Frequency (GHz)	S <sub>11</sub> (dB)	VSWR	BW (%)	Gain (dBi)	Directivity (dBi)	Efficiency (%)	Cross Pol. Level (dB)
<b>Square</b>	61.8	-17	1.32	1.53	4.45	6.14	67.69	-41.3
<b>Rectangular</b>	61.6	-15	1.43	1.7	5.22	6.50	74.61	-41.3
<b>Triangular</b>	61.7	-16	1.37	0.97	4.10	5.96	65.02	-42
<b>Trapezoidal</b>	61.5	-25	1.11	1.62	4.30	6.14	65.43	-41.7
<b>Circular</b>	60.6	-20	1.22	1.65	4.60	6.22	68.86	-40.6
<b>Elliptical</b>	61.4	-17	1.32	1.79	4.44	6.18	66.91	-41.5
<b>Annular ring</b>	62.0	-15	1.43	0.65	6.03	7.09	78.36	-38.5

### 3.9. Conclusion

In this paper, seven different geometric shapes of microstrip patch antennas suited for use at 60 GHz millimeter-wave band were fabricated, characterized and investigated. To understand the impact of geometric shapes on the antenna performances, a comprehensive comparative study between the various fabricated patch antennas has been done.

From this analysis, it can be concluded that the geometrical shape of the patch has a significant impact on the bandwidth with variation of 0.8 GHz between a larger (elliptical) and a narrower (annular ring) bandwidth. Moreover, the radiation characteristics were also affected by the patch geometry; there was 1.1 dBi of variation between maximum and minimum gain reached respectively by the annular ring and triangular patch. Similarly, for the radiation efficiency that has a difference of more than 12% between the maximum (annular ring) and minimum efficiency (triangular patch). As regards the cross polarization level, the obtained results show that the microstrip antenna shapes does not have a potential impact on cross polarization level, except for the case of annular ring microstrip antenna that indicates -38.5 dB (3.5 dB more than the lowest value of -42 dB (triangular patch)). However, a tradeoff which satisfied both, antenna geometry and antenna performances must be achieved.

In this context, the rectangular patch is by far the best appropriated and the most commonly used configuration at lower or millimeter-waves frequencies. It is very easy to analyze using both the transmission-line and cavity models, which are most accurate especially, for thin substrates such as the case of our study.

## Acknowledgments

The authors would like to acknowledge the Natural Sciences and Engineering Research Council of Canada (NSERC), for the generous research support, and the “Centre de Recherche en Électronique Radiofréquence” (CREER) of Montréal, funded by the “Fonds de recherche du Québec–Natures and technologies” (FRQNT), for the MHMICs fabrication.

## References

- [1] Pozar, D.M.: ‘Considerations for millimeter wave printed antennas’, IEEE Trans. Antennas Propag., 1983, 31, (5), pp. 740- 747
- [2] Lee, K., Tong, K.: ‘Microstrip patch antennas – basic characteristics and some recent advances’. Proc. of the IEEE, 2012, 100, (7), pp. 2169–2180
- [3] Kim, D.Y., Mun, J.K., and Kim, C.S.: ‘Design of antenna with broadband and high gain at millimeter wave band’, Electron. Lett., 2012, 48, (22), pp. 1382–1383

- [4] Rajab, K.Z., Mittra, R., and Lanagan, M.T.: ‘Size reduction of microstrip patch antennas with left-handed transmission line loading’, IET Microw. Antennas Propag., 2007, 1, (1), pp. 39–44
- [5] Lee, K.F., Luk, K.M.: ‘Microstrip patch antennas’ (Imperial College Press, London, UK, 2011)
- [6] G. Kumar and K.P. Ray.: ‘Broadband Microstrip Antennas’ (Artech House, Boston, USA, 2003)
- [7] Dejean, Li, R., Tentzeris, G., and Laskar, J.: ‘Development and analysis of a folded shorted-patch antenna with reduced size’, IEEE Trans. Antennas Propag., 2004, 52, (2), pp. 555–562
- [8] Hannachi, C., Tatu, S.O.: ‘A New Compact V-band Six-port Down-Converter Receiver for High Data Rate Wireless Applications’. IEEE Topical Conference on Wireless Sensors and Sensor Networks (WiSNet), San Diego, CA, January 2015, pp. 26–28
- [9] Ofcom Contract 410000258., ‘Radio Systems at 60GHz and Above’ (Rutherford Appleton Laboratory, 2006), pp. 1-194
- [10] Agarwal, S., Pathak, N. P., Singh, D.: ‘Performance comparison of microstrip patch antenna for 94 GHz imaging applications’. 7th IEEE International Conference on Industrial and Information Systems (ICIIS), Chennai, India, Aug. 2012, pp.1-4
- [11] Yahya, S., Olaimat, M.M., Abdel-Razeq, S.N.: ‘Comparison between rectangular and triangular patch antenna arrays’, Appl. Phys. Res., 2012, 4, p. 1-5
- [12] Mathur, V., Gupta, M.: ‘Comparison of performance characteristics of rectangular, square and hexagonal microstrip patch antennas’. 3rd International Conference on Reliability, Infocom Technologies and Optimization (ICRITO), Noida, India, October 2014, pp. 8-10
- [13] Moldovan, E., Tatu, S.O.: ‘Design and Characterization of Novel W-band Wide-band Couplers and Six-port Circuit’. European Microwave Week, Conference proceedings, Paris, France, September 2015, pp. 279-282
- [14] Garg, R., Long, S.A.: ‘An improved formula for the resonant frequency of triangular microstrip patch antennas’, IEEE Trans. Antennas Propag., 1988, 36, (4), pp. 570

- [15] Biswas, M., Dam, M.: ‘Fast and accurate model of equilateral triangular patch antennas with and without suspended substrates’, *Microw. Opt. Technol. Lett.*, 2012, 54, (11), pp. 2663–2668
- [16] Lu, J.H., Tang, C.L., and Wong, K.L.: ‘Circular polarisation design of a single-feed equilateral-triangular microstrip antenna’, *Electron. Lett.*, 1998, 34, (4), pp. 319–321
- [17] Prasanna, Zade, L., Choudhary, Dr. N. K.:‘Design and Implementation of a Broadband Equilateral Triangular Parasitic Patch Microstrip Antenna Array for Wireless Applications’, *International Journal of Computer Applications*, 2011, 28, (7), pp. 36-40
- [18] Verma, A. K., Nasimuddin. : ‘Analysis of circular microstrip patch antenna as an equivalent rectangular microstrip antenna on iso/anisotropic thick substrate’, *IEE Proc. Microwave Antennas and Propagation*, 2003, 150, (4), pp. 223-229
- [19] Huang, C.Y., Hisa, W.C.: ‘Planar Elliptical Antenna for Ultra - Wide Band Communication’, *Electron Lett.*, 2005, 41, (6), pp. 296-297
- [20] Batchelor, J. C., and Langley, R. J.: ‘Microstrip ring antennas operating at higher order modes for mobile communications’, *IEE Proc. Microwave Antennas and Propagation*, 1995, 142, (2), pp. 151-155
- [21] Syed, N. A., S. Anantha Ramakrishna., and J. Ramkumar.: ‘Excimer Laser Micromachining for Miniaturized Hybrid Microwave Integrated Circuits’ (*Directions*, 2015, Vol. 15 No.1)
- [22] ‘NANOWAVE Technologies Inc’, [http://www.nanowavetech.com/\\_pdf/Thin-Film\\_Catalog\\_May2015\\_v5.pdf](http://www.nanowavetech.com/_pdf/Thin-Film_Catalog_May2015_v5.pdf), accessed 14 May 2016
- [23] Hannachi, C., Hammou, D., Djerafi, T., Ouardirhi, Z., and Tatu, S.O.: ‘Complete Characterization of Novel MHMICs for V-band Communication Systems’, *Journal of Electrical and Computer Eng.*, 2013, Article ID 686708, pp. 1-9
- [24] Ranvier, S., Kyro, M., Icheln, C., Luxey, C., Staraj, R., and Vainikainen, P.: ‘Compact 3-D On-Wafer Radiation Pattern Measurement System for 60 GHz Antennas’, *Microw. Opt. Technol. Lett.*, 2009, 51, (2), pp. 319-324

- [25] Hrobak, M.: ‘Critical mm-Wave Components for Synthetic Automatic Test Systems’  
(Springer Vieweg, Berlin, Germany, 2015)

## **CHAPITRE 4 :**

### **A COMPACT V-BAND PLANAR GAP-COUPLED 4X1 ANTENNA ARRAY: IMPROVED DESIGN AND ANALYSIS**

**C. Hannachi, and S.O. Tatu**

Acess IEEE, vol. 2017, pp.1-7, March 2017

**Résumé :** Ce chapitre présente une nouvelle structure de réseau d'antenne microrubans à 4 éléments en utilisant la technique de couplage par proximité en ondes millimétriques, particulièrement dans la bande de 57 à 65 GHz. Afin de répondre à la problématique de réduction de la taille liée à ce genre de technique et de faciliter l'intégration du réseau conçu avec d'autres composants passifs ou actifs, le réseau d'antennes proposé a été conçu en adoptant un procédé de fabrication MHMIC (Miniature Hybrid Microwave Integrated Circuits) sur un substrat en céramique ultra mince, ayant une permittivité relative de  $\epsilon_r = 9,9$  et une épaisseur de  $h = 127 \mu\text{m}$ . La structure proposée est basée sur une forme améliorée d'un élément patch ayant des bords rayonnants incurvés. Pour une analyse plus approfondie, les performances de ce dernier en terme de largeur de bande, ont été évaluée et comparées avec la structure classique d'une antenne patch rectangulaire élémentaire, adoptant la même technique de couplage par proximité.

Le réseau d'antenne microrubans à 4 éléments proposé montrent des performances améliorées, au niveau de la largeur de bande (7%), et un gain d'environ 10,7 dB tout en maintenant une taille réduite (5,2 mm x 9,5 mm). Ces excellentes performances font de lui un candidat approprié pour les futures frontales radiofréquences intégrées opérant en ondes millimétriques ; Il peut être relié directement à divers circuits MHMIC passifs, ou à des dispositifs actifs par l'intermédiaire de la technologie de liaison par fil, sur un substrat d'alumine ultra mince standard.

## Abstract

In this paper, a broadband 60-GHz millimeter-wave 4x1 microstrip patch antenna array using gap-coupled technique is presented and analyzed. In order to meet the challenging requirement of reduced size related to this kind of technique, and facilitate the integration with other integrated passive or active devices, the proposed antenna array has been designed on thin ceramic substrate ( $\epsilon_r = 9.9$ ,  $h = 127 \mu\text{m}$ ), using an MHMIC (Miniature Hybrid Microwave Integrated Circuits) fabrication process. The proposed structure is based on an improved shape of a gap-coupled patch element with curved radiating edges. For further analysis, the performances of the latter in term of impedance bandwidth, gain and radiation efficiency were investigated and compared with a conventional structure of rectangular gap-coupled patch antenna. The obtained results clearly show that the proposed gap-coupled array structure provides an improved bandwidth (7 %), and an enhanced gain (10.7 dB), while maintaining a reduced size (5.2 mm x 9.5 mm). All these benefits make it an attractive candidate for the future integrated millimeter-wave RF front-end circuits; it can, however, be connected directly to various MHMIC passive circuits, or active devices through using the wire bonding technology, on a standard thin-film alumina substrate.

### 4.1. Introduction

Recently, printed antennas for millimeter-wave applications has become an increasingly important topic given the attractive features such as low profile, light weight, low manufacturing cost, and ease of fabrication and integration with Miniature Hybrid Microwave Integrated Circuits (MHMICs) or Microwave Monolithic Integrated Circuits (MMICs). They have become key components to many diverse commercial, industrial, and military applications including aircraft, spacecraft, satellite, missiles, cars and even handheld mobile telephones [1]. Despite its many advantages, the general design of microstrip patch antenna usually suffers from its intrinsic narrow bandwidth, which is of the order of a few percent (2% - 5%). This characteristic constitutes a real limitation in most of the wireless communication systems that are increasingly designed for supporting a large number of users and providing high data-rate information [2].

In order to overcome this constraint, various techniques were adopted to increase the bandwidth of microstrip patch antennas, such as the slot-loading technique, the multilayered technique, the stacked multilayered technique and by using modified or partial ground [3]-[10].

However, their implementation in practice further complicates the fabrication process, and may pose a difficulty in terms of integration with the existing planar fabrication processes. Many other approaches related to the substrate material choices have also been proposed for enhancing the bandwidth, for instance, by increasing the electrical thickness of the substrate, or by reducing the dielectric constant. Indeed, the increase in substrate thickness significantly degrades the antenna efficiency, especially at millimeter-wave frequencies due to surface wave effects; on the other hand, there are practical limitations in decreasing the dielectric constant [2].

Gap-coupled multiple resonators technique used in microstrip antenna structures, is among the most promising techniques, and the simple solutions that have been proven to significantly increase operational bandwidth and antenna gain. They have been subject to numerous researches over the past years, but, nonetheless, the vast majority of them have brought more interest for low-frequency antenna structures [11]-[20]. Therefore, they do not consider the same issues as in millimeter-wave frequencies, particularly at 60 GHz band. In fact, at this frequency band, the surface wave propagations and the high mutual coupling between adjacent elements have a severe impact on the antenna radiation performance. Moreover, the signals are supplementary attenuated (10-17 dB/km) due to oxygen absorption, in addition to inherent very high path loss due to the operating frequency. This restricts the use of 60 GHz band for long distance communication ( $> 2$  km), and hence makes it entirely suitable for short-range wireless communications (several meters for low power to max 1 km for backhaul solutions) [21]-[23]. The frequency reuse is, therefore, one of the main advantages. Nevertheless, these drawbacks can be limited by designing the antennas having a high efficiency, high gain, an acceptable bandwidth, and readily expandable to the compact array configurations.

In this paper, a compact broadband 4x1 millimeter-wave microstrip patch antenna array using gap-coupled technique is designed, fabricated, and analyzed. The proposed structure is based on gap-coupled microstrip patch elements having curved radiating edges. For performance comparison, an equivalent rectangular gap-coupled patch antenna was also designed as a reference antenna. In order to enable a compact size that usually constitutes a major problem in this kind of technique, an MHMIC fabrication process, and a thin ceramic substrate with high dielectric constant ( $\epsilon_r = 9.9$ ,  $h = 127 \mu\text{m}$ ) have been employed. Finally, to investigate the coupling effect of the gap on the proposed gap-coupled structure, parametric studies were conducted to enable a gap width and input impedance matching optimization.

## 4.2. Antenna designs, fabrication, and measurement

In order to point out the usefulness of the proposed gap-coupled structure in the optimization of the coupling between the driven patch and parasitic element, a conventional rectangular microstrip patch antenna is used as reference antenna for performance comparison. Therefore, a consistent comparison between single rectangular patch (SRP) and single modified patch (SMP) antenna, as well as between their associated gap-coupled configurations is performed. For that purpose, Advanced Design System (ADS) software of Keysight Technologies is used for circuit design, simulation, and performance analysis. As a manufacturing technique, a standard MHMIC fabrication process on thin ceramic substrate has been adopted. The latter provides several interesting features, including miniature circuits, low costs, as well as high level of integration and the use of high precision thin film resistors, fabricated with microstrip line, such as in the case of our fabricated gap-coupled array prototype.

The geometrical configurations of the optimized single modified patch (SMP) and its equivalent single rectangular patch (SRP) antenna are shown in Figure 4.1. Their physical parameters are:  $W=2R=1.071$ ,  $L=0.731$ ,  $W_0=0.708$ ,  $L_1=0.266$ ,  $L_2=0.307$ ,  $d=0.411$ ,  $d_1=0.231$ ,  $d_2=0.180$ ,  $e=e_1=0.061$ ,  $e_2=0.093$ ,  $W_1=W_2=0.127$ ,  $D=0.660$ ,  $f=0.058$ ,  $f_1=0.078$ ,  $E=0.152$ , all units being millimeters.

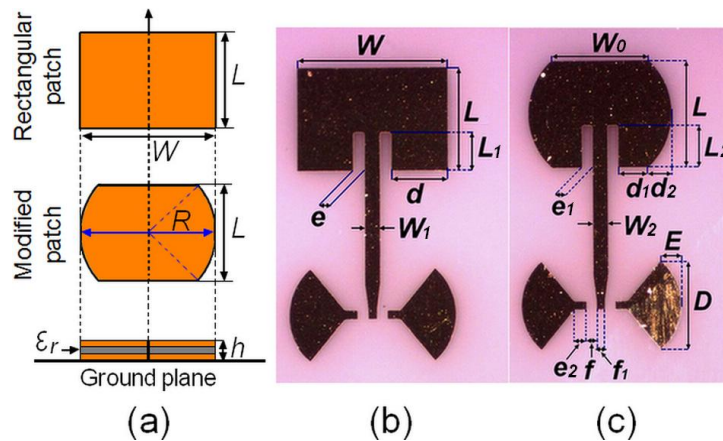


**Figure 4.1** - Single modified patch antenna and its equivalent rectangular patch in (a) Photograph of the fabricated prototypes with the geometrical parameters of the single rectangular patch antenna, and single modified patch antenna in (b), and (c) respectively.

The rectangular gap-coupled patch antenna (RGCP) and the modified gap-coupled patch (MGCP) in Figure 4.2 are also designed to achieve better control of the coupling between driven patch and parasitic element through optimization of the resonating lengths and the gap width between them. Accordingly, a larger operational bandwidth and best input impedance matching will be achieved. Their optimized geometrical parameters are :  $W_x= 1.036$ ,  $L_x= 1.516$ ,  $s_0= 0.111$ ,  $W_y= 1.036$ ,  $L_y= 1.564$ ,  $s= 0.101$ , all units being millimeters.

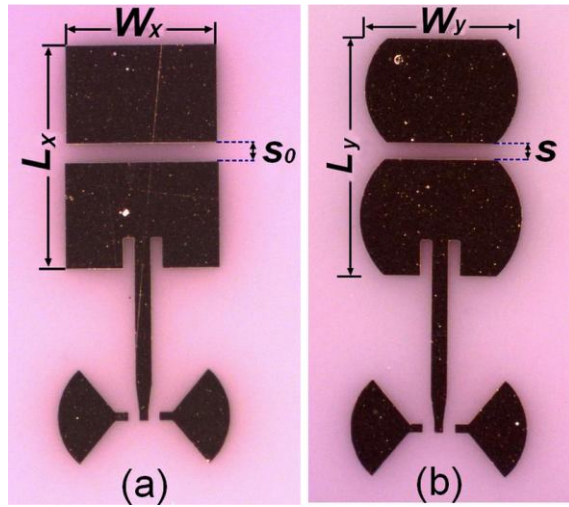


**Figure 4.2** - Photograph of the fabricated prototype with the geometrical parameters of (a) the rectangular gap-coupled microstrip patch antenna and (b) the modified gap-coupled microstrip patch antenna.

The on-wafer return loss measurements of all fabricated microstrip antenna structures were performed using a Cascade Microtech probe station equipped with GSG 150  $\mu\text{m}$  coplanar probes. The latter is connected to a Keysight (Agilent) Technologies millimeter-wave network analyzer (E8362B), with E-band extension modules, operating in 60 – 90 GHz band. Therefore, a coplanar line (CPWG) to microstrip transition is designed and fabricated to enable input return loss measurement with GSG 150  $\mu\text{m}$  coplanar probes. Quarter-wavelength open circuited lines and sectors were also employed as millimeter-wave RF short-circuits while avoiding via holes to ensure measurement repeatability and accuracy. This feeding method is selected because it is the most appropriate, in view of the very compact size of the proposed microstrip structures, and the fragility of the ceramic alumina substrate ( $h=127 \mu\text{m}$ , and a very thin gold layer metallization of 1  $\mu\text{m}$ ). This makes the implementation of a standard 1.85 mm V-connector very challenging, and

may even further complicate the fabrication process. In order to ensure an accurate measurement, the on-wafer Through Reflect Line (TRL) calibration technique was also adopted using the calibration kit on the same ceramic alumina substrate as the devices under test (DUT) [24], [25].

Figure 4.3 compares the simulated and measured return losses of single modified patch (SMP) and its equivalent single rectangular patch (SRP) antenna. As can be seen, the starting frequency is 60 GHz instead of 57 GHz (the starting frequency of unlicensed 60 GHz frequency band). This is due to the capability of our on-wafer measurement facility, as described earlier. Accordingly, the proposed microstrip antenna structures were designed to operate at 61.6 GHz to enable performance comparison. It should be noted that these structures are easily scalable with frequency, such as in the case of the proposed 4 x 1 modified gap-coupled antenna array, which was designed to operate at the unlicensed frequency range around 60 GHz.

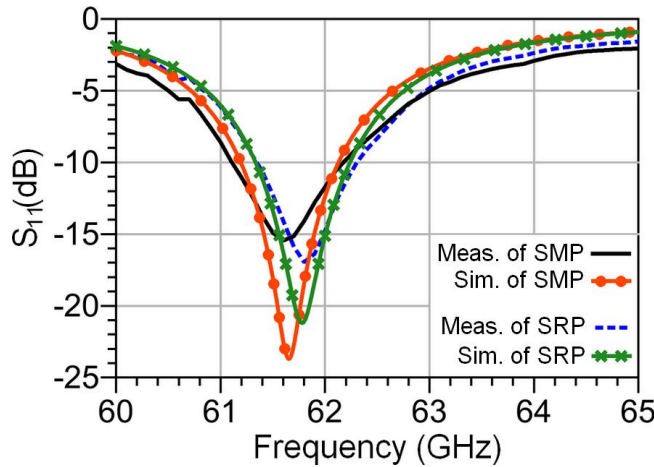


**Figure 4.3** - Measured and simulated return loss of single modified patch (SMP) and single rectangular patch antenna (SRP).

The obtained return loss results in Figure 4.3 show a good agreement with each other over the considered frequency band, from 60 to 65 GHz. The measured impedance bandwidth at -10 dB of the single modified patch (SMP) covers the frequency range of about 1.1 GHz, from 61.1 to 62.2 GHz, which represents 1.78 % at the center frequency of 61.6 GHz. The single rectangular patch (SRP) antenna shows almost the same measured return loss performances with approximately 1 GHz of the measured impedance bandwidth, from 61.4 to 62.4, representing 1.62 % at 61.6 GHz.

Figure 4.4 shows the measured return loss comparing with the simulated one over the investigated frequency band (60 to 65 GHz) for the modified gap-coupled patch (MGCP) and the rectangular gap-coupled patch antenna (RGCP). As can be seen from Figure 4.4, the comparison of measured and simulated insertion loss showed very good agreement. The modified gap-coupled patch (MGCP) resonates efficiently at 61.6 GHz and 63.9 GHz, with a measured impedance bandwidth of 3.7 GHz, from 60.7 to 64.4 GHz, representing, 5.92 % at the center frequency of 62.5 GHz.

The rectangular gap-coupled patch antenna (RGCP), can reach a measured impedance bandwidth of 2.6 GHz (4.16 % at the center frequency of 62.5 GHz), from 60.4 to 63 GHz, which is clearly 1.1 GHz less than the measured bandwidth obtained previously in modified gap-coupled patch (MGCP).

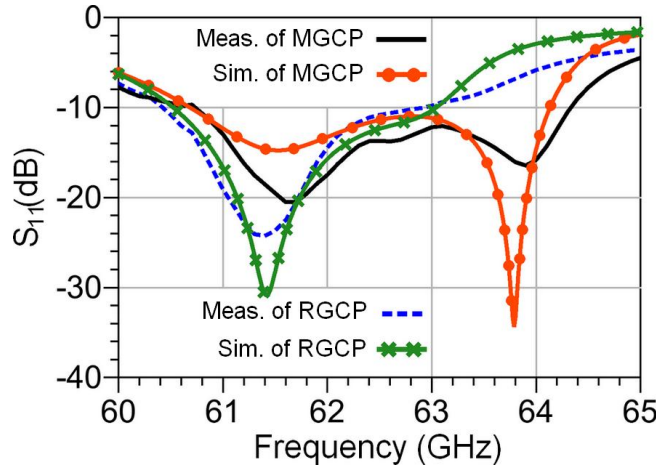


**Figure 4.4** - Measured and simulated return loss of the modified gap-coupled patch (MGCP) and the rectangular gap-coupled patch antenna (RGCP).

However, a slight resonant frequency shift between simulated and measured return loss is observed for both structures, which is mainly due to the tolerances of the dielectric constant and thickness of the ceramic substrate, substrate losses, and fabrication tolerances.

In order to investigate the impact of the proposed single and gap-coupled configurations in Figure 4.1(c) and Figure 4.2(b) on the gain and efficiency, a comparative study at the operating frequency bands (-10 dB return loss bandwidth) is carried out. For that purpose, the single rectangular patch antenna (SRP) and rectangular gap-coupled patch antenna (RGCP) in Figure 4.1(b) and Figure 4.2(a) are considered as reference antennas for performance comparison. In

Figure 4.5, we can see the calculated maximum gain versus frequency of respectively, single modified patch (SMP), single rectangular patch antenna (SRP), modified gap-coupled patch (MGCP) and the rectangular gap-coupled patch antenna (RGCP). As can be seen from the figure, the gain of single modified patch (SMP) and single rectangular patch antenna (SRP) are in close agreement. They increase from 4.25 dB (at 61 GHz) to 4.7 dB (at 62 GHz), and after that they decrease to achieve again 4.25 dB at 62.8 GHz. Similarly, for the modified gap-coupled patch (MGCP) and the rectangular gap-coupled patch antenna (RGCP). They are very close together over 2 GHz, from 60.5 to 62.5 GHz, with peak gains of respectively 6.62 and 6.55 dB. However, the modified gap-coupled patch (MGCP) antenna shows a slightly higher gain compared to the rectangular gap-coupled patch antenna (RGCP). It achieves more than 5.6 dB in the frequency range of 60.5 to 64.5 GHz, whereas the rectangular gap-coupled patch antenna (RGCP) reaches the same level of performance in only 2.7 GHz of frequency range, from 60.5 to 63.2 GHz.

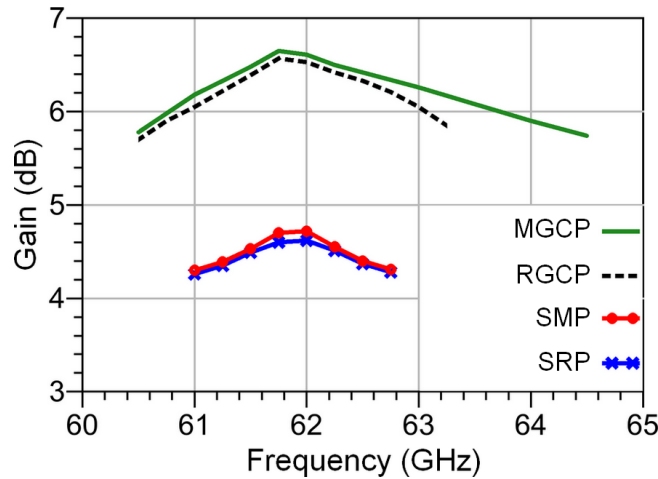


**Figure 4.5** - Calculated gain at -10 dB bandwidth of single modified patch (SMP), single rectangular patch antenna (SRP), modified gap-coupled patch (MGCP) and the rectangular gap-coupled patch antenna (RGCP).

The calculated radiation efficiency for all configurations is shown in Figure 4.6. As can be observed, the radiation efficiency variations of single modified patch (SMP) and single rectangular patch (SRP) antenna are very close to each other's. The maximum value reached for both is 77% at 61.8 GHz, whereas the minimum value achieved is around 73.5% at respectively 61 and 62.75 GHz. For the gap-coupled structures, we can see that the modified gap-coupled patch (MGCP) provides better efficiency, over 70% in the entire operating frequency band, from

60.5 to 64.5 GHz. However, the same performance is obtained for the rectangular gap-coupled patch antenna (RGCP), in only 2.7 GHz of operating frequency band, from 60.5 to 63.2 GHz.

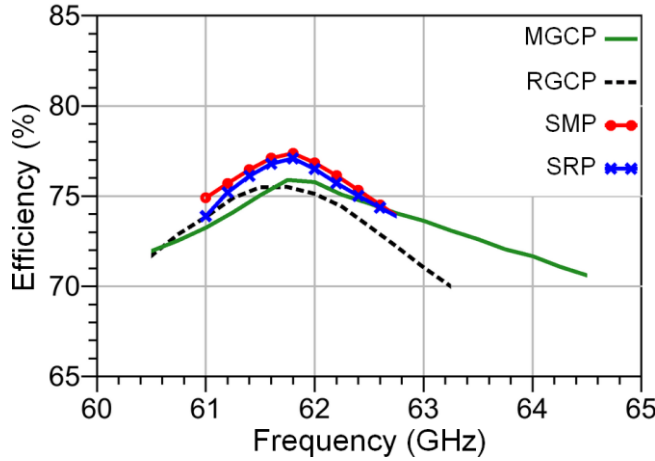


**Figure 4.6** - Calculated efficiency at -10 dB bandwidth of single modified patch (SMP), single rectangular patch antenna (SRP), modified gap-coupled patch (MGCP) and the rectangular gap-coupled patch antenna (RGCP).

### 4.3. Theoretical analysis

The proposed modified gap-coupled patch (MGCP) structure can be analyzed for the two modes, commonly known as even and odd. The theory of such structures has recently been well investigated in the literature [11], [26]. However, this structure can be analyzed by adopting the theory of coupled microstrip lines and coupled microstrip antenna. In this analysis, the total capacitance of the coupled structure is taken as parallel plate capacitance ( $C_p$ ) and two fringing capacitances ( $C_f$ ,  $C_{f'}$ ) for both even and odd mode. It should be noted that the additional fringing capacitance at the adjacent edge of the patches is in fact the result of the additional parasitic element in the proposed gap-coupled microstrip patch structure. Figure 4.7 shows in detail all those capacitances for both modes, even and odd respectively.

The values of these capacitances can be expressed in terms of even and odd mode parameters for propagation, as illustrated in Table 4.1 [11], [26].

From the table, it is noted that the expressions for the capacitances cited earlier including  $C_p$ ,  $C_f$ , and  $C_{f'}$  are given respectively in (1), (2), and (3). We can also distinguish two other

capacitances that characterize the coupling effect between the fed patch and the parasitic patch in odd mode. The first one is the dielectric coupling capacitance  $C_{gd}$ , which represents the capacitance value due to the electric flux in the dielectric area, where its value is calculated in (5). While for the second one, is the air coupling capacitance  $C_{ga}$ , which describes the gap capacitance in air. Its value can be obtained from (6), where  $K(k)$  and  $K(k')$  designate the elliptic function and its complement (7).

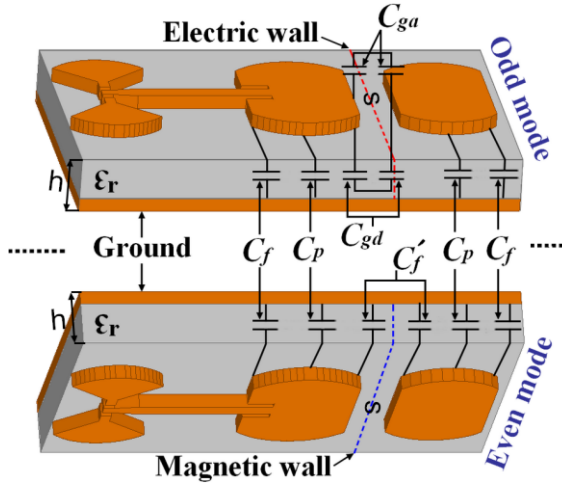


**Figure 4.7** - Even and odd mode capacitances of the proposed gap-coupled microstrip patch antenna structure.

**Tableau 4.1** - Even and Odd mode Capacitances Equations.

Even-mode capacitance	Odd-mode capacitance
$C_{even} = C_p + C_f + C'_f$	$C_{odd} = C_p + C_f + C_{gd} + C_{ga}$
$C_p = \epsilon_r \epsilon_0 (w/h)$ , $\epsilon_0$ : Free-space permittivity	(1)
$C_f = \frac{1}{2} \left[ \frac{\sqrt{\epsilon_{eff}}}{c Z_c - C_p} \right]$ , $c = 3 \times 10^8 \text{ m/s}$ , $Z_c = 50\Omega$	(2)
$C'_f = C_f \left[ 1 + A \left( \frac{h}{s} \right) \tanh \left( \frac{10s}{h} \right) \right]^{-1} \left( \frac{\epsilon_r}{\epsilon_{eff}} \right)^{1/2}$	(3)
$A = \exp(-0.1 \exp(2.33 - 2.53 w/h))$	(4)
$C_{gd} = \left( \frac{\epsilon_0 \epsilon_r}{\pi} \right) \ln \left[ \coth \left( \frac{\pi s}{4h} \right) \right] + 0.65 C_f \left[ \frac{0.02}{(s/h)} \sqrt{\epsilon_r} + 1 - \frac{1}{\epsilon_r^2} \right]$	(5)
$C_{ga} = \frac{1}{2} K(k') \frac{\epsilon_0}{K(k)}$	(6)
$k = \frac{s/h}{(s/h) + 2(w/h)}$ , $k' = \sqrt{1 - k^2}$	(7)

From the table, it is noted that the expressions for the capacitances cited earlier including  $C_p$ ,  $C_f$ , and  $C'_f$  are given respectively in (1), (2), and (3). We can also distinguish two other capacitances that characterize the coupling effect between the fed patch and the parasitic patch in odd mode. The first one is the dielectric coupling capacitance  $C_{gd}$ , which represents the capacitance value due to the electric flux in the dielectric area, where its value is calculated in (5). While for the second one, is the air coupling capacitance  $C_{ga}$ , which describes the gap capacitance in air. Its value can be obtained from (6), where  $K(k)$  and  $K(k')$  designate the elliptic function and its complement (7).

In this analysis, particular attention is paid to the coupling effect between the driven element and a parasitic one. However, according to the Table 4.1, this effect can be assessed quantitatively by estimating the values of the dielectric coupling capacitance  $C_{gd}$  and the air

coupling capacitance  $C_{ga}$ , for different normalized gap distances  $s/h$ . The obtained results for those capacitances with the employed alumina substrate are shown in Figure 4.8.

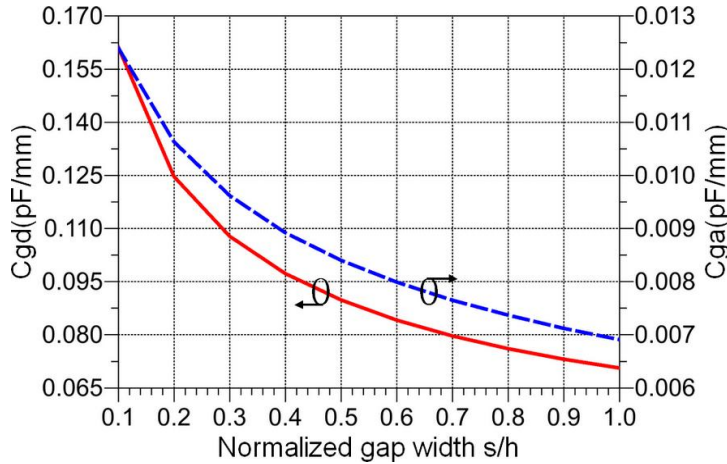


**Figure 4.8** - Coupling capacitances versus normalized gap width for the alumina substrate ( $\epsilon_r = 9.9$  and  $h = 127 \mu\text{m}$ ).

It is noteworthy that the normalized gap width used to obtain the results is increased every step by 0.1 (one-tenth of the substrate height  $h$ ), reaching a maximum value of 1, which corresponds to an overall increase of one time the substrate height  $h$  ( $s=h$ ). In view of these considerations, it can be seen that as the gap width increases, the coupling effect decreases for both capacitances,  $C_{gd}$  and  $C_{ga}$ . The dielectric coupling capacitance  $C_{gd}$  and the air coupling capacitance  $C_{ga}$  have reached their maximum values at respectively 0.162 pF/mm and 0.0125 pF/mm, for  $s/h=0.1$ . While the minimum values reached by these capacitances are respectively 0.072 pF/mm and 0.0069 pF/mm, for  $s/h=1$ . These results clearly demonstrate that the variations of the dielectric coupling capacitance  $C_{gd}$  are approximately ten times higher than the variations of the air coupling capacitance  $C_{ga}$ . This may be explained by the high relative dielectric constant ( $\epsilon_r = 9.9$ ) and low thickness ( $h = 127 \mu\text{m}$ ) of the used alumina substrate.

In order to determine the optimum value of gap distance allowing for a better input impedance matching, the variation of the latter has been expressed as a function of frequency for different normalized gap distances at Figure 4.9. It is observed that the input impedance increases with increasing gap distance at 60 GHz, and decrease after that to attain a minimum value of 20  $\Omega$  at the frequency range of 64 to 65 GHz. Different resonance peaks are also observed at the

frequency around 63.8 GHz, which they increase with decreasing gap distance to reach a maximum value of  $160 \Omega$ . Overall, the optimum value of the gap distance allowing a proper input impedance matching over the considered frequency band corresponds to the normalized value of  $s/h=0.8$  (value selected for our design).

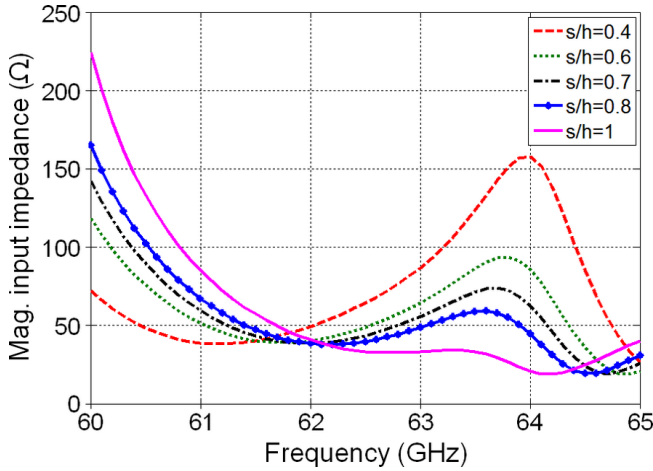


**Figure 4.9** - Variation of the input impedance magnitude with frequency for different normalized gap distances.

#### 4.4. Modified 4x1 gap-coupled microstrip antenna array

The fabricated prototypes of the proposed 4x1 modified gap-coupled antenna array with coplanar line (CPWG) to microstrip transition and V-connector (1.85 mm), are shown in Figure 4.10(a) and 4.10(b), respectively. Its structure consists of four modified gap-coupled patch elements, spaced about  $0.55\lambda_0$  ( $\lambda_0=5$  mm), and a parallel feed network composed of three rounded shape Wilkinson power dividers/combiners [27], along with the  $50 \Omega$  transmission lines. It should be noted that this kind of feed network often employs only T-junction power dividers. Therefore, the architecture of the latter has a decisive effect on the microstrip antenna arrays performance. In this context, the Wilkinson power divider/combiner was selected as the preferred solution to the lossless T-junction problems, which is not matched at all ports and not isolated between output ports. Furthermore, the employed rounded shape Wilkinson power divider/combiner has recently proven that it can achieve the ideal three-port network properties including lossless, reciprocal, and matching at all ports, at millimeter-wave frequencies (up to 86 GHz) [28]. This is the reason why we opted for the rounded shape Wilkinson divider as the best choice in our optimized design of the parallel feed network.

In order to understand the excitation mechanism of the  $4 \times 1$  modified gap-coupled antenna array, simulated surface current distributions on the conductor are illustrated in Figure 4.10(c). In this figure, the electrical field is uniformly distributed, and is coupled from the driven elements to the parasitic elements, which results in excitation of all patches. It should also be mentioned that this coupling is mainly governed by the gap thickness and patch widths between driven and parasitic elements.

Furthermore, to estimate losses and assess the performance of the proposed parallel feed network, its simulated S-parameters including, the return loss, isolation and the transmission coefficient are also presented in Figure 4.11 and 4.12, respectively.

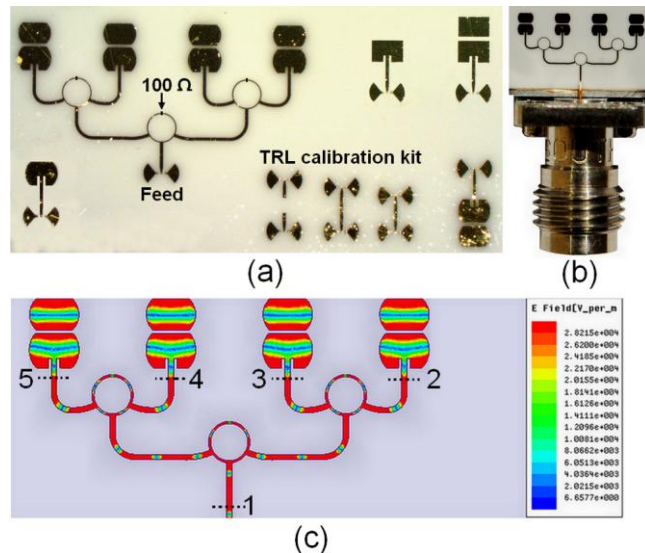


**Figure 4.10** - Photographs of the fabricated  $4 \times 1$  gap-coupled antenna array (a) prototype with coplanar line (CPWG) to microstrip transition (b) prototype with V-connector (1.85) mm and (c) simulated surface current distributions on the conductor.

Figure 4.11 shows the simulated S-parameters of the return loss and the outputs isolation of the employed feed network according to the Figure 4.10(c) above. These results demonstrate a good matching at all ports, with more than -20 dB over the entire unlicensed frequency band, from 57 to 64 GHz. The isolation factor between the adjacent ports (2-3, 3-4, and 4-5) at the output is at least 20 dB, and it has reached 33 dB around 61.8 GHz. This high isolation level is indeed the result of the integrated high-precision resistor implemented with accuracy on  $100 \Omega$ .

per square titanium oxide thin layer [27], using Miniature Hybrid Microwave Integrated Circuit (MHMIC) technology (see Figure 4.10(a)).

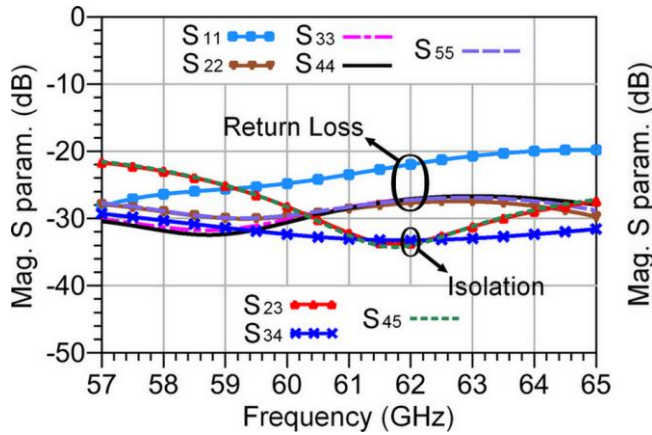


**Figure 4.11** - Simulated RF inputs return loss and isolation of the feed network.

The simulated transmission coefficient results,  $S_{12}$  to  $S_{15}$ , according to the ports at Figure 4.10(c) are illustrated in Figure 4.12. These results show less than 0.5 dB of additional insertion loss over the whole 57 to 65 GHz frequency band. However, a quasi-null amplitude imbalances  $\Delta S_{13,2}$  and  $\Delta S_{14,5}$  between the requested ports are obtained, which does not exceed 0.15 dB. These results prove that the designed feed network is well optimized and has almost negligible additional losses.

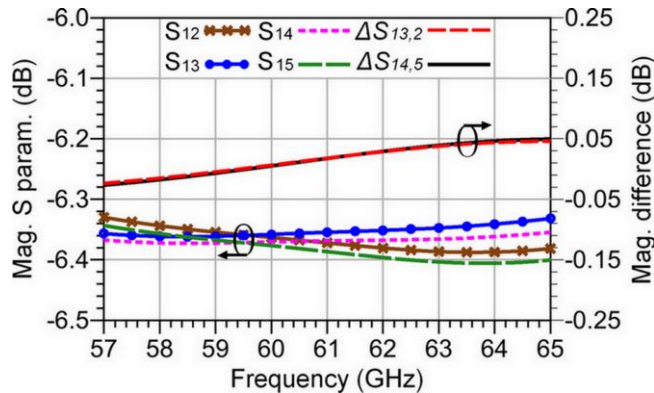


**Figure 4.12** - Simulated transmission S-parameter magnitudes of the feed network.

In order to ensure complete characterization of the proposed gap-coupled antenna array configuration, a 1.85 mm V-connector from Southwest Microwave Company was used to perform measurements of radiation pattern and return losses over the entire unlicensed 60-GHz

frequency band (57 - 65 GHz). For this purpose, An Anritsu 37397C vector network analyzer (40 MHz - 65 GHz), and an automated far-field antenna measurement systems (up to 110 GHz) composed of a rotating standard horn antenna (Quinstar, Model n°qwh-vprr00) have been employed. Photos of both facilities, including the measurement set-ups are shown in Figure 4.13.

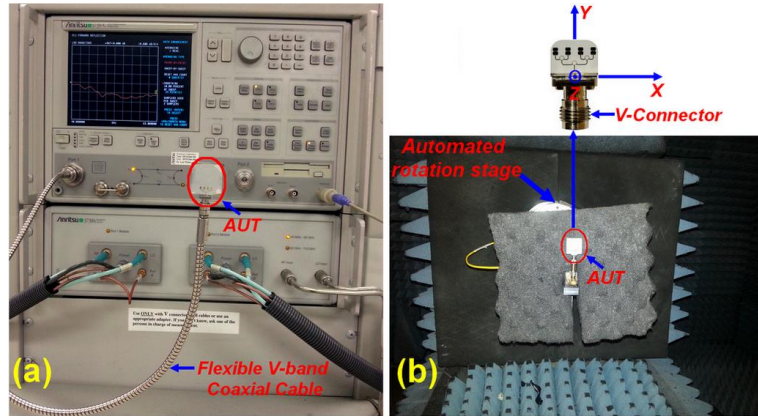


**Figure 4.13** - Antenna under test (AUT) with (a) The Anritsu 37397C vector network analyzer (VNA), and (b) The automated anechoic chamber.

The return loss measurements (1.85 mm V-connector and on-wafer measurements) have been performed after standard TRL calibration of Vector Network Analyzers (VNAs). The obtained results were compared with the simulations in Figure 4.14, over the considered frequency ranges, from 57 to 64 GHz for 1.85 mm V-connector measurement, and from 60 to 64 GHz for on-wafer measurement. These results show that the proposed 4x1 modified gap-coupled antenna array at -10 dB has a measured bandwidth of 4.2 GHz, from 57.8 to 62 GHz, which represents a measured bandwidth of 7 % at the center frequency of 60 GHz. This trend is also confirmed for the on-wafer return loss measurement from 60 to 64 GHz.

Globally, simulated and measured results are in reasonable agreement over the whole 57 to 65 GHz frequency band, except small frequency shift at resonant frequencies, not exceeding 1 GHz. The resonant frequency from simulation at 59.5 and 62.2 GHz, from measurement at 58.4 and 61.2 GHz (1.85 mm V-connector measurement), while from on-wafer measurement, at around 61.8 GHz. This is probably due to the fabrication tolerance, uncertainties in material parameters, and measurement imperfections.

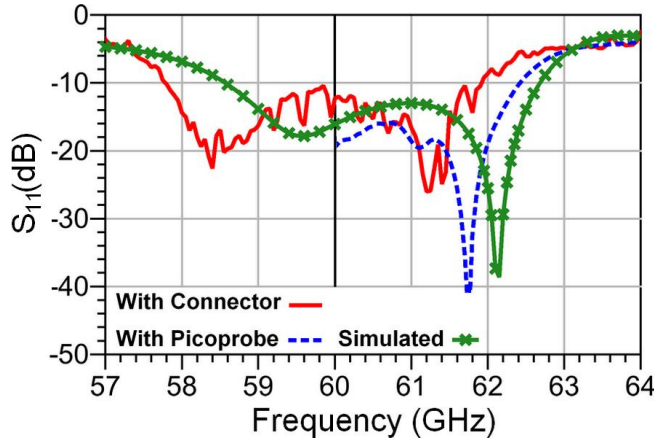


**Figure 4.14** - Measured and simulated return loss of the fabricated 4x1 gap-coupled antenna arrays.

As it can be seen from the Figure 4.14 above, the measured return loss using 1.85 mm V-connector contains some additional amplitude ripples over the considered frequency band (57-65 GHz). This is primarily a result of the unwanted reflections due the mismatch effects between the  $50\ \Omega$  microstrip feed line and the connector, which are in turn related to the soldering quality of the V-connector with the  $50\ \Omega$  microstrip feed line.

The simulated and measured radiation patterns at 60 GHz in both E and H-planes are presented in Figure 4.15 below.

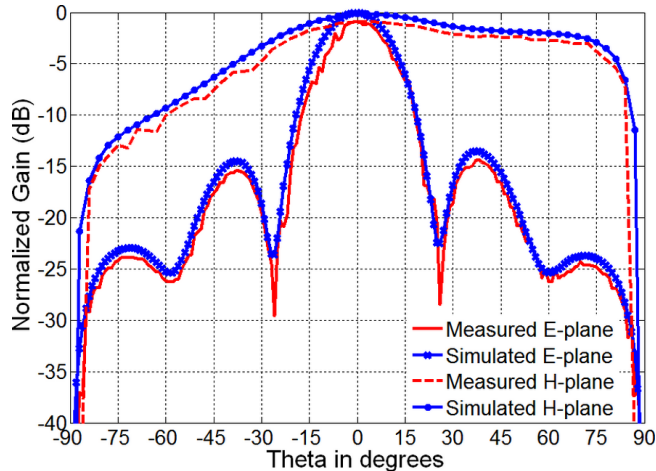


**Figure 4.15** - Radiation patterns of the fabricated 4x1 gap-coupled antenna array in E and H-planes.

The simulated and measured E-plane patterns agree well with each other, while maintaining high symmetry and good broadside radiation pattern. However, a certain asymmetry in the H-plane pattern is observed, which is mainly related to the parasitic elements coupling that makes the radiation pattern slightly inclined towards the front of the array. The half-power beamwidth (HPBW) in the E-plane and H-plane are respectively  $15^\circ$  and  $91^\circ$ , and the first side lobe is about 13.46 dB below the main lobe.

The small variations observed between simulated and measured results for both planes in Figure 4.15, are probably due to the connector losses during radiation pattern measurement and fabrication tolerances, as mentioned earlier.

The results of the measured and simulated peak gain of the proposed 4x1 gap-coupled array configuration over the frequency band of 57.5 to 62.8 GHz (at the operating frequency bands) are shown in Figure 4.16.

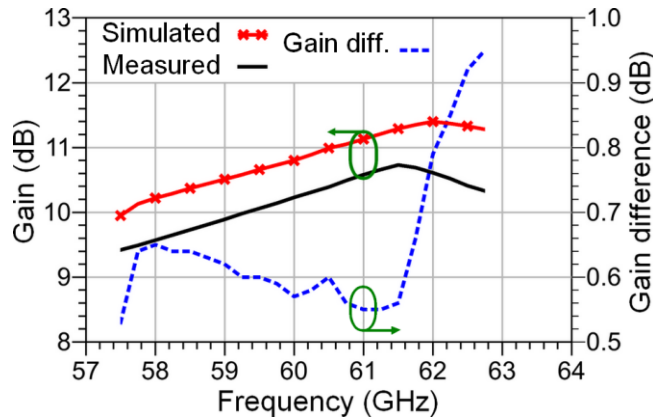


**Figure 4.16** - Simulated and measured gains of the fabricated 4x1 gap-coupled antenna array.

These results show more than 10 dB of measured gain in the operating frequency range (-10 dB return loss bandwidth), from 57.8 to 62 GHz with maximum measured peak of 10.7 dB at 61.5 GHz (simulated 11.4 dB at 62 GHz). However, the difference between simulated and realized gain is more or less 0.95 dB in the considered frequency band. As mentioned previously, the major part of this loss is due to the additional reflections resulted from the 1.85 mm (V) connector, which can reach the insertion loss of 1 dB below 67 GHz [29]. In fact, this problem

can possibly be avoided given the miniature size of the antenna (does not exceed 5.2 mm by 9.5 mm) which enables it to be easily integrated with other components in the package.

## **4.5. Conclusion**

In this study, an improved gap-coupling concept for 60 GHz millimeter-wave microstrip patch antennas has been theoretically investigated, and experimentally validated. For this purpose, a new compact configuration of gap-coupled patch antenna having curved radiating edges has been designed, fabricated, and tested. The principle is to maintain an optimized coupling level from driven to the parasitic element through the modification of the current flowing way around the edges of the patches. This approach may enhance the operational bandwidth to more than four times and increases the gain up to 3 dB as compared to the single modified patch.

Based on the modified gap-coupled patch (MGCP) antenna element that has proved a better bandwidth performance compared to the rectangular gap-coupled patch (RGCP) structure, a 4x1 gap-coupled array antenna has been, also designed and fabricated. The obtained results in terms of bandwidth (7 %), gain (10.7 dB), and compactness (5.2 mm by 9.5 mm), prove evidently a high optimization level of the proposed structure and make it a serious candidate for integration in the future broadband millimeter-wave integrated circuits.

## **Acknowledgment**

The authors would like to acknowledge the Natural Sciences and Engineering Research Council of Canada (NSERC), for the generous research support, and the “Centre de Recherche en Électronique Radiofréquence” (CREER) of Montréal, funded by the “Fonds de recherche du Québec–Natures and technologies” (FRQNT), for the MHMICs fabrication.

## References

- [1] C. A. Balanis, Antenna theory analysis and design, 3rd ed., NY, John Wiley and Sons, 2011.
- [2] G. Kumar and K.P. Ray, Broadband Microstrip Antennas, Boston, MA, USA, Artech House, 2003.
- [3] S. Liu, W. Wu, and D. G. Fang, "Single-feed dual-layer dual-band E-shaped and U-slot patch antenna for wireless communication application," IEEE Antennas Wireless Propag. Lett., vol. 15, pp. 468–471, 2016.
- [4] H. Wong, K. K. So, and X. Gao, "Bandwidth enhancement of a monopolar patch antenna with V-shaped slot for car-to-car and WLAN communications," IEEE Trans. Veh. Technol., vol. 65, no. 3, pp. 1130–1136, Mar. 2016.
- [5] X. Zhang and L. Zhu, "Gain-enhanced patch antennas with loading of shorting pins," IEEE Trans. Antennas Propag., vol. 64, no. 8, pp. 3310–3318, Aug. 2016.
- [6] H. W. Lai, D. Xue, H. Wong, K. K. So, X. Y. Zhang, "Broadband Circularly Polarized Patch Antenna Arrays with Multiple-Layers Structure," IEEE Antennas Wireless Propag. Lett., vol. 16, pp. 525–528, 2017.
- [7] W. C. Yang, H. Wang, W. Q. Che, Y. Huang, and J. Wang, "High gain and low-loss millimeter-wave LTCC antenna array using artificial magnetic conductor structure," IEEE Trans. Antennas Propag., vol. 63, no. 1, pp. 390–395, Jan. 2015.
- [8] H. Sun, Y.-X. Guo, and Z. Wang, "60-GHz circularly polarized U-slot patch antenna array on LTCC," IEEE Trans. Antennas Propag., vol. 61, no. 1, pp. 430–435, Jan. 2013.
- [9] R. Florencio, R. R. Boix, and J. A. Encinar, "Fast and accurate MoM analysis of periodic arrays of multilayered stacked rectangular patches with application to the design of reflectarray antennas," IEEE Trans. Antennas Propag., vol. 63, no. 6, pp. 2558–2571, June 2015.
- [10] R. Azim, M. T. Islam, and N. Misran, "Ground modified double-sided printed compact UWB antenna," Electron. Lett., vol. 47, no. 1, pp. 9–11, 2011.
- [11] C. K. Aanandan, P. Mohanan, and K. G. Nair, "Broad-band gap coupled microstrip antenna," IEEE Transactions on Antennas and Propagation, vol. 38, no. 10, pp. 1581–1586, 1990.
- [12] A. Kandwal and S. K. Khah, "A novel design of gap-coupled sectoral patch antenna," IEEE Antennas Wireless Propag. Lett., vol. 12, pp. 674–677, 2013.

- [13] G. Kumar and K. C. Gupta, "Broadband microstrip antennas using additional resonators gap-coupled to the radiating edges," *IEEE Transactions on Antennas and Propagation*, vol. 32, no. 12, pp. 1375–1379, 1984.
- [14] P. Kumar and G. Singh, "Gap-coupling: a potential method for enhancing the bandwidth of microstrip antennas," *Advanced Computational Techniques in Electromagnetics*, vol. 2012, Article ID acte-00110, 6 pages, 2012.
- [15] C. Wood, "Improved bandwidth of microstrip antennas using parasitic elements," *Inst Electr. Eng Proc. Microw., Opt. Antennas*, vol. 127, no. 4, pp. 231–234, 1980.
- [16] Q. Song and X. X. Zhang, "Study on wideband gap-coupled microstrip antenna arrays antennas," *IEEE Transactions on Antenna and Propagation*, vol. 43, pp. 313–317, 1995.
- [17] C. K. Wu and K. L. Wong, "Broadband microstrip antenna with directly coupled and gap-coupled parasitic patches", *Microwave Opt. Technol. Lett.* 22, 348–349, Sept. 5, 1999.
- [18] K. P. Ray, S. Ghosh, and K. Nirmala, "Compact broadband gap-coupled microstrip antennas," in *Proc. IEEE Antennas Propag. Soc. Int. Symp.*, vol. 9–14, pp. 3719–3722, 2006.
- [19] P. Nayeri, F. Yang, and A. Z. Elsherbini, "Bandwidth improvement of reflectarray antennas using closely spaced elements," *Prog. Electromagn. Res. C*, vol. 18, pp. 19–29, 2011.
- [20] A. A. Deshmukh and K. P. Ray, "Broadband proximity-fed square-ring microstrip antennas," *IEEE Antennas Propag. Mag.*, vol. 56, no. 2, pp. 89–107, Apr. 2013.
- [21] W. Yang, K. Ma, K.S. Yeo, and W.M. Lim, "A Compact High-Performance Patch Antenna Array for 60-GHz Applications," *IEEE Antennas and Wireless Propagation Lett.*, vol. 15, pp. 313–316, 2016.
- [22] C. Hannachi, S. O. Tatu, "A New Compact V-band Six-port Down-Converter Receiver for High Data Rate Wireless Applications," *IEEE Topical Conference on Wireless Sensors and Sensor Networks (WiSNet)*, pp. 26–28, San Diego, CA, USA, 25 – 28 January 2015.
- [23] Adane, A. Gallée, F. Person, C, "Bandwidth improvements of 60 GHz micromachining patch antenna using gap coupled U — Microstrip feeder, " *Proceedings of the Fourth European Conference on Antennas and Propagation*, pp.1-5, Barcelona, Spain, April, 12-16, 2010.
- [24] C. Hannachi, D. Hammou, T. Djerafi, Z. Ouardirhi, and S.O. Tatu, "Complete Characterization of Novel MHMICs for V-band Communication Systems," *Journal of Electrical and Computer Engineering*, Article ID 686708, pp.1-7, October 2013.

- [25] C. Hannachi, E. Moldovan, Z. Ouardirhi, and S.O. Tatu, “V-band Six-port Quadrature Demodulator: Error Vector Magnitude Analysis,” 8th Global Symposium on Millimeter Waves (GSMM 2015), pp.1-3, Montreal, Quebec, Canada, May 25-27, 2015.
- [26] B. K. Kanaujia and A. K. Singh, “Analysis and Design of Gap-Coupled Annular Ring Microstrip Antenna,” International Journal of Antennas and Propagation, Article ID 792123, pp.1-5, 2008.
- [27] D. Hammou, E. Moldovan, and S.O. Tatu, “Novel MHMIC Millimeter Wave Power Divider/Combiner”, 2011 IEEE Canadian Conference on Electrical and Computer Engineering (CCECE 2011), Conference proceedings, pp. 280-283, Niagara Falls, Ontario, May 8-11, 2011.
- [28] E. Moldovan, and S.O. Tatu, “Design and Characterization of Novel W-band Wide-band Couplers and Six-port Circuit,” European Microwave Week, Conference proceedings, pp. 279-282, Paris, France, September 6-11, 2015.
- [29] M. Hrobak, Critical mm-Wave Components for Synthetic Automatic Test Systems, Berlin, Germany, Springer Vieweg, 2015.

## **CHAPITRE 5 :**

# **A V-BAND HIGH DYNAMIC RANGE PLANAR INTEGRATED POWER DETECTOR: DESIGN AND CHARACTERIZATION PROCESS**

**C. Hannachi, B. Zouggari, Razvan I. Cojocaru, T. Djerafi and S.O. Tatu**

Volume 59, Issue 11 Pages 2705–2949, March. 2017

**Résumé :** Dans cet article, un détecteur de puissance opérant dans la bande V (60-65 GHz), ayant une large plage dynamique, a été conçu et fabriqué en employant un procédé MHMIC (Miniature Hybrid Microwave Integrated Circuit). Une diode de type Schottky HSCH-9161 à zéro polarisation opérant en bande millimétrique a été sélectionnée pour la fabrication du détecteur de puissance proposé. Par ailleurs, une transition entre la ligne microruban et guide d'ondes rectangulaire (WR12) possédant une large bande d'opération, ainsi qu'un réseau d'adaptation d'impédance microruban optimisé à l'entrée de la diode, ont été également employés. Les étapes de conception et de caractérisation ont été détaillées afin de fournir une méthodologie efficace pour concevoir des détecteurs de puissance à haute performance tout en tenant compte de la précision, la non-linéarité, ainsi que de la limitation des dispositifs de mesure. Le prototype de détecteur de puissance fabriqué démontre une bonne adaptation d'impédance à l'entrée (une bande passante d'environ 3,8 GHz), une haute stabilité de fonctionnement sur une plage de fréquence de 58,5 à 62 GHz, ainsi qu'une excellente sensibilité (-48 dBm).

Cet article a dû être retiré de la version électronique en raison de restrictions liées au droit d'auteur.

Vous pouvez le consulter à l'adresse suivante :

DOI : 10.1002/mop.30809

## **CHAPITRE 6 :**

### **BROADBAND E-BAND WR12 TO MICROSTRIP LINE TRANSITION USING A RIDGE STRUCTURE ON HIGH-PERMITTIVITY THIN-FILM MATERIAL**

**C. Hannachi, T. Djerafi and S.O. Tatu**

Microwave and Wireless Components Letters, vol. 2017, pp.1-2, May 2017

**Résumé :** Dans cet article, une transition entre la ligne microruban et guide d'ondes rectangulaire (WR12) opérant à la bande E (60-90 GHz) et utilisant un substrat ultra mince en céramique à très haute permittivité est présentée et analysée. La configuration proposée utilise une crête métallique s'étendant progressivement sur une ligne microruban à film mince pour assurer une transformation de champ électrique et une adaptation d'impédance, tout en maintenant un bon contact électrique, sans soudure. Le prototype fabriqué a été testé avec succès en termes de perte d'insertion et de perte de retour. Les résultats obtenus montrent une bande passante de plus de 37% à -10 dB avec une perte d'insertion de 1,5 à 2,7 dB, sur toute la bande de fréquences, de 60 à 90 GHz. La simplicité et l'adéquation de la conception proposée pour des substrats ultra mince et à haute permittivité, ainsi que la très large bande capacité de fonctionnement, permettent d'intégrer la structure proposé facilement aux différents MMIC/MHMIC circuits planaires pour différentes applications en bande de fréquence millimétriques.

## Abstract

A full E-Band (60-90 GHz) WR12 waveguide to microstrip line transition using very thin high-permittivity ceramic substrate is presented and analyzed. The proposed configuration uses a gradually extending metal ridge over a thin-film microstrip line to ensure electric field transformation, and an accurate impedance matching, while maintaining a good electrical contact, without any soldering or gluing. The fabricated prototype has been, successfully tested in terms of an insertion and return loss. The obtained results exhibit a bandwidth of more than 37% at -10 dB with insertion loss of 1.5 to 2.7 dB, over the entire 60 to 90 GHz frequency band. The design simplicity and suitability for high-permittivity thin film substrates, as well as the very broadband operation capability, enable it to be easily integrated with various planar MMICs/MHMICs microstrip circuits for different millimeter-wave applications.

### 6.1. Introduction

The current trend in millimeter-wave technology tends towards increasing component integration to reduce production time and cost for large-scale production. In this context, different integration techniques and fabrication processes, including MHMIC (Miniaturised Hybrid Microwave Integrated Circuits), and MMIC (Monolithic Microwave Integrated Circuits) are used to provide a reliable interface between different components on a single chip [1, 2]. Indeed, all of those components are, typically interconnected via wire bonding or through microstrip lines, leading to the realization of more complex systems, such as RF front-end receivers, or RF transmitter modules. However, the implementation of such systems in practice often requires the use of the waveguides technology, particularly low loss transitions between planar microstrip circuits and traditional rectangular waveguides. The later plays a crucial role in the system's design, and represents a key element for the reliable integration in millimeter-wave frequency bands, and even beyond [3, 4].

In recent years, several millimeter-wave transition configurations between microstrip lines and rectangular waveguides have been, investigated in the literature. For instance, antipodal finline, probe coupling based technique and transition using uniplanar Quasi-Yagi antenna [5]. These transitions exhibit good performances in terms of operating frequency bandwidth and insertion loss, but involve a high degree of mechanical complexity requiring high-precision fabrication processes. Transitions based on ridge waveguide have also, been proposed in [6, 7].

Although these transitions exhibit a full waveguide band performance and low complexity structures, only few of them involved high and thin dielectric constant materials. In fact, millimiter-wave MMICs/MHMICs are often, fabricated on high dielectric constant substrates in order to allow a high level of integration with various standards of millimiter-wave rectangular waveguides.

In this letter, an improved design of a rectangular WR12 waveguide to microstrip line transition using a very thin high-permittivity ceramic substrate ( $\epsilon_r = 9.9$ ,  $h = 127 \mu\text{m}$ ) is presented and analysed. In the proposed design, a ridge structure with a tapered shape is, introduced inside the rectangular waveguide to enable a gradual transformation of impedance and electric field mode, from the rectangular WR12 waveguide to thin-film microstrip line. The obtained results in terms of impedance bandwidth and insertion loss confirm that the proposed transition configuration constitutes a serious alternative to the high-permittivity materials, usually known for their limits to achieve wide bandwidth operation.

## 6.2. Design and Configuration

The conventional design of transition between rectangular waveguide (RWG) and microstrip line (MSL), using a ridge-waveguide structure is illustrated in Figure 6.1. In the proposed transition, the impedance matching and EM field mode transformation between rectangular waveguide and microstrip line are, mainly managed by gradually extending metal ridge in rectangular waveguide, until it matches the impedance and the field distribution of microstrip line. On one hand, this operation allows an accurate impedance matching, from few hundreds of ohms (characteristic impedance of RWG) to fifty ohms (characteristic impedance of MSL). On the other hand, enables a gradual transition, from the fundamental TE10 mode of the rectangular waveguide to the microstrip line quasi-TEM mode [6].

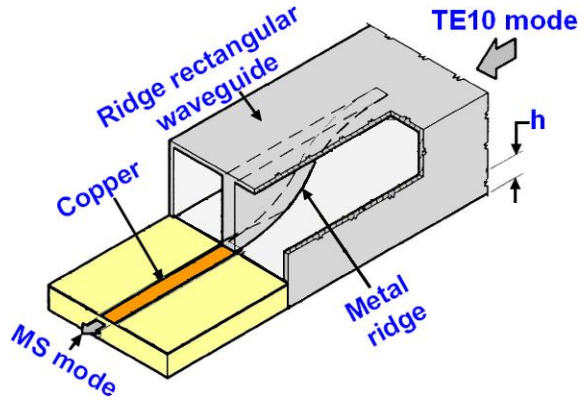


**Figure 6.1** - Microstrip-to-ridge waveguide in-line transition.

The mechanism of the electromagnetic field matching for this arrangement has been detailed in [6], where a transition between rectangular waveguide and microstrip at K-band has been designed, and fabricated using thick 5880 RT/Duroid substrate with single sided copper cladding. Based on similar concept, a new transition configuration employing Duriod based substrates ( $\epsilon_r=2.2$ ) at Q-Band was also proposed in [7]. The latter was suggested as a solution to overcome the difficulties in the mounting reproducibility and DC-block restriction in applications. A transition from microstrip to ridge gap waveguide was also successfully implemented at Ka-band using Arlon CLTE-AT substrate ( $\epsilon_r=3$ ,  $h=0.254$  mm) for integration purposes of MMIC-based RF circuits with gap waveguide-fed antennas [3].

As may be seen, all the previously mentioned works have only referred to lower permittivity materials. As can be observed in Figure 6.2a, the standard transition structure is only suitable for low permittivity substrate with any thickness, and for high permittivity substrate with only thick thickness.

In this approach, the discontinuity created at the substrate-air junction can be modelled by an ideal transformer and pure shunt impedance according to [8, 9]. However, the discontinuity increases with permittivity and inversely proportional to the thickness.

In order to overcome this limitation, simple mechanism should be added to eliminate the imaginary portion created by the junction effect. In this respect, transmission line of length  $l_t=3$  mm and impedance  $Z_{\text{field\_RW}}$  is introduced to rotate the reflection coefficient  $\Gamma$  toward purely resistive loads on the Smith chart. Furthermore, the linear ridge taper of  $l_t=4.07$  mm has the role

of impedance matching for the two purely resistive impedances,  $Z_{RW}$  and  $Z_{WR12}$ , as illustrated in Figure 6.2b below.

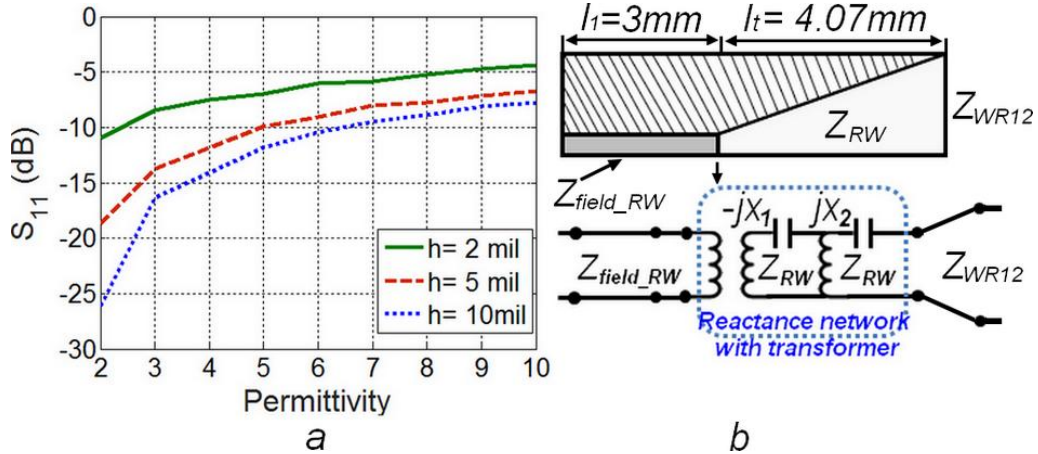


**Figure 6.2** - Parametric study and equivalent circuit,  
 (a) Transition return loss versus permittivity for different thicknesses  
 (b) Equivalent circuit of metal ridge/substrate junction

In our final prototype, shown in Figure 6.3, the ridge waveguide impedance transformer is extended over the microstrip line to enable a good electrical contact without any additional soldering, often resulting in poor repeatability, longer assembly time and increased cost. In order to maintain a good ground contact between the reference plane of the planar thin-film microstrip line and the waveguide body, two parallel arrays of identical metalized via-holes are also, introduced on the substrate, at each extremity of the top part. This allows reducing unwanted substrate waves and, at the same time, to shield the transition from backside radiation leakage.

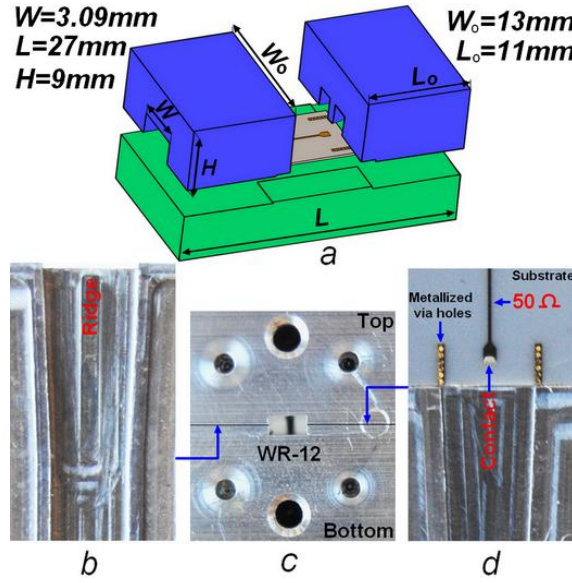


**Figure 6.3** - Proposed rectangular waveguide to microstrip line transition.

- (a) Geometrical structure with the optimized parameters
- (b) Photograph of the fabricated ridge structure (top part)
- (c) Photograph of the compatible WR12 flange
- (d) Photograph of the microstrip structure (bottom part)

### 6.3. Results and Discussion

The simulated and measured S-parameters are obtained using, respectively, the HFSS simulation software by Ansoft Corporation, and Keysight (Agilent) Technologies network analyzer (E8362B) equipped with E-band extension modules, operating in 60 – 90 GHz band.

It should be noted, that the designed transition has been optimized to achieve better performances, especially over 60 to 65 GHz frequency range to be used for V-band high-speed communication transceivers. This is due, to the fact that the proposed structure will be implemented at the input of an integrated MHMIC 60 GHz front-end prototype, currently in development to enable local oscillator (LO) signal feeding [10]. However, in view of the achieved broadband performances, this transition remains useable for others millimeter-wave applications in W-band (70-90 GHz), such as automotive radars and imaging systems.

Figure 6.4 compares the simulated and measured results of insertion and return loss over the entire 60 to 90 GHz frequency band (a typical operating frequency range of a standard WR-12 waveguide). The obtained results are in good agreement and show a return loss of better than -10 dB. The insertion loss variation achieved over the same frequency band is from 1.5 to 2.7 dB.

Nevertheless, frequency response shift of approximately 4% between simulated and measured return loss is observed. Generally, such frequency shift could be the eventual result of manufacturing tolerances, uncertainty in substrate thickness, and permittivity deviation commonly occurring at millimeter-wave bands.

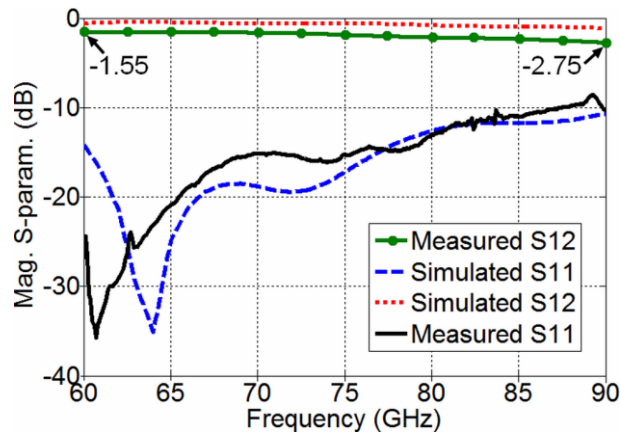


**Figure 6.4** - Measured and simulated insertion loss, and return loss of the fabricated transition prototype.

In order to enable comparison with the previous state of the art, the performance of the proposed transition structure is compared in terms of bandwidth, insertion loss, and complexity level with other transition recently designed on high permittivity substrate. The results are, summarized in Table 6.1.

It is clear from the table that the proposed transition structure achieves better performances compared to other structures. It demonstrates a wider bandwidth (more than 37% at -10 dB), minimal insertion loss variation (losses from 1.5-2.7 dB over the whole 60 to 90 GHz frequency band), and lowest complexity (single-layer fabrication process, good electrical contact without soldering, and easy assembly).

Table 6.1: State of the art of E-band transitions.

Ref.	[1]	[2]	[4]	[5]	<b>This work</b>
Freq. (GHz)	52-65	57-63	69.5-87	60-65	<b>60-90</b>
BW (%) @ -10dB	10.7	5.7	22.7	6.4	<b>37.3</b>
Loss(dB) Min-Max	2.4-5	0.7-3	2.5-9	1.5-4	<b>1.5-2.7</b>
<b>Dielec. const (<math>\epsilon_r</math>)</b>	<b>7.05</b>	<b>9.9</b>	<b>9.5</b>	<b>9.9</b>	<b>9.9</b>
Complexity	High	Med.	High	Med.	<b>Low</b>

## 6.4. Conclusion

A broadband WR12 waveguide to microstrip line transition has been proposed and experimentally demonstrated. The transition structure has been designed to cover the entire E-band (60-90 GHz), using a very thin high-permittivity alumina substrate ( $\epsilon_r = 9.9$ ,  $h = 127 \mu\text{m}$ ). In order to highlight the performance, and the reduced complexity of the fabricated structure, comparison with the previous state-of-the-art has been performed. The obtained results at a similar permittivity show that the proposed approach is the most appropriate to the thin high-dielectric-constant materials, commonly known for their difficulty of achieving wide bandwidth operation. The proposed structure demonstrates better performance in terms of insertion loss, return loss, and lower manufacturing complexity. These very good performances make the designed transition attractive for signal transmission from the rectangular WR12 waveguide components to different planar MHMICs microstrip circuits in different millimeter-wave applications, including our future 60-GHz transceiver front-end, currently under development.

## References

- [1] Lee, J.J., Eun, K. C., Jung, D. Y., and Park, C. S.: ‘A novel GCPW to rectangular waveguide transition for 60 GHz applications’, IEEE Microwave and Wireless Component Letters, 2009, 19, (2), pp. 80–82
- [2] Choi, J. H., Tokuda, K., Ogawa, H., and Kim, Y. H.: ‘Gap-coupled patch-type waveguide-to-microstrip transition on single-layer dielectric substrate at V-band’, Electronics Letters, 2004, 40, (17), pp. 1067–1068
- [3] Zaman, A. U., Vukusic, T., Alexanderson M., and Kildal, P.-S.: ‘Design of a simple transition from microstrip to ridge gap waveguide suited for MMIC and antenna integration’, IEEE Antennas Wireless Propag. Lett., 2013, 12, pp. 1558–1561.
- [4] Zhang, Y., Zhao, D., and Reynaert, P.: ‘A Flip-Chip Packaging Design with Waveguide Output on Single-Layer Alumina Board for E-Band Applications’, IEEE Transactions on Microwave Theory and Techniques, 2016, 64, (4), pp. 1255–1264
- [5] Hammou, D., Nedil, M., Kandil, N., Moldovan, E., and Tatu, S.O.: ‘V-band millimeter-wave microstrip to rectangular waveguide transition’, Microwave and Optical Technology Letters, 2013, 55, (7), pp. 1696–1699
- [6] Ponchak, G. E., and Simons., R. N.: ‘New rectangular waveguide to coplanar waveguide transition’, IEEE MTT-S Int. Microwave Symp. Dig., 1990, 1, pp. 491–492
- [7] Li, J. L., Shao, W., Chen, J. X., and Xue, L. J.: ‘A novel waveguide-to-microstrip transition for millimeter-wave applications’, International Journal of Infrared and Millimeter Waves, 2004, 25, pp. 513–521
- [8] Chang, C. T. M.: ‘Equivalent Circuit for Partially Dielectric-Filled Rectangular-Waveguide Junctions’, IEEE Transactions on Microwave Theory and Techniques, 1973, 21, (6), pp. 403–411
- [9] Angulo, C. M.: ‘Discontinuities in a Rectangular Waveguide Partially Filled with Dielectric’, IEEE Transactions on Microwave Theory and Techniques, 1957, 5, (1), pp. 68–74
- [10] Hannachi, C., Tatu, S.O.: ‘A New Compact V-band Six-port Down-Converter Receiver for High Data Rate Wireless Applications’. Wireless Sensors and Sensor Networks Conference, San Diego, January 2015, pp. 26–28

## **CHAPITRE 7 :**

### **FABRICATION, RÉSULTATS ET DISCUSSIONS**

#### **7.1. Prototypes des frontales radiofréquences fabriquées**

Nous avons en effet, effectué plusieurs tentatives de réalisation de cette frontale radiofréquence. Ces essais comportaient toujours des erreurs liées à la fabrication (coupure au laser, mauvaise insertion du circuit dans la cavité, raccordement de microcircuits par fils sur circuits hybrids, bris du substrat, etc.). Nous étions toujours en contact direct avec les techniciens afin d'identifier ces problèmes, et améliorer la conception du circuit pour qu'elle soit adaptée aux exigences technique ou matériel relatives à la fabrication.

Par exemple, lors de la première tentative de fabrication du prototype (voir Figure 7.1), nous avons rencontré un problème au niveau de l'implantation de l'amplificateur faible bruit (LNA), plus particulièrement, la conception du circuit de polarisation associé à ce dernier. Par conséquent, nous avons eu la difficulté à polariser l'amplificateur faible bruit (LNA), ce qui a engendré un phénomène d'oscillation. Ce problème a été rapidement résolu en implantant deux condensateurs ayant une valeur de 100 pF, plus proche à l'entrée et à la sortie du l'amplificateur faible bruit (LNA). Cependant, cette tentative de réparation a engendré d'autres complications relatives au raccordement par fils (wirebonding), au niveau des entrées de polarisation de l'amplificateur (LNA), ce qui a empêché l'alimentation en DC de ce dernier.

Suite à cette problématique, nous avons pensé de simplifier notre conception de frontale radiofréquence en fabriquant un prototype sans l'introduction du l'amplificateur faible bruit LNA (voir Figure 7.2), et caractériser au même temps ce dernier dans un prototype séparé (prêt à être caractériser présentement). En effet, le prototype fabriqué a été caractérisé avec succès et les résultats expérimentaux seront présentés en détail dans ce chapitre. Ces résultats incluent éventuellement l'évaluation expérimentale de la qualité de la transmission en fonction de différents types de modulation incluant BPSK, QPSK, 8PSK, 16PSK, 16QAM, et 32QAM, ainsi que la validation pratique d'une liaison sans fil à 60 GHz en utilisant le prototype de la frontale radiofréquence fabriquée.

Il faut signaler que le choix d'éliminer l'amplificateur faible bruit (LNA) vient principalement de la complication d'utiliser le prototype fabriqué d'une manière répétable suite aux problèmes liés à la polarisation, tel que mentionné précédemment. Par ailleurs, nous avons jugé également que le gain de 12 dB fourni par l'amplificateur (LNA) peut être facilement compensé, en utilisant une antenne cornet de haut gain (22 à 40 dB) au lieu du réseau d'antenne micro ruban intégré, qui possède un gain d'environ 15 dB. Certes, malgré le fait que nos efforts n'ont pas pu aboutir à l'intégration de l'ensemble des composants constituant la frontale radiofréquence, mais néanmoins ont conduit à la validation du concept en bandes millimétriques, en attendant les futures améliorations au sein de l'équipe supervisée par le professeur Serioja Tatu afin de trouver une solution compatible avec la technique de fabrication MHMIC pour l'intégration des composants actifs nécessitant une polarisation.

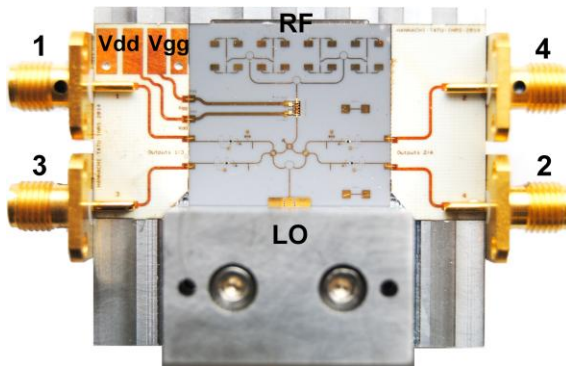


**Figure 7.1** - Premier prototype de la frontale radiofréquence, avec l'amplificateur faible bruit (LNA) et le réseau d'antenne microruban intégré.

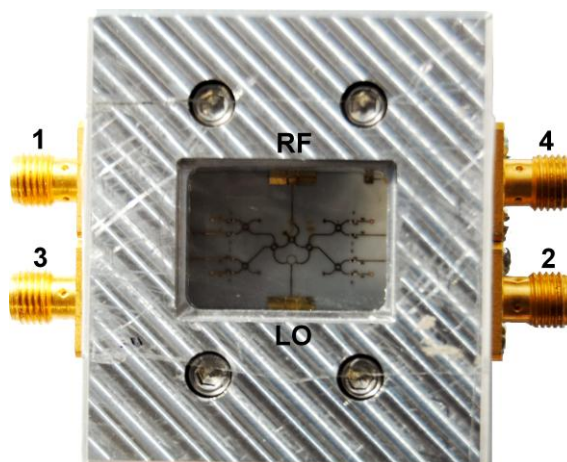


**Figure 7.2** - Deuxième prototype de la frontale radiofréquence, sans amplificateur faible bruit (LNA) et le réseau d'antenne microruban.

## 7.2. Caractérisation d'une frontale radiofréquence à base du RSP en technologie guide d'onde

Dans ce qui suit on propose un banc de caractérisation d'une frontale radiofréquence à base du réflectomètre six-port en technologie guide d'onde pour fin de comparaison des performances avec la frontale radiofréquence intégré proposée. La structure du banc de test comprend une partie émission et une partie réception. La photographie, ainsi que le schéma bloc du banc de test, sont représentés à la figure 7.3 et 7.4 respectivement.

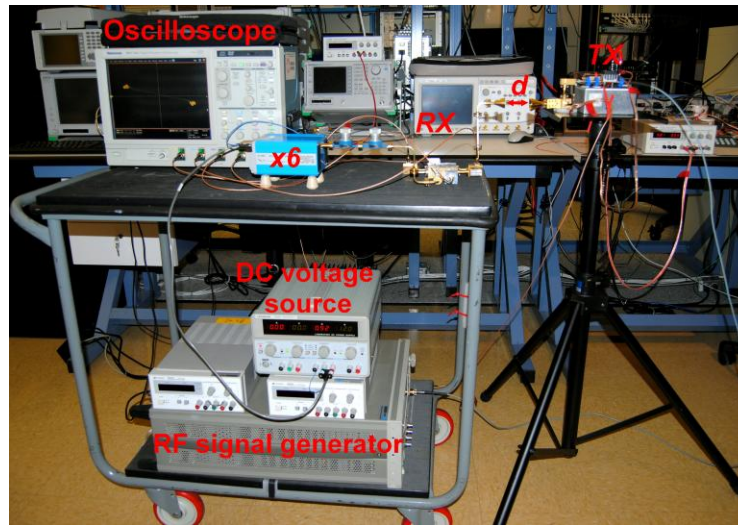


**Figure 7.3** - Banc de test de la frontale radiofréquence à base du RSP (Réflectomètre Six-Port) en technologie guide d'onde.

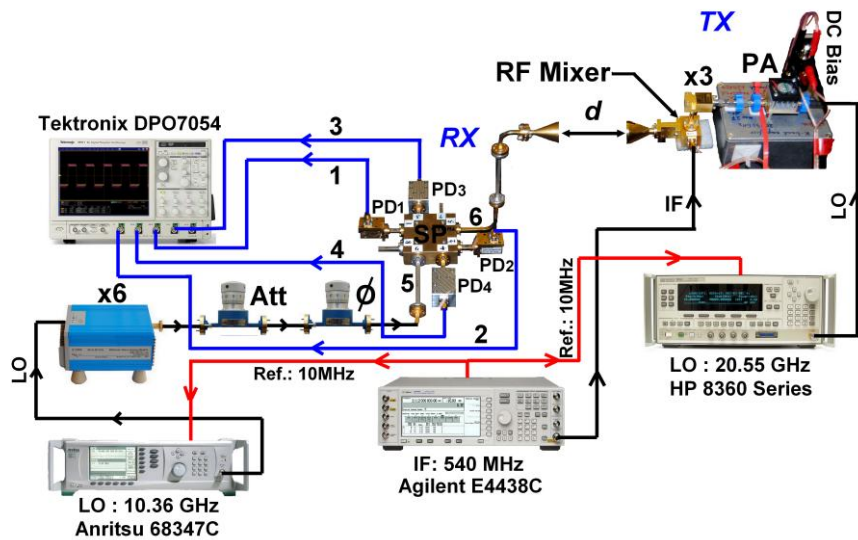


**Figure 7.4** - Schéma bloc du banc de caractérisation.

Les équipements employés dans le banc de test, sont illustrés dans le tableau 7.1 ci-dessous.

**Tableau 7.1**-équipements employés au banc de test

Équipements	Modèles
Sources vectorielles	- Anritsu 68347C - Agilent E4438 - HP 3860 Series
Oscilloscope	Tektronix DPO7054
Frequency multiplier module (x3)	SFP-123KF-S1
Frequency sixtuple module (x6)	S12MS
Waveguide attenuator	DORADO
Phase shifter	DORADO
K-Band power amplifier	-
Millimeter-wave power detectors	HXI, LLC
Millimeter-wave balanced mixer	HXI, LLC
DC power sources	Agilent
E-band conical horn antennas	SAGE Millimeter Inc

La partie émission est composée d'une source vectorielle synchronisée (HP 3860 Series) délivrant le signal RF à la fréquence de 20.55 GHz. Ce dernier est amplifié et multiplié par le multiplicateur de fréquence x3 (SFP-123KF-S1) afin d'atteindre une fréquence dans la bande V, autour de 61.65 GHz. Le signal obtenu est combiné à l'aide d'un mélangeur RF balancé avec le signal de la fréquence intermédiaire (IF) de 540 MHz provenant de la source Agilent E4438. À l'émission, une antenne cornet opérant à la bande de 60 GHz, avec un gain d'environ 22 dB, est employée pour transmettre le signal module à la fréquence  $61.65 \text{ GHz} + 0.54 \text{ GHz} = 62.19 \text{ GHz}$ .

La partie réception est constituée du RSP (réflectomètre six-port), de quatre détecteurs de puissance performants (zero-bias) et d'un atténuateur et déphasage pour contrôler la puissance et la phase du signal (LO) en bande millimétrique. Un multiplicateur de fréquence (x6) est également utilisé afin de générer un signal (LO) à la fréquence de 62.19 GHz, au niveau du port 5 du RSP. Les résultats de démodulation sont affichés directement à l'écran de l'oscilloscope Tektronix DPO7054 [1-3].

Nous avons donc réussi à obtenir les signaux en phase et en quadrature, I et Q, pour différentes modulations et vitesse de bits. Les constellations des signaux démodulés, BPSK,

QPSK, 8PSK ainsi que 16PSK, sont ainsi obtenues et affichées sur l'écran de l'oscilloscope. Les photographies de ces constellations sont représentées à la figure 7.5, ci-dessus [4-5].

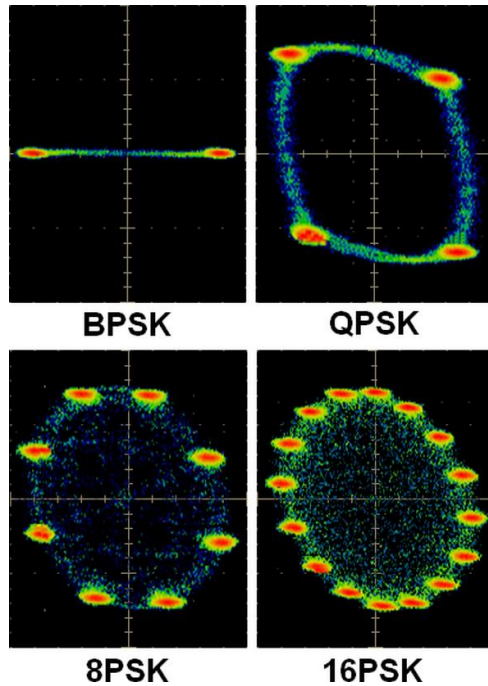


**Figure 7.5** - Résultats de démodulations MPSK (1mV/div).

Comme on peut l'observer sur la figure 7.5, les formes des constellations des signaux démodulées sont légèrement déformées. Cela est dû à plusieurs facteurs, notamment les imperfections de fabrication, inhérentes en bandes millimétriques, générant des distorsions du signal RF en amplitude et en phase, ce qui conduit à la détérioration des performances du récepteur et la qualité de la transmission. On peut distinguer également le problème de fuite OL (Oscillateur Local) à travers le port RF, ce qui peut engendrer une composante DC, un bruit supplémentaire, et une distorsion de second ordre. Cependant, pour les schémas de modulation simples recommandés pour les émetteurs-récepteurs à faible coût, tels que la modulation par déplacement d'amplitude (ASK), par changement de phase binaire (BPSK), ainsi que par changement de phase en quadrature (QPSK), une erreur de phase inférieure à 5% est considérée comme acceptable [6].

## 7.3. Caractérisation de la frontale radiofréquence à base du RSP en technologie MHMIC

### 7.3.1. Simulation système

Dans cette partie, nous allons commencer par évaluer la qualité de la transmission à 60 GHz d'un système émetteur/récepteur pour des débits binaires simulés de l'ordre du Gb/s. Le système émetteur/récepteur sera implémenté en utilisant le logiciel ADS (Advanced Design System), tout en plaçant le RSP dans des conditions réalistes de fonctionnement (gain d'antenne, puissances RF et LO, distance émetteur-récepteur, gain et figure de bruit du LNA, ...etc) tel qu'ilustré dans la figure 7.6.

Telle qu'ilustrée dans la la figure 7.6, le récepteur est composé d'une antenne réceptrice, d'un amplificateur faible bruit (LNA), ainsi que du réflectomètre six-port (RSP) connecté aux quatre détecteurs RF et de deux amplificateurs vidéo. Pour la mise en forme des signaux I/Q, on a utilisé des filtres et des circuits "sample-and-hold (SHC) ". La propagation du signal RF est simulée en utilisant la composante LOS\_Link, fournie par la librairie composant du logiciel ADS, basée sur le modèle de Friis.

On va évaluer donc la qualité de la transmission en fonction de différents types de modulation incluant BPSK, QPSK, 8PSK, 16PSK, 16QAM, 32QAM [6].

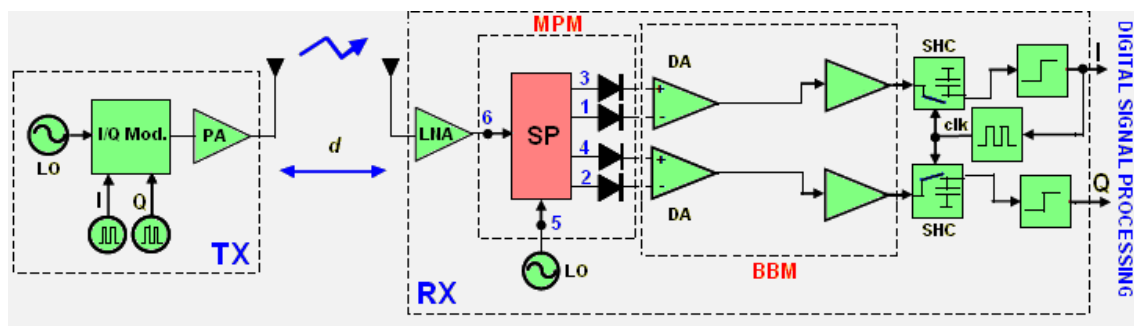
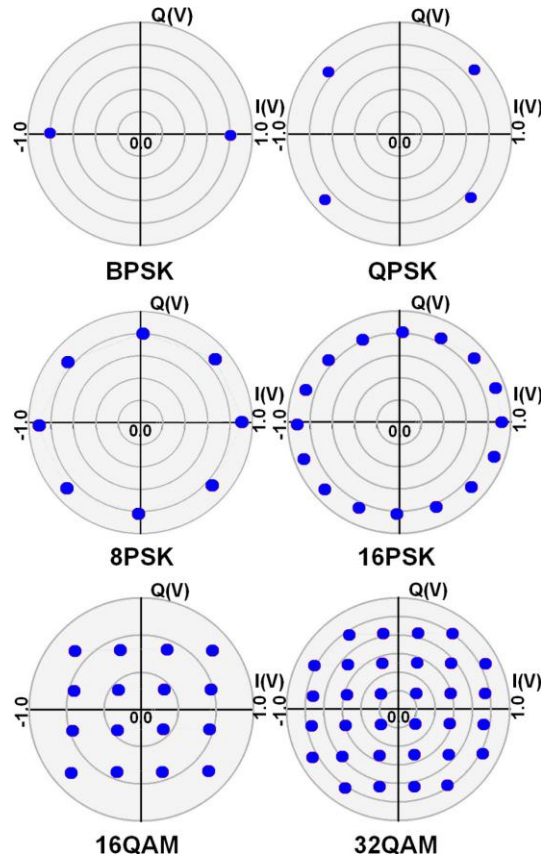


Figure 7.6 - Schéma bloc du circuit de simulation du récepteur à base du réflectomètre six-port.

Nous avons réussi à obtenir les signaux en phase et en quadrature, I et Q, pour différentes modulations. Les constellations des signaux démodulés à une vitesse de 1 Gbits/s sont affichées dans la figure 7.7 ci-dessous.

Comme on peut le constater dans la figure, les symboles des démodulations 8PSK et 16PSK sont répartis uniformément autour du cercle. De même, pour le diagramme de constellation QPSK, on obtient une forme quasi-parfaitement carrée. Par ailleurs, pour les constellations 16QAM, 32QAM, les points sont presque équidistants, ce qui prouve bien la qualité du RSP comme discriminateur d'amplitude et de phase, suivant ainsi la théorie de démodulateur six port [4]. Les erreurs de phase et d'amplitude sont minimales, ne dépassant pas quelques pourcentages pour chaque point de constellation. On rappelle que le modèle du RSP dans la simulation système proposée est obtenu à partir des mesures sur les différents circuits à deux ports. Par conséquent, les erreurs de modèle comprennent des erreurs de fabrication d'un circuit à l'autre et des erreurs de mesure et de configuration de la station VNA (des erreurs de phase liées à la position de la sonde coplanaire de GSG-150 ( $150\mu\text{m}$ )). On peut noter par exemple que pour une erreur de  $10 \mu\text{m}$ , une erreur de phase de  $2^\circ$  peut être engendrée.



**Figure 7.7** - Diagrammes simulés de constellation PSK/QAM des signaux I et Q.

### 7.3.2. Mesure et caractérisation

Dans cette partie, nous allons réaliser un montage similaire à celui dans la Figure 7.4, en remplaçant cette fois la frontale radiofréquence à base de guide d'onde par la frontale radiofréquence intégré en technologie MHMIC. Le nouveau montage de caractérisation est illustré dans la Figure 7.8.

Cette fois, la source vectorielle synchronisée (HP 3860 Series) délivrant le signal RF à la fréquence de 20.57 GHz. Ce dernier est amplifié et multiplié par le multiplicateur de fréquence x3 (SFP-123KF-S1) afin d'assurer une fréquence autour de 61.71 GHz (band V). Le signal obtenu est combiné à l'aide d'un mélangeur RF balancé avec le signal de la fréquence intermédiaire (IF) de 600 MHz (source Agilent E4438). Une antenne cornet opérant à la bande de 60 GHz, avec un gain d'environ 22 dB, est également employée pour transmettre le signal modulé.

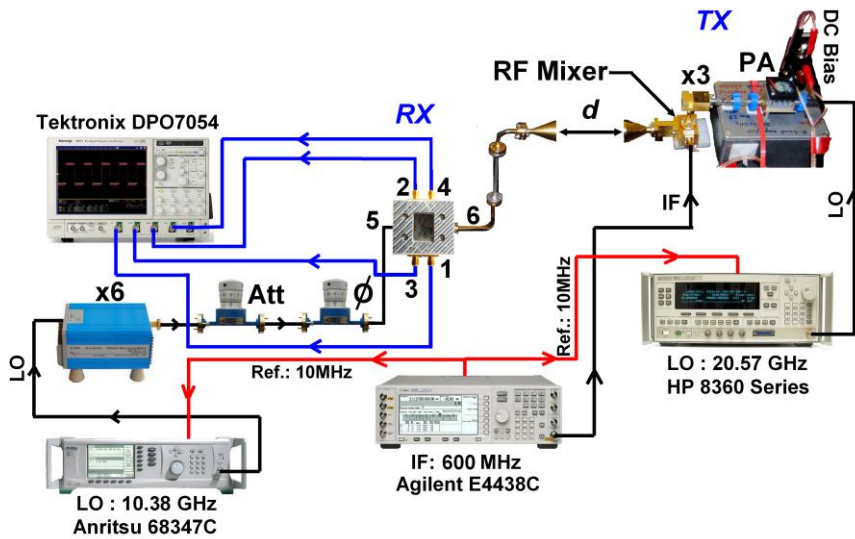


**Figure 7.8 - Schéma bloc du banc de caractérisation d'un récepteur basé sur un six-port intégré en technologie microstrip.**

Lors de la caractérisation expérimentale, nous avons également pu obtenir les signaux en phase et en quadrature, I et Q, pour différentes modulations. Les constellations des signaux démodulés sont affichées dans la figure 7.9 ci-dessous.

Comme on peut le remarquer dans la figure, les symboles des démodulations 8PSK et 16PSK sont répartis uniformément autour du cercle et concordent fort bien avec les résultats des

simulations obtenus précédemment. Pareillement, pour la constellation de la démodulation QPSK, on obtient une forme carrée qui est presque comparable à celle obtenue lors de la simulation. Pour les constellations 16QAM, 32QAM, les points sont uniformément répartis et correspondent également bien aux résultats de simulation ADS.

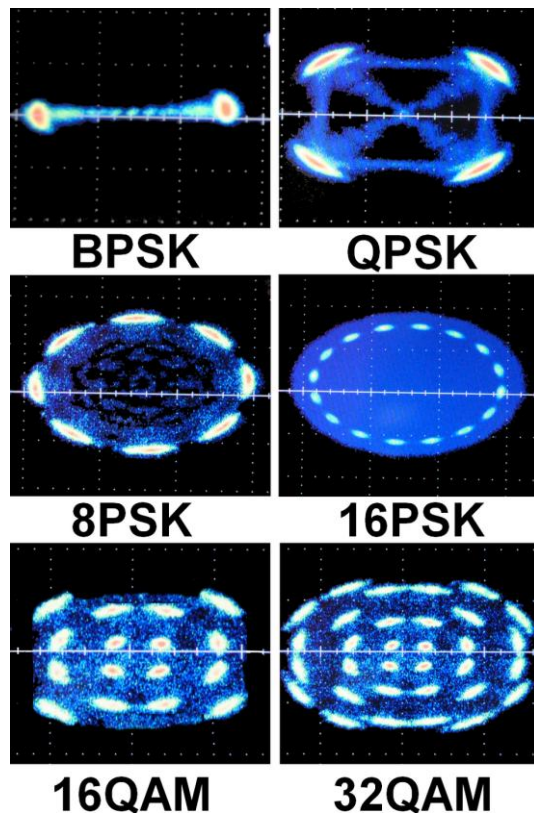


**Figure 7.9** - Diagrammes expérimentaux de constellation PSK/QAM des signaux I et Q (1 mV/div).

### 7.3.3. Validation expérimentale d'une liaison sans fil à 60 GHz

Dans ce qui suit, nous allons examiner la faisabilité d'une liaison sans fil à 60 GHz pour des courtes distances (1-1.75m), en utilisant la frontale radiofréquence fabriqué. Pour se faire, on garde la même configuration dans le montage précédent (voir Figure 7.8), sauf que cette fois on utilise une antenne cornet de haut gain (environ 40 dB), ainsi qu'une lentille spéciale placée à environ 10 cm du récepteur et qui permet d'amplifier le gain de l'antenne réceptrice afin d'aller à des distances plus longues. Toutefois, il faut bien signaler que ces mesures ont été prises pour contourner certaines limitations au niveau des équipements de mesure, notamment les

restrictions relatives à la bande passante et le niveau de puissance permis. Le montage expérimental de cette liaison est illustré dans la Figure 7.10.

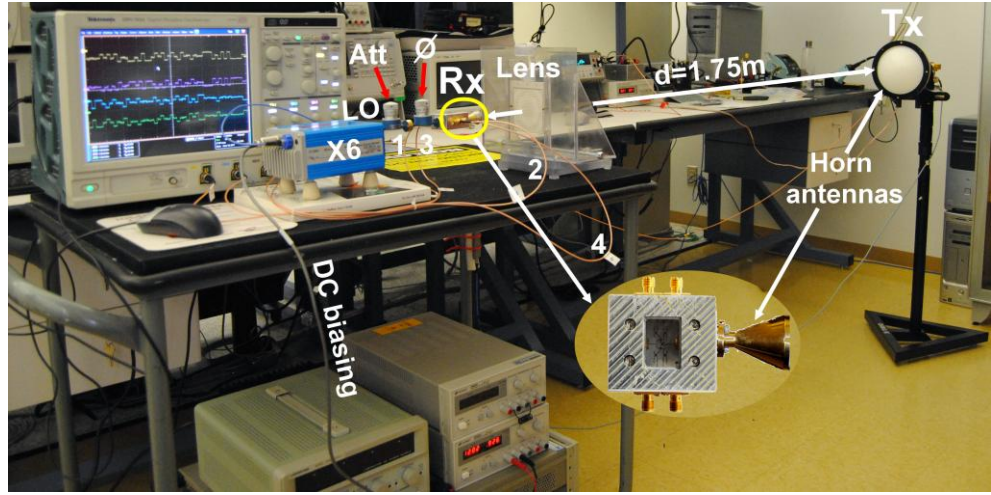


**Figure 7.10** - Photographe du banc de caractérisation du récepteur à base du réflectomètre six-port pour une liaison sans fil de 1.75m.

Nous avons également pu afficher les formes d'ondes des signaux I et Q pour différents types de démodulation incluant BPSK, QPSK, 8PSK, et 16QAM dans le domaine temporel à l'aide de l'oscilloscope, tel que présenté dans les Figures 7.11, 7.12, 7.13, et 7.14.

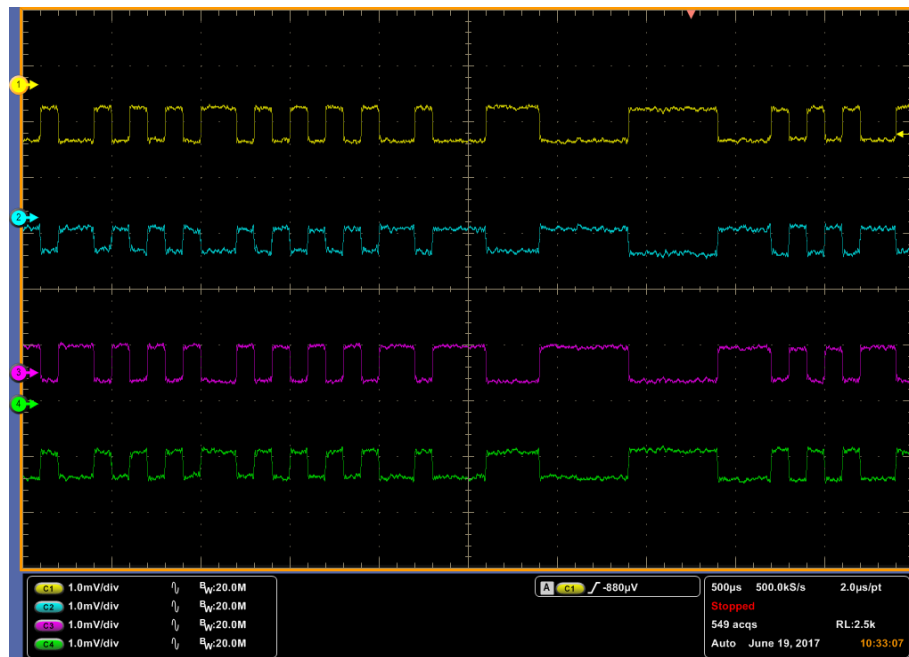


**Figure 7.11** - Formes d'ondes des signaux I et Q pour une modulation BPSK.

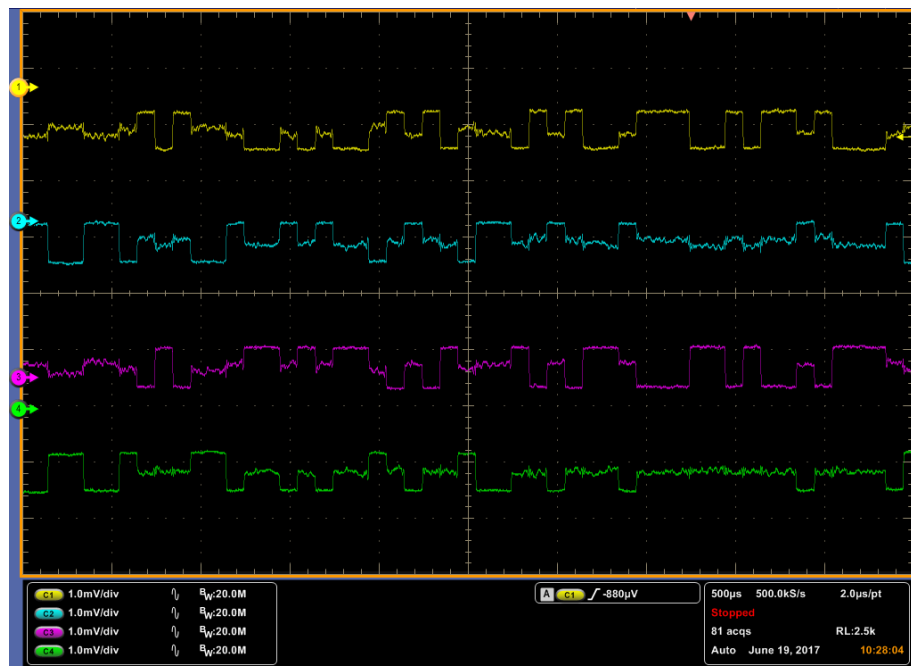


**Figure 7.12** - Formes d'ondes des signaux I et Q pour une modulation QPSK.

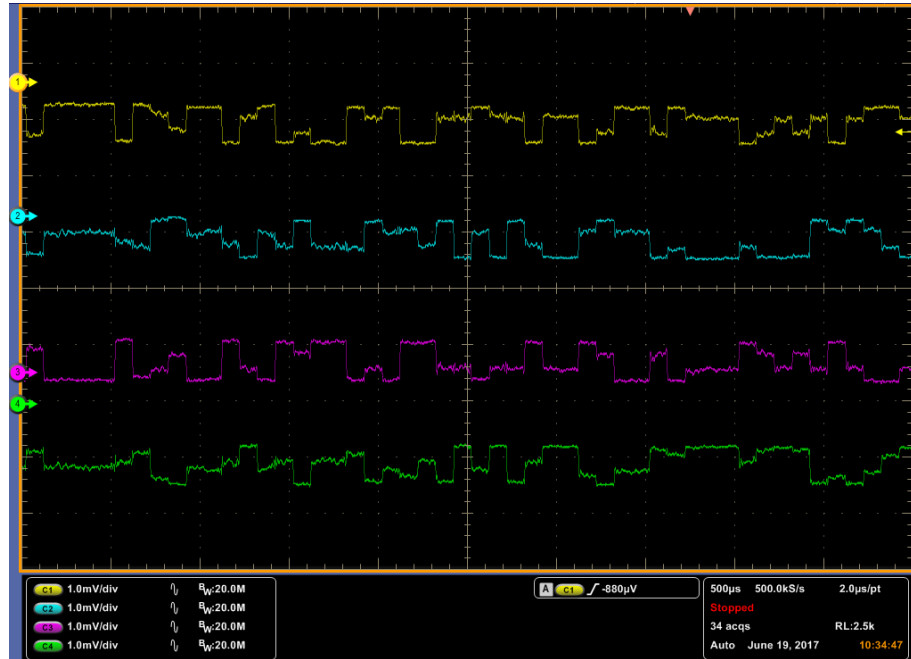


**Figure 7.13** - Formes d'ondes des signaux I et Q pour une modulation 8PSK.

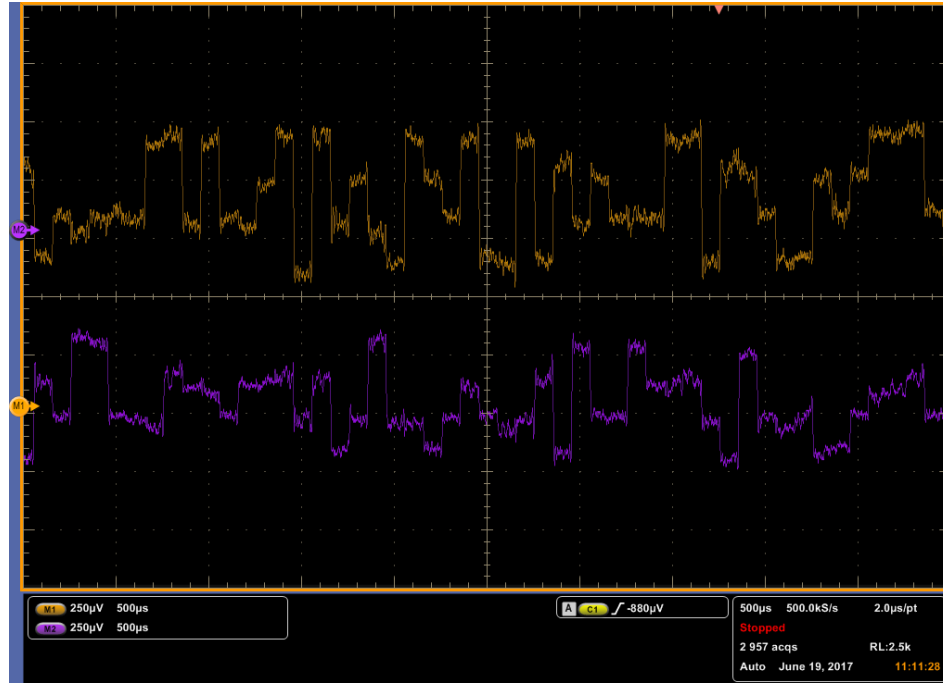


**Figure 7.14** - Formes d'ondes des signaux I et Q pour une modulation 16QAM.

Comme on peut le constater, les résultats dans ces Figures illustrent bien les sauts de phase du signal RF qui correspondent à des multiples de  $90^\circ$ .

#### 7.3.4. Évaluation de la liaison à 60 GHz

Dans cette partie, nous allons présenter les principaux paramètres influant la qualité d'une liaison radio haut débit à 60 GHz. En effet, la propagation des ondes électromagnétiques à la bande 60 GHz est caractérisée par un niveau élevé d'absorption de l'oxygène (une atténuation de 17 dB/Km) et de l'atténuation de la pluie, tout en ajoutant l'atténuation de propagation donnée par la formule conventionnelle de Friis. Ces effets limitent remarquablement la portée des systèmes de communication exploitant cette bande de fréquence, cependant elle permet la réutilisation de fréquence, ce qui la rend très attractive pour nombreuses applications de communication à courte portée. La frontale radiofréquence proposée dans le cadre de cette thèse est également conçue pour fonctionner à des distances courtes de 1 à 10 mètres, avec un rapport signal sur bruit (S/N) d'environ 16 dB [7].

Dans ce qui suit, nous allons évaluer l'atténuation dans l'espace libre, dans un canal de transmission 60 GHz. Considérant ces conditions, La puissance reçue peut être exprimée selon l'équation de Friis [7]:

$$P_r = P_t G_t \frac{A_r}{4\pi d^2} = P_t G_t G_r \frac{\lambda^2}{(4\pi d)^2} \quad (7.1)$$

Dans cette expression  $G_t$  et  $G_r$  correspondent respectivement aux gains des antennes de l'émetteur et du récepteur.  $P_t$ , est la puissance transmise et  $P_r$ , est la puissance reçue. En espace libre, les pertes dues au canal de transmission, sur une distance  $d$ , s'expriment par :

$$\alpha = \frac{\lambda^2}{(4\pi d)^2} \quad (7.2)$$

On peut déterminer aisément à partir de cette équation, l'atténuation du canal de transmission à 60 GHz. Elle est estimée à -48 dB pour une distance de 1.75 mètres et à -88 dB pour une distance de 10 mètres. Si on dispose d'une puissance à l'émission de 10 dB, et un gain d'antenne à l'émission et à la réception de 40 dB et 20 dB respectivement (gain de l'antenne cornet haut gain utilisée à l'émission, ainsi que l'antenne cornet standard à la réception). La puissance reçue incluant les pertes à l'émission et à la réception, ainsi que les pertes de trajet, calculée à partir de la relation de Friis, est estimée à -35 dBm.

### 7.3.5. Sensibilité du récepteur

Parmi les principaux objectifs du bilan de liaison à 60 GHz est de déterminer la puissance de réception minimale nécessaire pour obtenir un rapport signal bruit S/N souhaité et par conséquent une qualité de communication satisfaisante. Cette puissance minimale  $P_{rmin}$  définit cependant la sensibilité du récepteur et s'exprime en fonction du rapport signal à bruit S/N ainsi que la puissance disponible de bruit FkTB à l'entrée du récepteur [8].

$$P_{rmin} = F \cdot k \cdot T \cdot B \cdot \left(\frac{S}{N}\right) \quad (7.3)$$

k : Constante de Boltzmann.

T: Température ambiante 298 K ou température du récepteur.

B : correspond à la bande passante du récepteur et dépend du débit mais aussi du schéma de modulation.

Généralement, la sensibilité est exprimée en fonction du rapport  $E_b/N_0$  qui sert de référence pendant la comparaison du rendement énergétique de plusieurs modulations. En effet, l'introduction des paramètres  $N_0 = N/B$  et  $E_b = S/D_b$ , correspondant respectivement à la densité spectrale de bruit ainsi que à l'énergie moyenne par bit, on peut alors exprimer le rapport signal à bruit S/N par la formule suivante.

$$\frac{S}{N} = \left(\frac{E_b}{N_0}\right) \cdot \left(\frac{D_b}{B}\right) \quad (7.4)$$

La sensibilité du récepteur s'exprime maintenant en fonction du débit binaire  $D_b$  et du rapport signal sur bruit normalisé  $E_b/N_0$ .

$$P_{rmin} = F \cdot k \cdot T \cdot D_b \cdot \left(\frac{E_b}{N_0}\right) \quad (7.5)$$

Cette relation montre clairement que la puissance minimale nécessaire croît avec le débit. À titre d'exemple, un débit de 100 Mb/s contre 10 Mb/s exige un niveau de puissance à la réception supérieure à 10 dB afin de garantir une capacité de communication identique [8-9].

## References

- [1] P. Smulders, P, “Exploiting the 60 GHz band for local wireless multimedia access: prospects and future directions”. IEEE Communications Magazine, vol. 40, no. 1, pp. 140–147, 2002.
- [2] S. O. Tatu, E. Moldovan, G. Brehm, K. Wu et R.G. Bosisio, “Ka-Band Direct Digital Receiver”. IEEE Transactions on Microwave Theory and Techniques, vol. 50 no. 11, pp., 2436 - 2442, 2002.
- [3] S. O. Tatu, E. Moldovan, K. Wu, R.G. Bosisio et T. Denidni, “Ka-Band Analog Front-End for Software-Defined Direct Conversion Receiver”. IEEE Transactions on Microwave Theory and Techniques, vol. 53, no. 9, 2678 - 2776, 2005.
- [4] C. Hannachi, S. O. Tatu, “An Improved-Performance V-band Six-Port Receiver for Future 5G Short-Range Wireless Communications” 2017 IEEE Topical Conference on Wireless Sensors and Sensor Networks (WiSNet), Phoenix, Arizona, January 15 – 18, 2017.
- [5] C. Hannachi, S. O. Tatu, “A New Compact V-band Six-port Down-Converter Receiver for High Data Rate Wireless Applications” Wireless Sensors and Sensor Networks Conference, San Diego, January 2015, pp. 26–28.
- [6] C. Hannachi, E. Moldovan, Z. Ouardirhi, S. O. Tatu, “V-band Six-port Quadrature Demodulator : Error Vector Magnitude Analysis”, 8th Global Symposium on Millimeter-Waves (GSMM2015), Conference Proceedings, Montreal, Canada May 25-27, 2015.
- [7] Pozar, D. M. 2005. Microwave Engineering, 3rd ed. New York: Wiley.
- [8] S. O. Tatu. 2005. “Nouveau récepteur six-port en ondes millimétriques”. Thèse de doctorat, Montréal, École polytechnique, 209p.
- [9] D. Hammou, E. Moldovan et S. O. Tatu. “60 GHz MHMIC Six-Port Model Analysis”, Microwave and Optical Technology Letters, Vol. 52, No. 9, September 2010.

## **Conclusion générale et perspectives**

Les travaux exposés dans ce mémoire porte sur la fabrication et la caractérisation expérimentale, de nouveaux circuits millimétriques en technologie MHMIC, destinés à la future génération des systèmes de télécommunications sans fil.

Nous avons tout d'abord conçu et validé le fonctionnement de circuits de base aux fréquences millimétriques, incluant, le coupleur hybride arrondi H-90°, le coupleur en anneau (rat-race), diviseurs/combineurs de puissance de type Wilkinson, ainsi que le réflectomètre six-port. Les résultats de mesure de tous ces circuits ont été confirmés par les résultats de simulation en utilisant le logiciel ADS Momentum (Advanced Design Systems software of Keysight Technologies). Les circuits conçus sont large bande avec un haut degré d'équilibre en amplitude et en phase, ce qui nous a encouragés d'entamer une nouvelle étape qui consiste à intégrer ces circuits dans une topologie finale de frontale radiofréquence. Dans ce contexte, le réflectomètre six-port proposé constituera le noyau du système millimétrique proposé.

Nous avons par ailleurs mené une étude sur les antennes patchs microrubans, et nous avons développé un nouveau réseau d'antenne de quatre éléments (à base du diviseur/combineur en anneau). Les résultats de simulation et de caractérisation expérimentale de ces antennes, ont démontré de bonnes performances en termes de perte d'insertion, de gain, et d'efficacité.

Un détecteur de puissance à base de diode Schottky a été également conçu et fabriqué dans le but de l'intégrer aux sorties du réflectomètre six-port, dans le cadre de la frontale radiofréquence proposée. Les résultats de mesure ont montré des performances globales très acceptables, en termes d'adaptation, de coefficient de transfert, de sensibilité, et de la largeur de plage dynamique.

Nous avons aussi conçu et fabriqué dans le cadre de ces travaux, une transition opérant en bande millimétrique. Cette transitions permet d'interconnecter, différents supports de transmission tel que : ligne microruban, guide intégré au substrat, et guide d'onde rectangulaire. La transition de ligne microruban vers guide d'onde rectangulaire WR12 est réalisée dont l'objectif est d'alimenter notre prototype de frontale radiofréquence en signal de pompe OL (Oscillateur local). C'est ainsi qu'on assure la synchronisation entre les signaux OL et RF dans la configuration de frontale radiofréquence proposée.

À la fin de ces travaux, nous avons réalisé le prototype final de la frontale radiofréquence à 60 GHz, incluant tous les circuits conçus dans la présente étude. Les résultats de caractérisation confirment bien que le réflectomètre six-port permet la conception d'architecture de frontale radiofréquence, de haute performance, intégrée et à faible coût, pour les futurs récepteurs de communication sans fil à haute débit. Cependant, un point très essentiel reste à améliorer, qui est la répétabilité des processus de fabrication actuels afin de permettre des meilleurs résultats, au niveau de la robustesse des circuits intégrés et les prototypes fabriqués. Plus précisément, la partie qui concerne l'intégration des composants actifs, tels que les amplificateurs à faible bruit (LNAs). Dans ce contexte, nous avons envisagé de caractériser séparément et d'une manière plus approfondie et détaillée l'amplificateur à faible bruit utilisé dans le cadre de la frontale radiofréquence fabriquée. Cela va nous permettre de bien connaître en effet, le comportement de l'amplificateur LNA utilisé et communiquer par la suite, des informations pertinentes aux techniciens afin d'améliorer en continu les méthodes existantes d'assemblage et de fabrication. Une autre alternative peut être également envisagée, qui est le remplacement de l'amplificateur LNA actuel par un autre plus robuste et plus adapté au processus de fabrication adopté. Aujourd'hui, la technologie de communication à ondes millimétriques dans la bande de fréquences de 60 GHz est en plein essor, et les composants actifs dans différentes technologies (AsGa, CMOS,...) opérant dans cette bande ont tendance à se multiplier, donc plus de choix, et plus de composants de qualité seront disponibles au futur.

Enfin, nous avons également pensé à diminuer la vulnérabilité des circuits conçus dans le futur, en optant pour des substrats en céramique plus épais et plus résistants (10 mil et plus), permettant plus de maniabilité pendant le processus de fabrication. Cependant, le niveau élevé de la complexité des circuits conçus sur cette substrat demeure le prix à payer.

## Liste des publications

### Journaux

- [1] **C. Hannachi**, T. Djerafi, and S.O. Tatu, “A Novel Broadband Low-Loss Microstrip Line to Ridged-Waveguide transition Using a Thin Ceramic for Millimeter-wave Applications”, *Microwave and Wireless Components Letters*, vol. 2017, pp.1-2, May 2017. (accepted with major revisions)
- [2] **C. Hannachi**, B. Zouggari, Razvan I. Cojocaru, T. Djerafi, and S.O. Tatu, “A V-band High Dynamic Range Planar Integrated Power Detector: Design and Characterization Process,” *Microwave and Optical Technology Letters*, pp. 1–5, March. 2017. (accepted)
- [3] **C. Hannachi**, and S.O. Tatu, “A Compact V-band Planar Gap-coupled 4x1 Antenna Array: Improved Design and Analysis”. *IEEE Access. Antennas Propag.*, vol. 5, pp.1-8, February 2017. (published)
- [4] **C. Hannachi**, and S.O. Tatu, “Performance Comparison of Miniature Printed MHMICs Patch Antennas with Different Geometrical Shapes for 60-GHz Wireless Applications,” *IET Microwaves Antennas & Propagation*, vol. 11, no. 1, pp. 106-112, Januray 2017. (published)
- [5] **C. Hannachi**, D. Hammou, T. Djerafi, Z. Ouardirhi, S.O. Tatu, “Complete Characterization of Novel MHMICs for V-band Communication Systems”. *Journal of Electrical and Computer Engineering*, vol. 2013, Article ID 686708, pp.1-7, October 2013. (published)

### Conférences

- [1] B. Zouggari, D. Hammou, **C. Hannachi**, and S. O. Tatu, “Precise Direct Millimeter Wave QPSK Modulator for 5 G Wireless Communications” 2018 IEEE Topical Conference on Wireless Sensors and Sensor Networks (WiSNet), Anaheim, CA, January 14 – 17, 2017 (Submitted).
- [2] **C. Hannachi**, S. O. Tatu, “Highly Isolated Broadband Five-port Circuit for V-Band High Data-rate Wireless Communications” The 28th Annual IEEE International Symposium on Personal, Indoor and Mobile Radio Communications (IEEE PIMRC 2017), Montreal, QC, October 8 – 13, 2017 (Submitted).
- [3] **C. Hannachi**, B. Zouggari, and S.O. Tatu, “Low-cost High Data-rate Direct-Conversion Multi-port Receiver for Millimeter-wave Indoor Wireless Applications,” International Union of

Radio Science General Assembly & Scientific Symposium (URSI 2017), pp. 4–9, Montreal, August 2017.

- [4] **C. Hannachi**, S. O. Tatu, “An Improved-Performance V-band Six-Port Receiver for Future 5G Short-Range Wireless Communications” 2017 IEEE Topical Conference on Wireless Sensors and Sensor Networks (WiSNet), Phoenix, Arizona, January 15 – 18, 2017 (Accepted).
- [5] B. Zouggari, **C. Hannachi**, E. Moldovan, and S. O. Tatu, “Millimeter Wave Six-Port QPSK Modulators for High Data-Rate Wireless Communications”, European Conference, 2016 European Microwave Week, Conference Proceedings, London, United Kingdom October 3-7, 2016 (Accepted)
- [6] **C. Hannachi**, B. Zouggari, and S. O. Tatu, “A compact, High Gain and High Efficiency 8×2 Patch Antenna Array for 60 GHz Communication Systems”, 17th International Symposium on Antenna Technology and Applied Electromagnetics (ANTEM 2016), Conference Proceedings, Montreal, Canada, July 10-14, 2016.
- [7] E. Dailleux, J-F. Frigon, **C. Hannachi**, S. O. Tatu, “Millimeter Wave Spatial Multiplexing: Feasibility and Performance of a Short Range 2x2 Link”, European Conference, 2015 European Microwave Week, Conference Proceedings, Paris, France September 6-11, 2015.
- [8] **C. Hannachi**, E. Moldovan, Z. Ouardirhi, S. O. Tatu, “V-band Six-port Quadrature Demodulator : Error Vector Magnitude Analysis”, 8th Global Symposium on Millimeter-Waves (GSMM2015), Conference Proceedings, Montreal, Canada May 25-27, 2015.
- [9] **C. Hannachi**, S. O. Tatu, “A New Compact V-band Six-port Down-Converter Receiver for High Data Rate Wireless Applications” 2015 IEEE Topical Conference on Wireless Sensors and Sensor Networks (WiSNet), San Diego, CA, January 25 – 28, 2015.
- [10] T. Jiang, D. Hammou, **C. Hannachi**, M. Nedil, J-F. Frigon, K. Wu, S. O. Tatu, “Six-port Technology for Millimeter Wave MIMO Systems”, European Conference, 2013 European Microwave Week, Conference Proceedings, Nuremberg, Germany October 6-11, 2013.